

The following pages report the document:

A. Amicarelli, 2025, RANS SPH CFD for Air Quality: a closure on the turbulent Schmidt number constrained to Taylor's theory, grid turbulence and a shear flow; paper preprint; protocol RS2501; pp.1-45.

RANS SPH CFD for Air Quality: a closure on the turbulent Schmidt number constrained to Taylor's theory, grid turbulence and a shear flow

paper preprint (version 4), protocol RS2501; Copyright 2025 (Andrea Amicarelli)
author: Andrea Amicarelli, freelance, Lucca (Italy), andrea.amicarelli@gmail.com

Abstract (max.150 words)

A closure of the mean-concentration Balance Equation on the turbulent Schmidt number SCT is formulated for a Lagrangian deterministic RANS CFD-SPH code on Air Quality (CFD-OUT-sweePDF v.2.0.0, Amicarelli et al.). It is constrained to ‘Taylor’s theory’, ‘Grid turbulence’ and a ‘Shear flow’. Further validations concern a confined flow past a wall-mounted obstacle. Velocity autocorrelation and the systematic SCT dependence on the turbulence Reynolds number are considered. SCT -TGS reproduces the near-source ‘ballistic regime’ and corrects the mean concentration assessed with a state-of-the-art constant SCT up to one order of magnitude. SCT -TGS makes errors negligible under grid turbulence and fills most of the gap between deterministic and stochastic RANS CFD in simulating the mean concentration of a passive pollutant in a shear flow. SCT -TGS ignores the mean-scalar field and might interest any Eulerian/Lagrangian CFD method, RANS-SPDF, the turbulent Prandtl number. The SPH quadrature formulae and reconstruction schemes of the code are specified.

Keywords (5–10)

RANS CFD; turbulent Schmidt number; Air Quality; velocity autocorrelation; SCT -TGS turbulence closure; Sub-Particle Pollutant Source; mean concentration; SPH quadrature formulae; spatial reconstruction schemes; CFD-OUT-sweePDF.

1. INTRODUCTION

In deterministic Reynolds-Averaged Navier-Stokes (RANS) modelling, the turbulent Schmidt number SCT is defined as the ratio between the turbulent viscosity ν_T (m^2/s) and the coefficient of turbulent dispersion K_T (m^2/s) of the transported scalar or pollutant. SCT plays a major role in the diffusion terms of the Balance Equations (BEs) for the concentration mean \bar{C} and variance. SCT is systematically assumed constant (‘ SCT -const approach’) by deterministic RANS CFD codes (i.e. RANS CFD codes based on mean-velocity trajectories). It is equivalent to setting SCT to an intermediate value approximately used all over the domain. Tominaga & Stathopoulos (2007, [1]) reported that RANS CFD studies had been globally used a range of constant SCT values going from 0.2 to 1.3. Some specific SCT reference values are listed hereafter: $SCT=0.72$ (Efthimiou et al., 2017, [2]; Venetsanos et al., 2010, [3]; Violeau, 2009, [4]); $SCT=0.63$ (Hsieh et al., 2007, [5]); $SCT=0.7$ (former state-of-the-art value mentioned by Anand & Pope, 1985, [6]); $SCT=0.70$ (Dong et al., 2017, [7]; Issakhov et al., 2020, [8]); $SCT=0.80$ (experimental value from Fackrell & Robins, 1982, [9]); $SCT=0.90$ (Baik et al., 2007, [10]; Tominaga et al., 2013, [11]; experimental value from Yee & Biltoft, 2004 [12]). Despite being a state-of-the-art common practise, the adoption of any constant SCT value determines a systematic overestimation/underestimation of K_T at small/large flight times since the Pollutant Source PS and neglects the dependence of SCT on the turbulence Reynolds number Ret . The reduced accuracy in reproducing the turbulent flux of the pollutant mass, due to the absence of velocity autocorrelation in SCT -const approach, represents the leading difference between stochastic and deterministic RANS models in simulating the mean concentration. In the following, these model categories are compared by highlighting their differences, no matter about the numerical method used to discretise the BEs.

Deterministic RANS models (e.g. Efthimiou et al., 2017, [2]) assess the concentration ensemble mean and rarely the ensemble variance. A sole set of computational nodes considers both the transporting fluid and the transported scalar. Mean velocity, mean Turbulent Kinetic Energy (TKE) and mean pressure are the main target variables of the simulated air-flow. Either 1st-order or 2nd-order turbulence closures are considered, being the latter rarely adopted for Air Quality. No effect of

velocity autocorrelation is taken into account (Sct -const approach). RANS deterministic models obtain limited accuracy under 2nd-order kinetics via the segregation coefficient. These models are commonly and effectively applied to Air Quality and Water Quality. Turbulence closures of RANS deterministic models on Sct (e.g. Libby & Scragg, 1973, [13]; Deardorff, 1978, [14]) have not reached a large use: some possible explanations are reported in the following. They were computationally expensive and complicated (in case of second-order closures, e.g. Sykes et al., 1984, [15]) and/or depended on the field of the mean scalar. They were mainly conceived or validated on a sole test case. Sct -const approach was not considered inconsistent in the turbulent-diffusion regime as the Sct dependence on Re_T , affecting the Lagrangian integral time scale T_L (s) (Sawford et al., 2008, [16]; Sawford & Pinton, 2013, [17]), was ignored. Sct -const approach covered a much narrower range of permitted values and thus seemed more justified. The use of deterministic RANS CFD was probably deemed to hugely decrease vis-à-vis the growth of RANS-PDF, since the seminal paper of Pope (1985, [18]), and Large Eddy Simulation (LES). The current relative advantages of deterministic RANS CFD and shortcomings of RANS-PDF and LES were partly unknown.

RANS-PDF (Probability Density Function; Pope, 1985, [18]) models represent the most accurate category of stochastic RANS models for turbulent flows with scalar dispersion. Two sets of computational nodes are used via a Particle-in-Cell approach. A complementary solver is needed to assess the mean-pressure gradient in the Stochastic Differential Equation (SDE, e.g. Morkisz & Przybylowicz, 2017, [19]) for velocity. RANS-PDF simulates instantaneous-like quantities and is constrained to an accurate reproduction of both velocity autocorrelation and RANS Reynolds' stress Balance Equation (RS-BE); e.g. the Simplified Langevin Model is coherent with the return-to-isotropy Rotta's RS-BE model. Any ensemble statistic and the pdfs of velocity and concentration are directly estimated. Second-order kinetics are accurately represented. Stochastic RANS models usually apply to combustion processes, but rarely to Air Quality, except for Bahlali et al. (2018, [20]) and Bahlali et al. (2019, [21]), where RANS-PDF is used as LSM (Lagrangian Stochastic Models; e.g. Thomson, 1987, [22]). RANS-LSM is the category of stochastic RANS models most commonly used for Air Quality (e.g. Gariazzo et al., 2004, [23]): they exclusively target concentration and require the velocity statistics in input from any CFD model.

RANS-PDF CFD accuracy is clearly superior to deterministic RANS CFD in assessing the velocity statistics of the transporting fluid and the concentration statistics of the transported scalars in turbulent flows. Nonetheless, the current advantages of deterministic RANS models, still widely used in CFD applications, were partly unexplored. They are computationally efficient and used in a large sequence of application fields. Their simulations involve complex and mobile boundaries also under non-stationary regimes. They use of a sole set of computational nodes and efficiently couple multiple PDEs also dealing with multi-physics.

The aim of the present study is to make deterministic RANS models fill a relevant part of the accuracy gap they experience with respect to stochastic RANS models in representing the mean concentration, at least in the scope of the investigated classes of benchmark. A closure of the RANS BE for \bar{C} (Cm-BE) on the turbulent Schmidt number is presented as ‘ Sct -TGS’; it is constrained to Taylor’s theory (Taylor, 1922, [24]), grid turbulence and a shear flow. It models the effects of velocity autocorrelation, considers the dependence of Sct on Re_T and is written as the default Sct approach of the code CFD-OUT-sweePDF v.2.0.0 (Amicarelli et al.). It is a Lagrangian deterministic RANS CFD-SPH code for turbulent flows with pollutant dispersion. The aforementioned constant value $Sct=0.72$, used in the previous version of the code (Amicarelli, 2024, [25]) for any test case, is here activated only for sparring simulations. The mathematical and numerical models of Sct -TGS are proposed for both Lagrangian and Eulerian deterministic RANS CFD codes. A secondary and separate validation involves the Sub-Particle Pollutant Source (SPPS) scheme. It is a ‘sub-grid’ spatial reconstruction scheme for \bar{C} working in a very limited region just downstream the PS.

The present paper is organised as follows. The code CFD-OUT-sweePDF v.2.0.0 is synthetically described (Sec.2). For sake of brevity, only some detailed descriptions of the features of the previous

code version were reported in Amicarelli (2024, [25]). They concerned: time integration; the stability criteria, the physical bounds and the convergence criteria of the Partial Differential Equations (PDE); the Wall Functions WFs. Other code features validated in Amicarelli (2024, [25]) are described in the current paper, as they are active and further tested with the new simulations. It is the Smoothed Particle Hydrodynamics (SPH) quadrature formulae (Sec.3) and the spatial reconstruction schemes for the mean pressure, the mean TKE and the mean concentration at the PS (Sec.4). It follows the presentation of the main novelties of the current code version: the turbulence closures of the Balance Equation for the mean concentration (Sec.5) and the SPPS scheme (Sec.6). For sake of brevity, the missing descriptions are reported in a following study (Amicarelli, 2025, [26]); they concern the mathematical models of the BEs, the SPH Time-Space Ensemble (SPH-TSE) filter, the stabilisation term in the Momentum Equation and the inlet/outlet sections. The code novelties are validated on three test cases by comparison with the available closed-form solutions (Anand & Pope, 1985, [6], with a minor generalisation of Sec.12.3) and measurements (Fackrell & Robins, 1982, [9]), the numerical results of a stochastic RANS-LSM model (Amicarelli et al., 2011, [27]) and the previous code version (Amicarelli, 2024, [25]). These incremental validations involve grid turbulence with surface PS (Sec.7), an experimental turbulent shear flow with elevated PS (Sec.8) and a confined turbulent flow past a wall-mounted cubic obstacle with Canyon PS (Sec.9). The original contributions of the current study are cited in the abstract and the conclusions (Sec.10). Some general pre-processing procedures are reported in appendix (Sec.11). The closed-forms solutions used for validation purposes under grid turbulence are listed in a second appendix (Sec.12), included a minor generalisation for the mean concentration. Simulations are executed under reduced pressure for barotropic neutrally-buoyant micro-scale air-flows following Amicarelli (2024, [25]) as for the management of Initial Conditions (IC) and stationary conditions. The background pressure is adopted analogously to Isik & He (2021, [28]).

2. THE CODE CFD-OUT-SWEEPDF V.2.0.0

CFD-OUT-sweePDF v.2.0.0 (Amicarelli et al.) is a deterministic Lagrangian RANS CFD-SPH code for turbulent flows with pollutant transport. The following applications have been investigated: Outdoor Air Quality (OAQ), Indoor Air Quality (IAQ) and air-treatment processes for Duct Air Quality (DAQ). They include ordinary stack emissions and accidental releases. The simulated obstacles and buildings are isolated structures or parts of a complex matrix like an Urban Canopy of several tenths of street canyons. The code reproduces any useful spatial resolution under a maximum spatial cover of $2\text{km} \times 2\text{km} \times 0.5\text{km}$. Non-stationary and stationary conditions are directly simulated, whereas many state-of-the-art RANS CFD studies efficiently apply extrapolation algorithms as an alternative to a direct representation of transient regimes (e.g., Galindo et al., 2019, [29]).

The code adopts the Weakly-Compressible (WC) approach to assess the mean pressure, with turbulent transport term in the RANS Continuity Equation (RANS-CE). The code relies on Kato & Launder's improved k- ϵ s model (Kat&Lau-k- ϵ s), being considered one of the most accurate 2-equation 1st-order turbulence closures, and on the mean-concentration Balance Equation (BE). Its closure concerns the turbulent Schmidt number and reproduces the effects of velocity autocorrelation and the dependence of Sc_T on Re_T . The semi-implicit Euler's scheme and forward-backward Euler's schemes rule time integration, merging a spatial linear filter, a stabilisation term in the Momentum Equation and the shell SPH filter to enhance the stability domains. The SPH Time-Space Ensemble (SPH-TSE) filter improves the accuracy of the ensemble statistics under specific conditions. Any RANS-SPH formula is valid at any Re ; alternative Implicit LES (ILES-SPH) and Navier-Stokes (NS-SPH) formulations are also available. The code is written in Fortran 95 and has not been distributed. Further details follow hereafter.

The application of the SPH filters $\langle \rangle$ and the semi-implicit Euler's scheme to the RANS Momentum Equation (RANS-ME) and the Trajectory Equation (TE), traced by the mean motion of the computational particle ' o ', provides the following Partial-Differential-Equation (PDE) scheme:

$$\bar{\underline{u}}_{0,k+1} = \bar{\underline{u}}_{0,k} + \left\{ \begin{array}{l} \bar{g} - \frac{1}{\bar{\rho}_0} \langle \nabla \bar{p} \rangle_{C1,0} - \frac{2}{3} \langle \nabla \bar{q} \rangle_{C1,0} + \left\langle \nabla \cdot \left[(\nu_T + \bar{\nu}) (\nabla \otimes \bar{\underline{u}})^T \right] \right\rangle_{C0,0} \\ - 2(1 - c_{TB}) \max \left\{ \left(\frac{\bar{p}_0}{\bar{\rho}_0} + \frac{2}{3} \bar{q}_0 \right); 0 \right\} \langle \nabla 1 \rangle_{C-1,0} \end{array} \right\}_k \Delta t_k \\ \underline{x}_{0,k+1} = \underline{x}_{0,k} + \bar{\underline{u}}_{0,k+1} \Delta t_k \quad (2.1)$$

where $\bar{\underline{u}}$ (m/s) is the mean velocity vector, \bar{g} (m/s²) is the gravitational acceleration, \bar{p} (Pa) is the mean pressure, $\bar{\rho}$ (kg/m³) is the mean density, \bar{q} (m²/s²) is the mean Turbulent Kinetic Energy (TKE), ν_T (m²/s) is the turbulent viscosity, $\bar{\nu}$ (m²/s) is the mean kinematic viscosity, t (s) is time, Δt (s) is the time step duration, the subscript ‘ k ’ indicates the time step and \underline{x} (m) is the particle position. The subscripts ‘ $C-1$ ’, ‘ $C0$ ’ and ‘ $C1$ ’ denote C-1-, C₀- and C₁-consistent SPH filters. The last term within curl brackets in (2.1) is the ‘ME stabilisation term’ and also inhibits the so-called SPH tensile instability (Vignjevic & Campbell, 2009, [30]) thanks to its null limiter. This term plays an analogous role to SPH Particle Shifting Techniques (e.g. Crespo et al., 2008, [31]; Aristodemo et al., 2015, [32]; Cui et al., 2020, [33]) since both reduce the deformations of the control volumes (Fang et al., 2017, [34]). Only close to some simplified outlet sections ‘_{TB}’, the truncated portion of the SPH kernel support is not reconstructed: here the stability constant c_{TB} is non-null, the limiter above is deactivated and C₀ consistency is set.

Analogously to the WC approach for ILES-SPH (e.g., Cui et al., 2019, [35]; Tagliafierro et al., 2022, [36]), the SPH RANS-CE is used to assess the mean pressure via a barotropic Equation of State, which is averaged after Reynolds. The WC approach is alternative to keeping density constant and applying any algorithm for pressure-velocity coupling (e.g., Issakhov & Baitureyeva, 2019, [37]). The SPH filters and the forward-backward Euler’s scheme with linear filter applies to RANS-CE as:

$$\begin{aligned} \bar{\rho}_{0,k+1,PRE} &= \bar{\rho}_{0,k} + \left[-\bar{\rho}_{0,k} \langle \nabla \cdot \bar{\underline{u}} \rangle_{C1,0,k+1} + \langle \nabla \cdot (\nu_{T,k+1} \nabla \bar{\rho}_k) \rangle_{C0,0} \right] \Delta t_k, \\ \bar{\rho}_{0,k+1} &= (1 - \theta_{0,k+1}) \bar{\rho}_{0,k+1,PRE} + \theta_{0,k+1} \langle \bar{\rho}_{k+1,PRE} \rangle_{C0,0}, \\ \theta_{k+1} &= \frac{\left(c_1 \frac{c_{ref}}{h} - 2 \frac{c_2 \nu_{T,k+1}}{h^2} \right) \Delta t_k}{(1 - W_{k+1} \omega_{k+1}) \left(1 + c_1 \frac{c_{ref}}{h} \Delta t_k \right) - 2 \frac{c_2 \nu_{T,k+1}}{h^2} \Delta t_k} \end{aligned} \quad (2.2)$$

where θ is the RANS-SPH smoothing coefficient, c_{ref} (m/s) is the sound speed at the reference state, W (m⁻³) is the SPH kernel function, ω (m³) is the particle volume, h (m) is the kernel support size, the subscript ‘_{PRE}’ indicates the predictor stage, c_1 and c_2 are derived from stability analyses.

The application of the SPH filters and a forward-backward Euler’s scheme, stabilised by the shell SPH filter, to the RANS Balance Equation for the mean Turbulent Kinetic Energy (TKE-BE) provides the following PDE scheme:

$$\bar{q}_{0,k+1} = \frac{\bar{q}_{0,k} + \left(\langle P_q \rangle_{SH^*,C1,0,k} + \langle D_q \rangle_{SH^*,C0,0,k} \right) \Delta t_k}{\left(1 + \frac{\bar{\varepsilon}_{0,k}}{q_{0,k}} \Delta t \right)}, \quad (2.3)$$

$$\langle D_q \rangle_{SH^*,C0,0} = \left\langle \nabla \cdot \left[(\nu_T + \bar{\nu}) (\nabla \bar{q}) \right] \right\rangle_{SH^*,C0,0}, \quad \langle P_q \rangle_{SH^*,C1,0} = 4\nu_{T,0,SHq} \sqrt{(-\langle S_m \rangle_{C1,0}) \langle R_m \rangle_{C1,0}}$$

$\langle P_q \rangle$ (m²/s³), $\langle D_q \rangle$ (m²/s³) and $\bar{\varepsilon}$ (m²/s³) are the production, diffusion and dissipation rates of the mean TKE. S_m (s⁻²) and R_m (s⁻²) are the quadratic invariants of the mean strain-rate tensor and of the

mean rotation tensor. The subscript ‘ $_{SH^*}$ ’ indicates that, in the formulation of the turbulent viscosity, \bar{q} is replaced by its shell SPH filter, i.e. the SPH filter net of the contribution of the computational node. Instead, where the subscript ‘ $_{SHq}$ ’ is used, \bar{q} is always replaced by its shell SPH approximation. The application of the SPH filters and the forward-backward Euler’s scheme (version of Leroy et al., 2014, [38]) to the BE of the mean-TKE dissipation rate (eps-BE) provides the following PDE scheme:

$$\bar{\varepsilon}_{0,k+1} = \frac{\bar{\varepsilon}_{0,k} + (\langle P_\varepsilon \rangle_{C1,0,k} + \langle D_\varepsilon \rangle_{C0,0,k}) \Delta t_k}{\left(1 + C_{\varepsilon_2} \frac{\bar{\varepsilon}_{0,k}}{q_{0,k}} \Delta t \right)}, \quad (2.4)$$

$$\langle D_\varepsilon \rangle_{C0,0} = \left\langle \nabla \cdot \left[\left(\frac{\nu_T}{\sigma_\varepsilon} + \bar{\nu} \right) (\nabla \bar{\varepsilon}) \right] \right\rangle_{C0,0}, \quad \langle P_\varepsilon \rangle_{C1,0} = 4C_\mu C_{\varepsilon_1} \bar{q}_0 \sqrt{(-\langle S_m \rangle_{C1,0}) \langle R_m \rangle_{C1,0}}$$

where $\langle P_\varepsilon \rangle$ (m^2/s^4) and $\langle D_\varepsilon \rangle$ (m^2/s^4) are the SPH eps-BE production and dissipation terms. The constants $(C_\mu, \sigma_\varepsilon, C_{\varepsilon_1}, C_{\varepsilon_2})$ are defined by Launder & Spalding (1974, [39]). The constants of any RANS turbulence closure are derived under equilibrium turbulence, represent relevant approximations under non-equilibrium conditions typical of complex flows and thus they might be reformulated in future studies, following the investigations in Fang et al. (2017, [40]). No explicit filtering technique for WC high-frequency acoustic waves (e.g. Chen et al., 2022, [41]) is adopted. These numerical waves are damped by the combined effect of the SPH-TSE filter, the SPH RANS-CE time scheme, the stabilisation effect of θ and the acoustic convergence criterion

$$\Delta t_{AW} \equiv 0.10 F_{\Delta t} \frac{2h}{c_{ref} + |\underline{u}|_{max}}, \text{ where } F_{\Delta t} \text{ is the optimisation factor (Amicarelli, 2024, [25])}.$$

The application of the SPH filters and a variant of the forward-backward Euler’s scheme to the BE for the mean concentration \bar{C} (kg/m^3) of a passive pollutant provides the following scheme:

$$\bar{C}_{0,k+1} = \bar{C}_{0,k} + \left\langle \nabla \cdot \left[\left(D_M + \frac{\nu_{T,k+1}}{Sc_{T,k+1}} \right) \nabla \bar{C}_k \right] \right\rangle_{C0,0} \Delta t_k \quad (2.5)$$

where D_M (m^2/s) is the coefficient of molecular diffusion and Sc_T is discussed in Sec.5.

The code relies on a tenth of original stability conditions and physical-bound conditions for the PDE schemes presented above, including stabilisation terms and Δt -dependent conditions. They are formulated for several blends of forward-backward Euler’s time schemes with/without filters, under linear or quadratic-hyperbolic rate of change. Eight convergence criteria for time integration are built on the non-redundant Δt -dependent conditions.

The SPH Time-Space Ensemble (SPH-TSE) filter combines the SPH (spatial) kernel with an exponential-decaying SPH time kernel of memory-loss factor a_{mem} . The ensemble mean of a generic quantity A is the weighted sum of the spatial filter over the RANS TKE-averaged eddy size among all the turbulent vortices l_0 (m) and the ensemble mean at the previous time step, at the same point:

$$\bar{A} \Big|_k \approx a_{mem,k} \langle A \rangle_{l_0,k} + (1 - a_{mem,k}) \bar{A} \Big|_{k-1}; \quad a_{mem,k} \approx \begin{cases} 1 - e^{-\frac{\min\{\Delta t_k, T_{L,k}\}}{T_{L,k}}}, & T_{L,k} \leq (t_k - t_{IC}) \\ 1 - e^{-\frac{\min\{\Delta t_k, (t_k - t_{IC})\}}{(t_k - t_{IC})}}, & 0 < (t_k - t_{IC}) < T_{L,k} \end{cases} \quad (2.6)$$

where the subscript ‘ $_{IC}$ ’ denotes Initial Conditions and T_L (s) is the Lagrangian integral time scale of turbulence. Under RANS-SPH simulations, the SPH-TSE filter corrects the ensemble statistics during the post-processing stage of the code algorithm and its difference with the SPH filter feeds a convergence criterion to stationary conditions. Under ILES-SPH simulations, the SPH-TSE filter is also used to convert the output LES-filtered quantities into Reynolds’ ensemble statistics and to assess

the higher-order ensemble moments, the ensemble probability density function and the ensemble cumulative density function. The ensemble statistics for Solid Dynamics are computed via the SPH time filter. In other turbulence approaches, the SPH-TSE filter might convert the output instantaneous-like quantities into Reynolds' statistics.

The SPH filter applies to all the derivatives in the BEs and to the functions needing filtering. The SPH filters of a generic function, gradient and ‘quasi-Laplacian’ (i.e. the divergence of the product of the function gradient by a scalar g) consider contributions from fluid particles ‘ b ’, solid particles ‘ s ’ and fixed-wall elements ‘ w ’ in the SPH neighbourhood of the computational particle. The SPH filter of the gradient of a generic function f is represented by a C₁-consistent SPH quadrature formula:

$$\begin{aligned} \langle \nabla f \rangle_{C1,0} = & \underline{\underline{B}}_0 \left\{ \sum_b (f_b - f_0) \nabla W_b \omega_b + \sum_s (f_{0s} - f_0) \nabla W_s \omega_s + \right. \\ & \left. + \sum_w (f_{0w} - f_0) \underline{T}_w G_{c,0w} + \sum_w \left\{ \underline{T}_w \left\{ G_{l,0w} \left[\underline{T}_w^T (\nabla f)_{0w} \right] \right\} \right\} \right\} \end{aligned} \quad (2.7)$$

where $\underline{\underline{B}}_0$ is a renormalisation matrix, built with inner and boundary terms, and \underline{T}_w is the matrix of the directional cosines of the fixed-wall element.

The SPH filter of the quasi-Laplacian is a C₀-consistent SPH quadrature formula:

$$\begin{aligned} \langle \nabla \cdot [g \nabla f] \rangle_{C0,0} = & -2g_0 \sum_{b \neq 0} \frac{2\bar{\rho}_b^* g_b}{\rho_0 g_0 + \rho_b g_b} \frac{(f_b - f_0)}{r_{0b}} \frac{\partial W}{\partial r} \Big|_b \omega_b + \\ & -2g_0 \sum_{s \neq 0} \frac{(f_{0s} - f_0)}{r_{0s}} \frac{\partial W}{\partial r} \Big|_s \omega_s - 2g_0 \sum_w (f_{0w} - f_0) L_{c,0w}; \quad \bar{\rho}_b^* \equiv \begin{cases} 0.5(\bar{\rho}_0 + \bar{\rho}_b), & f \equiv \bar{C} \\ \bar{\rho}_b, & \text{otherwise} \end{cases} \end{aligned} \quad (2.8)$$

where r (m) is the distance from the computational particle. The mathematical expression of the fluid-fluid interaction term in (2.8) is a minor generalisation of a mathematical formula in Di Monaco et al. (2011, [42]). Specific C₁-consistent quadrature formulae apply to positioning-grid barycentres and monitoring points. A kernel-based anti-cluster strategy is used for fluid-fluid and fluid-body interactions. A unified anti-cluster and anti-penetration strategy applies to fluid-wall interactions, based on reactions as numerical collisions. Eq.(2.8) exactly conserves the pollutant mass.

A series of spatial reconstruction schemes applies, included RANS SPH Wall Functions (WFs) and the Sub-Particle Pollutant-Source (SPPS) scheme. WFs depend on three hydraulic-roughness regimes, and the depths of the turbulent Boundary Layer (BL) and of the Neutral Surface BL (NSBL); TKE-BE is adapted to $\bar{\varepsilon}$ WF.

Under fluid flows confined by solid rigid boundaries, the conservative Balance Equation for the particle Control Volume (CV-BE) can be activated to exactly conserve the fluid global volume. CV-BE time integration is ruled by a simple forward-backward Euler's scheme with a post-correction.

$G_{c,0w}$ (m^{-1}), $\underline{G}_{l,0w}$ and $L_{c,0w}$ (m^{-2}) in (2.7) and (2.8) are geometrical quadrature formulae over a single fixed-wall element: they are mentioned in Sec.3.4. Newton-Euler's equations rule Computational Solid Dynamics (CSD). The main parts of those source lines of the current code dealing with Newton-Euler's equations are imported from the code SPHERA v.10.0.0 (RSE SpA, 2022, [43]) and were presented in Amicarelli et al. (2015, [44]), Amicarelli et al. (2020, [45]), Amicarelli et al. (2021, [46]) and Amicarelli et al. (2022, [47]). The solid-body quantities are interpreted as instantaneous and interact with the fluid mean variables. Ensemble averaging only applies to solid bodies under post-processing. The integration of CSD SPH and CFD SPH is alternative to coupling the latter with a CSD solver: such numerical solution is used in many ILES-CFD-SPH studies (e.g., Tagliafierro et al., 2021, [48]).

The main improvement introduced in CFD-OUT-sweePDF v.2.0.0 with respect to the previous code version is the representation of S_{CT} ; secondary novelties concern the SPPS scheme, the truncation outlet sections ‘ T_B ’, the conservative variant to the SPH filter of the quasi-Laplacian in SPH Cm-BE

and a correction to the roughness length z_0 (m) in the intermediate hydraulic-roughness regime. This is now expressed as $z_0 = \frac{(70 - Re_*)}{(70 - 5)} \frac{\bar{v}}{9u_*} + \frac{(Re_* - 5)}{(70 - 5)} \frac{H_{sgr}}{5}$, where u^* (m/s) is the friction velocity (at ground), Re^* is the friction Reynolds number and H_{sgr} (m) is the sub-grid roughness.

3. SPH QUADRATURE FORMULAE

The SPH filter applies to the derivatives of the governing BEs of (2.1)-(2.5). The SPH spatial filters of a generic function (Sec.3.1), gradient (Sec.3.2) and ‘quasi-Laplacian’ (Sec.3.3) consider contributions from fluid particles, solid particles and fixed-wall elements. The latter also depend on geometrical quadrature formulae over a single fixed-wall element (Sec.3.4). A unified anti-cluster and anti-penetration strategy for fluid-wall interactions is represented by reactions modelled as numerical collisions (Sec.3.5, Sec.3.6). The anti-cluster strategy for fluid-fluid and fluid-body interactions (Sec.3.7) is based on a cubic anti-cluster kernel. The SPH quadrature formulae rely on the assessment of relative positions, kernel functions and gradients (Sec.3.7), and are also computed over the barycentres of the positioning grid and the monitoring points (Sec.3.8). Any SPH filter is interpreted as a spatial filter in the continuum plus a 3D open weighted quadrature formula for given irregular nodes (Sec.3.9). The formulations for all the SPH-TSE ensemble statistics and the SPH spatial statistics are completed in Sec.3.10. Each vector component is processed as a generic scalar.

3.1. SPH spatial filter of a generic function

The SPH filter of a generic function f around the computational particle ‘ 0 ’ is represented by the following C₁-consistent SPH quadrature formula:

$$\langle f \rangle_0 = \langle f \rangle_{C1,0} + \left\langle \frac{\partial f}{\partial x_j} \right\rangle_{C1,0} \left(x_{j,0} - \frac{\langle x_j \rangle_{C-1,0}}{\sigma_0} \right), \quad \sigma_0 \equiv \langle 1 \rangle_{C-1,0} \quad (3.1)$$

where σ is the discrete Shepard’s coefficient and the C₋₁ SPH quadrature formula is the straightforward discretisation of the integral SPH filter:

$$\langle f \rangle_{C-1,0} = \sum_b f_b W_b \omega_b + \sum_s f_{0s} W_s \omega_s + \sum_w f_{0w} F_{c,0w} + \sum_w \underline{F}_{l,w} \left[\underline{T}_{l,w}^T (\nabla f)_{0w} \right] \quad (3.2)$$

where the summations of the first line are executed over the volumes ω of the neighbouring fluid ‘ b ’ and solid ‘ s ’ particles which locally discretise the fluid domain and the solid bodies. The fluid-body interaction quantities ‘ $0s$ ’ are synthesized in Sec.3.10 and Sec.4. The following two terms are associated with a summation over the neighbouring elements ‘ w ’ of the fixed walls. The first one represents the quadrature formula for the constant term of the linear Taylor series of f over the portion of the kernel support truncated by the set of the neighbouring fixed-wall elements $V'_{h,w}$ (m³). The last term is associated with the linear term of the same series. The fixed-wall ‘constant’ term depends on the constant boundary function f_{0w} (Sec.3.10) and a geometrical quadrature formula over a single-wall element $F_{c,0w}$ (Sec.3.4). The fixed-wall ‘linear’ term considers the constant boundary gradient $(\nabla f)_{0w}$ (Sec.3.10) and the matrix $\underline{F}_{l,w}$ (m) of the following geometrical quadrature formula over a single wall element, which depends on the portions of solid angle α_s :

$$\underline{F}_{l,w} = \left(\sum_{\Delta\alpha_s} (\nabla r \otimes \nabla r) I_3 \Delta\alpha_s \right)_{0w}, \quad I_3 \equiv \int_{r_{0w}}^{2h} r^3 W dr \quad (3.3)$$

Eq.(3.3) is here formulated, but not used for sake of simplicity. The omission of the fixed-wall ‘linear’ term is equivalent to assume a null gradient over $V'_{h,w}$. The alternative fixed-wall terms in 2D read:

$$\sum_w f_{0w,2D} F_{c,0w,2D} + \sum_w (\nabla f)_{0w} \cdot (\underline{i}_w F_{l1,0w,2D} + \underline{n}_w F_{l2,0w,2D}) \quad (3.4)$$

where \underline{n}_w is the wall-element normal and \underline{l}_w is its perpendicular unit vector. The geometrical quadrature formulae $F_{c,0w,2D}$, $F_{l1,0w,2D}$ (m) and $F_{l2,0w,2D}$ (m) for the fixed-wall constant and linear 2D terms are mentioned in Sec.3.4. The 2D fixed-wall constant $f_{0w,2D}$ assumes the following form:

$$f_{0w,2D} = f_0 + (\nabla f)_{0w} \cdot (\underline{x}_{0w} - \underline{x}_0) \quad (3.5)$$

where \underline{x}_{0w} (m) is the closest position along the wall element ' w ' to the computational particle ' o '.

3.2. SPH spatial filter of the gradient of a generic function

The SPH filter of a gradient is represented by the C₁-consistent SPH quadrature formula (2.7).

The inverse of the renormalisation matrix $\underline{\underline{B}}_0$ is the opposite of the C₀-consistent SPH filter of the gradient of the position of the numerical neighbours (Randles & Libertsky, 1996, [49]):

$$\underline{\underline{B}}_0^{-1} \equiv -\langle \nabla \otimes \underline{x} \rangle_{C0,0} \Leftrightarrow B_{ij,0}^{-1} \equiv -\left\langle \frac{\partial \underline{x}_j}{\partial \underline{x}_i} \right\rangle_{C0,0} \quad (3.6)$$

and here includes boundary contributions. In the continuum, it equals the opposite of the identity matrix, which replaces (3.6) if $\underline{\underline{B}}_0^{-1}$ is bad-conditioned ($|\underline{\underline{B}}_0^{-1}| < 1 \times 10^{-4}$). The C₀-consistent SPH filter:

$$\langle \underline{\nabla} f \rangle_{C1,0} = -\underline{\underline{B}}_0 \langle \nabla f \rangle_{C0,0}, \quad \langle \underline{\nabla} f \rangle_{C0,0} \equiv \langle \nabla (f - f_0) \rangle_{C-1,0} \quad (3.7)$$

depends on the C₋₁ SPH quadrature formula of the integral SPH filter after integration over the fluid, solid-body and fixed-wall subdomains:

$$\langle \underline{\nabla} f \rangle_{C-1,0} = -\sum_b f_b \underline{\nabla} W_b \omega_b - \sum_s f_{0s} \underline{\nabla} W_s \omega_s - \sum_w f_{0w} \underline{\underline{T}}_w G_{c,0w} - \sum_w \left\{ \underline{\underline{T}}_w \left\{ G_{l,0w} \left[\underline{\underline{T}}_w^T (\nabla f)_{0w} \right] \right\} \right\} \quad (3.8)$$

The corresponding 2D fixed-wall terms for (2.7) read:

$$-\underline{\underline{B}}_0 \left[\sum_w (f_{0w,2D} - f_0) \underline{n}_w G_{c,0w,2D} + \sum_w (\nabla f)_{0w} G_{l,0w,2D} \right] \quad (3.9)$$

The geometrical quadrature formulae over a single fixed-wall element $G_{c,0w}$ (m⁻¹) and $G_{l,0w}$ for the fixed-wall constant and linear terms are mentioned in Sec.3.4, together with the corresponding 2D geometrical quadrature formulae $G_{c,0w,2D}$ and $G_{l,0w,2D}$.

3.3. SPH spatial filter of the ‘quasi-Laplacian’ of a generic function

The SPH filter of the divergence of the product of a function gradient by a generic scalar g is mentioned as ‘quasi-Laplacian’ of the function, for sake of simplicity. If the scalar is uniform, the divergence is equal to the product of the scalar by the Laplacian. The SPH filter of the quasi-Laplacian of a function is represented by the C₀-consistent SPH quadrature formula (2.8). It is an extension of the mathematical formula for the inner viscous term of the Momentum Equation reported in Di Monaco et al. (2011, [42]), after the integration of the BC terms and a conservative variant for Cm-BE. The inner term of (2.8) is a combination of Cleary’s and Morris’ formulations (Basa et al., 2009, [50]): the three expressions are equal under homogeneous conditions for the mean density and the scalar. Basa et al. (2009, [50]) demonstrated it is a hybrid SPH-FDM operator, where FDM stands for Finite Difference Method. The linear fixed-wall term is null for sake of simplicity without deteriorating the consistency order. However, under the BCs of Sec.3.10, such term would be null. The integral over a single fixed-wall element $L_{c,0w}$ (m⁻²) is mentioned in Sec.3.4. The filter (2.8) exactly conserves the pollutant mass in every pair-particle subsystem.

3.4. Geometrical quadrature formulae over a single fixed-wall element

This section does not represent an original contribution of the current code: it is mentioned for sake of completeness. The fixed-wall contributions to the SPH quadrature formulae of Sec.3.1-Sec.3.3 also depend on the following geometrical quadrature formulae over a single fixed-wall element: $F_{c,0w}$,

$F_{c,0w,2D}$, $F_{l1,0w,2D}$, $F_{l2,0w,2D}$, $G_{c,0w}$, $\underline{G}_{l,0w}$, $G_{c,0w,2D}$, $G_{l,0w,2D}$ and $L_{c,0w}$. Five of them apply in 2D, the other four in 3D. The main parts of those source lines of the current code dealing with the above-mentioned formulae are imported from the code SPHERA v.10.0.0 (RSE SpA, 2022, [43]) and were presented in Di Monaco et al. (2011, [42]).

3.5. Fluid-wall reactions over fixed-wall faces

The anti-cluster strategy for fluid-fluid and fluid-body interactions, based on the application of the cubic anti-cluster kernel, does not apply to the interactions between fluid and fixed walls (or ‘fluid-wall interactions’, for sake of simplicity) for two reasons. The first is to simplify the algorithm not introducing formulae in Sec.3.4, which relies on the cubic beta-spline kernel. The latter is to represent symmetry conditions without fluid-wall penetrations, under the approximated and fast BC treatment for fixed walls. This need is not shown by the more accurate but slower BC treatment for solid bodies. The solution is the simulation of fluid-wall reactions represented by numerical collisions. They are as smooth as possible in time and space not to alter the fluid fields in the inner domain. The global fluid-wall reaction \underline{R}_{FW} ($\text{kg} \times \text{m} \times \text{s}^{-2}$) for a computational particle interests the neighbouring fixed-wall faces, coherently with the mathematical formula in Di Monaco et al. (2011, [42]):

$$\underline{R}_{FW,0} = \sum_w \underline{R}_{FW,0w} = -m_0 \frac{c_{ref}^2}{h} \sum_w \frac{\underline{r}_{0w}}{|\underline{r}|_{0w}} \cdot \begin{cases} -\ln \left[\frac{h + (d_{0w} - d_{FW,max})}{h} \right], & d_{0w} < d_{FW,max}, \quad \bar{\underline{u}}_{0n} > 0; \\ 0, & \text{otherwise} \end{cases}; \quad (3.10)$$

$$d_{FW,max} \equiv \frac{\Delta x}{4}; \quad \bar{\underline{u}}_{0n} \equiv \bar{\underline{u}}_0 \cdot \underline{n}_w$$

provided that the particle lies within the collision zone of depth $d_{FW,max}$ (m), is approaching the fixed-wall element and meets the wall-face ‘projection visibility criterion’. This is satisfied if the projection of the particle position over the plane/line containing the fixed-wall element in 3D/2D is internal to the element. The quantity Δx (m) is the particle size, whereas d (m) represents any inter-element distance. The advantage of (3.10) is that its limited magnitude makes the approximated stability criterion on fluid-wall reactions (Amicarelli, 2024, [25]) provide an acceptable time discretisation without more constraining criteria, even if this strategy does not strictly guarantee the non-penetration condition under optimised simulations.

3.6. Fluid-wall reactions over fixed-wall edges

This section does not represent an original contribution of the current code: it is mentioned for sake of completeness. To improve the cover of the collision zone around a boundary made of fixed-wall elements, fluid-wall reactions are also computed over fixed-wall edges, only if no fluid-wall reaction is activated on the adjacent fixed-wall faces (Sec.3.5). The number of fluid-wall reactions for fixed-wall edges is normally at least 3 orders of magnitude smaller than the number of fluid-wall reactions for fixed-wall faces. The main parts of those source lines of the current code dealing with fluid-wall reactions for fixed-wall edges are imported from the code SPHERA v.10.0.0 (RSE SpA, 2022, [43]).

3.7. Relative positions, kernel functions and gradients

The current code uses the cubic beta-spline kernel, whose mathematical formulation was presented in Monaghan & Lattanzio (1985, [51]):

$$W = \begin{cases} \frac{1}{\pi h^3} \left(1 - \frac{3}{2}q^2 + \frac{3}{4}q^3 \right), & 0 \leq q < 1 \\ \frac{1}{4\pi h^3} (2-q)^3, & 1 \leq q < 2 \\ 0, & 2 \leq q \end{cases}; \quad \underline{\nabla}W = \begin{cases} \frac{1}{\pi h^4} \left(\frac{9}{4}q^2 - 3q \right) \frac{r}{r}, & 0 \leq q < 1 \\ -\frac{3}{4\pi h^4} (2-q)^2 \frac{r}{r}, & 1 \leq q < 2 \\ 0, & 2 \leq q \end{cases} \quad (3.11)$$

In 2D, W and $\underline{\nabla}W$ are multiplied by $10h/7$. In the inner domain and over the solid bodies, the anti-cluster strategy replaces the kernel gradient of (3.11) in the terms of SPH RANS-ME with the gradient of the cubic anti-cluster kernel, which was mathematically defined in Gallati & Braschi (2000, [52]):

$$W = \begin{cases} \frac{15}{64\pi h^3} (2-q)^3, & 0 \leq q < 2 \\ 0, & 2 \leq q \end{cases}; \quad \underline{\nabla}W = \begin{cases} -\frac{45}{64\pi h^4} (2-q)^2 \frac{r}{r}, & 0 \leq q < 2 \\ 0, & 2 \leq q \end{cases} \quad (3.12)$$

Its kernel function applies to the SPH filter of several functions. In 2D, W and $\underline{\nabla}W$ are multiplied by $4h/3$. The most frequent kernel- and position-related interaction quantities are saved by default in dedicated arrays for fluid-fluid, fluid-body and body-body pair-particle interactions, unless specific pre-processor macros are activated to save the Total Virtual Memory *TVM* (GB) at the expense of the elapsed time t_{ela} (s). Some algorithm details are presented hereafter. The following 6 scalars are assessed and stored every time step, each fluid-fluid pair-particle interaction:

$$\begin{aligned} \text{grad_}_W\text{-fp0_fpn}(1:3) &\equiv \underline{\nabla}W_{\beta s,0b}; \quad W\text{-fp0_fpn} \equiv W_{\beta s,0b} \geq 0; \\ gW2\text{-by_}gW\text{-fp0_fpn} &\equiv \begin{cases} \frac{\underline{\nabla}W_{ac,0b}}{\underline{\nabla}W_{\beta s,0b}} \geq 0, \quad \underline{\nabla}W_{\beta s,0b} \neq 0 \\ 1, \quad \underline{\nabla}W_{\beta s,0b} = 0 \end{cases}; \\ x\text{-by_}gW\text{-fp0_fpn} &\equiv \begin{cases} \frac{\underline{x}_b - \underline{x}_0}{\underline{\nabla}W_{\beta s,0b}} = -\frac{|\underline{x}_b - \underline{x}_0|}{|\underline{\nabla}W_{\beta s,0b}|} = \left(\frac{1}{r_{0b}} \frac{\partial W_{\beta s}}{\partial r} \Big|_{0b} \right)^{-1} < 0, \quad \underline{\nabla}W_{\beta s,0b} \neq 0 \\ 1, \quad \underline{\nabla}W_{\beta s,0b} = 0 \end{cases} \end{aligned} \quad (3.13)$$

Considering the default value $h/\Delta x=1.30$, the average number of SPH fluid neighbours in 3D is ca.75, far from boundaries. The subscripts ‘ βs ’ and ‘ ac ’ refer to the beta-spline and the anti-cluster cubic kernels. The following 5 scalars are updated every time step, each fluid-body pair-particle interaction:

$$\begin{aligned} \text{grad_}_W\text{-fp0_bpn}(1:3) &\equiv \underline{\nabla}W_{\beta s,0s}; \\ gW2\text{-by_}gW\text{-fp0_bpn} &\equiv \begin{cases} \frac{\underline{\nabla}W_{ac,0s}}{\underline{\nabla}W_{\beta s,0s}} \geq 0, \quad \underline{\nabla}W_{\beta s,0s} \neq 0 \\ 1, \quad \underline{\nabla}W_{\beta s,0s} = 0 \end{cases}; \\ x\text{-by_}gW\text{-fp0_bpn} &\equiv \begin{cases} \frac{\underline{x}_s - \underline{x}_0}{\underline{\nabla}W_{\beta s,0s}} = -\frac{|\underline{x}_s - \underline{x}_0|}{|\underline{\nabla}W_{\beta s,0s}|} = \left(\frac{1}{r_{0s}} \frac{\partial W_{\beta s}}{\partial r} \Big|_{0s} \right)^{-1} < 0, \quad \underline{\nabla}W_{\beta s,0s} \neq 0 \\ 1, \quad \underline{\nabla}W_{\beta s,0s} = 0 \end{cases} \end{aligned} \quad (3.14)$$

The following 3 scalars are updated every time step, each body-body pair-particle interaction:

$$x\text{-bp0_bpn}(1:3) \equiv \underline{x}_{sb} - \underline{x}_{s0} \quad (3.15)$$

The subscripts ‘ $s0$ ’ and ‘ sb ’ refer to the computational body particle and the neighbouring body particle, respectively. Any other kernel function is always computed on the fly. The activation of the pre-processor macro ‘*ON THE FLY grad_W_fp0_fp*n’ in compile-time makes ‘*grad_W_fp0_fp*n’

be computed on the fly. The analogous activation of the macro ‘*ON_THE_FLY_OTHERS*’ makes ‘*gW2_by_gW_fp0_fn*’, ‘*x_by_gW_fp0_fn*’ and ‘*W_fp0_fn*’ be computed on the fly as well.

3.8. SPH quadrature formulae for positioning-grid barycentres and monitoring points

For sake of efficiency in terms of *TVM* and *tela*, the C₁-consistent SPH quadrature formula used to assess a spatial average over a barycentre ‘*gp*’ of the positioning grid or a monitoring point relies on the statistics already computed at the nearest SPH particle ‘*np*’, boundary terms included:

$$\langle f \rangle_{C1, gp} = \frac{\langle f \rangle_{C-1, np}}{\sigma_{np}} + \left\langle \frac{\partial f}{\partial x_j} \right\rangle_{C1, np} \left(x_{j, gp} - \frac{\langle x_j \rangle_{C-1, np}}{\sigma_{np}} \right) \quad (3.16)$$

where Einstein’s summation convention applies to the subscript ‘*j*’. Eq.(3.16) is used in the memory-loss term of the SPH-TSE filter. Besides the SPH and SPH-TSE filters, even the nearest-particle method applies to monitoring points, for post-processing purposes, with the following motivation. Under almost-discontinuous spatial fields, the nearest-particle unfiltered ‘raw’ value at a generic monitoring point converges faster than the SPH and SPH-TSE filters: the ‘raw’ values are then preferred to avoid finer Δx . However, the nearest-particle method might be too inaccurate depending on the nearest-particle distance from the monitor and the field inhomogeneity. Thus, when using a ‘raw’ profile, the target field has to be almost discontinuous and a comparison with the associated SPH-TSE profile has to support the reliability of the profile obtained by the nearest-particle method.

3.9. SPH filter: a spatial filter in the continuum plus a 3D open weighted quadrature formula for given irregular nodes

Each of the three SPH filters (Sec.3.1–Sec.3.3) is interpreted as a spatial filter in the continuum ‘ $\hat{\cdot}$ ’, plus a 3D open weighted quadrature formula for given irregular nodes. The quadrature formula is open because the particle position strictly lies within the particle volume, not over its edges. The nodes are given because the particle trajectories are computed and not arbitrarily chosen, except for minor displacements induced by the stabilisation terms. The SPH filters are formally revised hereafter to demonstrate the interpretation above. A generic weighted quadrature formula reads:

$$\int_V f dV \approx \sum_b f_b \gamma_b \quad (3.17)$$

where γ_b are the coefficients or weights computed over the nodes ‘*b*’, represented by the neighbouring particles in CFD-SPH. In the following, the definition (3.17) applies to the SPH filters for the function, the gradient and the quasi-Laplacian, far from boundaries for sake of synthesis.

The SPH filter for a generic function (3.1)–(3.2) is interpreted as a spatial filter in the continuum plus a C₁-consistent 3D open weighted quadrature formula for given irregular nodes:

$$\begin{aligned} \hat{f}_{x_0} &= \int_{V_h} f W dV \approx \sum_b f_b W_b \gamma_b, \quad \gamma_{b \neq 0} = \frac{\omega_b}{\sigma_0} + \frac{\left(\underline{B}_0 \nabla W_b \omega_b \right)}{W_b} \cdot \left(x_0 - \frac{\sum_b x_b W_b \omega_b}{\sigma_0} \right), \\ \gamma_{b=0} &= \frac{\omega_0}{\sigma_0} - \frac{\left(\underline{B}_0 \sum_{b \neq 0} \nabla W_b \omega_b \right)}{W_0} \cdot \left(x_0 - \frac{\sum_b x_b W_b \omega_b}{\sigma_0} \right) \end{aligned} \quad (3.18)$$

where the convolution kernel is *W*. The analogous formula with Gaussian weights and chosen nodes is the C₁-consistent formula of Gauss-Hermite. Under ICs, the SPH nodes are set by the code in a regular Cartesian distribution to reduce the SPH truncation errors. Under these conditions and

virtually assuming a top-hat kernel, not suggested for SPH simulations, the SPH quadrature formula (3.18) would be equivalent to a trilinear interpolation.

Statistics	\underline{f}_{0s}	\underline{f}_{0w}	$(\nabla \otimes \underline{f})_{0w}$
$\left\langle \nabla \cdot \left[(\bar{\nu} + \nu_T) (\nabla \otimes \bar{u})^T \right] \right\rangle_{C0}$	\bar{u}_{0s}	\bar{u}_{0w}	$\underline{\underline{0}}$
$\langle \bar{u} \rangle_{C1}, \left\langle (\nabla \otimes \bar{u})^T \right\rangle_{C1}, \langle \nabla \cdot \bar{u} \rangle_{C1}, \langle \bar{u} \rangle_{(h, T_L)}$	\bar{u}_{0s}	\bar{u}_{0w}	$\underline{\underline{0}}$
$\langle \bar{p} \rangle_{C1}, \langle \nabla \bar{p} \rangle_{C1}, \langle \bar{p} \rangle_{(h, T_L)}$	\bar{p}_{0s}	\bar{p}_{0w}	$(\nabla \bar{p})_{0w}$
$\left\langle \nabla \cdot \left(\frac{\nu_T}{\sigma_\rho} \nabla \bar{\rho} \right) \right\rangle_{C0}$	$\bar{\rho}(\bar{p}_{0s})$	$\bar{\rho}_0$	$\underline{\underline{0}}$
$\left\langle \nabla \cdot \left[\left(\frac{\bar{\nu}}{\nu} + \frac{\nu_T}{\sigma_q} \right) \nabla \bar{q} \right] \right\rangle_{C0, SH^*}$	\bar{q}_0	\bar{q}_0	$\underline{\underline{0}}$
$\left\langle \nabla \cdot \left[\left(\frac{\bar{\nu}}{\nu} + \frac{\nu_T}{\sigma_\varepsilon} \right) \nabla \bar{\varepsilon} \right] \right\rangle_{C0}$	$\bar{\varepsilon}_0$	$\bar{\varepsilon}_0$	$\underline{\underline{0}}$
$\langle \bar{q} \rangle_{C1}, \langle \bar{q} \rangle_{C0}, \langle \nabla \bar{q} \rangle_{C1}, \langle \bar{q} \rangle_{(h, T_L)}$	\bar{q}_{0s}	\bar{q}_0	$(\nabla \bar{q})_{0w}$
$\langle \bar{\varepsilon} \rangle_{C1}, \langle \bar{\varepsilon} \rangle_{(h, T_L)}$	0	0	$\underline{\underline{0}}$
$\left\langle \nabla \cdot \left[\left(D_M + \frac{\nu_T}{Sc_T} \right) \nabla \bar{C} \right] \right\rangle_{C0}$	\bar{C}_0	\bar{C}_0	$\underline{\underline{0}}$
$\langle \bar{C} \rangle_{C1}, \langle \bar{C} \rangle_{(h, T_L)}$	0	0	$\underline{\underline{0}}$
$\langle \nabla \bar{1} \rangle_{C-1}$	1	1	$\underline{\underline{0}}$
$\langle \bar{p} \rangle_{C0}$	\bar{p}_{0s}	\bar{p}_{0w}	$\underline{\underline{0}}, 3D$ $(\nabla \bar{p})_{0w}, 2D$
$\langle \nabla \otimes \bar{x} \rangle_{C0}$	\underline{x}_s	$\underline{x}_0, 3D$ $\underline{x}_{0w}, 2D$	$\underline{\underline{I}}$
$\langle \bar{t}_{FP} \rangle_{C1}, \langle \bar{t}_{FP} \rangle_{(h, T_L)}$	0	0	$\underline{\underline{0}}$
$\langle \nabla \bar{p} \rangle_{REC}, \langle \nabla \bar{q} \rangle_{REC}$	0	0	$\underline{\underline{0}}$

Table 3.1. RANS SPH-TSE ensemble statistics and SPH spatial statistics. Column 1 (from left to right): list of the SPH spatial statistics at the positions of the fluid particles, monitors and grid barycentres, and the SPH-TSE ensemble statistics $\langle \rangle_{(h, T_L)}$ at the monitors and grid barycentres. Each group of statistics is associated with the boundary quantities formulated for solid bodies (column 2) and fixed walls (columns 3 and 4). The last row refers to the reconstructing ‘REC’ gradients used by the reconstruction schemes of Sec.4.

The SPH filter for the gradient of a generic function (2.7) is interpreted as a spatial filter of f in the continuum plus a C₁-consistent 3D open weighted quadrature formula for given irregular nodes:

$$\begin{aligned} \widehat{\nabla f}_{x_0} &= \int_{V_h} (\nabla f) W dV = - \int_{V_h} f (\nabla W) dV \approx \sum_b f_b (\nabla_i W)_b \gamma_{i,b}, \\ \gamma_{i,b \neq 0} &= \frac{(\underline{B}_0 \nabla W_b)_i}{(\nabla W_b)_i} \omega_b, \quad (\gamma \nabla W)_{i,b=0} = - \left(\underline{B}_0 \sum_{b \neq 0} \nabla W_b \omega_b \right)_i, \quad i = 1, 2, 3 \end{aligned} \quad (3.19)$$

where the convolution kernels are the opposites of the components ‘ i ’ of the SPH kernel gradient. In 2D the boundary treatment of fixed walls of the code of Sec.2 relies on a different integration approach with respect to 3D, merging boundary surface and line integrals after a double integration by parts. The overall 2D integral SPH spatial filter of a gradient reads:

$$\left(\widehat{\nabla f} \right)_{2D} = \int_{V_h} (\nabla f) W dV = - \int_{V_h, IN, BD} (\nabla W) f dV - f_0 \int_{A_h} W n dA + (\nabla f)_0 \int_{V_h} W dV \quad (3.20)$$

where the subscripts ‘ IN ’ and ‘ BD ’ represent the fluid subdomain and the subdomain of the solid bodies, respectively, whereas A_h (m, 2D) is the intersection between the set of fixed-wall neighbours and the kernel support of the fluid computational particle.

The SPH filter for the ‘quasi-Laplacian’ of a generic function (2.8) might be interpreted as a spatial filter in the continuum plus a C_0 -consistent 3D open weighted quadrature formula for given irregular nodes, provided that one could find a more proper definition to the convolution kernel X :

$$\begin{aligned} \left(\widehat{\nabla \cdot [g \nabla f]} \right)_{x_0} &= \int_{V_h} [\nabla \cdot (g \nabla f)] W dV \approx \sum_b f_b X_b \gamma_b, \quad (\gamma X)_{b \neq 0} = -4 \frac{\bar{\rho}_b g_0 g_b}{g_0 \bar{\rho}_0 + g_b \bar{\rho}_b} \frac{1}{r_{0b}} \frac{\partial W}{\partial r} \Big|_b \omega_b, \\ (\gamma X)_{b=0} &= 2g_0 \sum_{b \neq 0} \frac{2\bar{\rho}_b g_b}{g_0 \bar{\rho}_0 + g_b \bar{\rho}_b} \frac{1}{r_{0b}} \frac{\partial W}{\partial r} \Big|_b \omega_b \Rightarrow \int_{V_h} [\nabla \cdot (g \nabla f)] W dV \approx \int_{V_h} f X dV \end{aligned} \quad (3.21)$$

Such complication is due to the hybrid SPH-FDM nature of this filter (Sec.3.3).

3.10. RANS SPH-TSE ensemble statistics, SPH spatial statistics and boundary quantities

Table 3.1 shows the synthetic list of RANS SPH-TSE ensemble statistics and SPH spatial statistics with their boundary quantities. The spatial statistics are the applications of the SPH filters for functions (3.1)–(3.2), gradients (2.7) and quasi-Laplacians (2.8). The boundary quantities with double subscript in the last three columns are formulated either in the previous subsections or in Sec.4.

No assumption is needed on the SPH kernel to keep C_1 -consistency in (2.7) and (3.1): any W can be used, included a hybrid combination of kernels. This implies the following conditions: the SPH filters of the mean-pressure and mean-TKE gradients are C_1 -consistent, even if the cubic beta-spline kernel always applies beyond the fixed walls; the SPH filters of the mean pressure and the mean TKE are C_1 -consistent even if computed with a kernel function slightly incoherent with its gradient, which is also hybrid (being partly ‘beta-spline’ beyond fixed walls, partly ‘anti-cluster’). This approach is even justified by the role of the anti-cluster kernel, which is interpreted as an anti-cluster filter applied to the cubic beta-spline kernel in the inner domain and over the solid bodies.

4. SPATIAL RECONSTRUCTION SCHEMES FOR MEAN PRESSURE, TKE AND CONCENTRATION

The boundary values of the mean pressure, the mean TKE and their gradients (Table 3.1) are assessed by C_1 -consistent spatial reconstruction schemes (Sec.4.1, Sec.4.2). They feature any point ‘ BC ’ in the outer portions of the SPH kernel support of the computational particle ‘ o ’ that lie in the solid subdomain. The boundary mean-TKE gradient is also needed by the reconstruction scheme for \bar{p}_{BC} . The spatial reconstruction scheme for the mean concentration at the PS is reported in Sec.4.3. The reconstruction schemes in RANS-SPH are analogous to the ILES-SPH reconstruction schemes but

the first are free from any sub-particle energy dissipation, which is intrinsically related to the ILES-SPH Riemann's solvers (e.g., Gu et al., 2017, [53]).

4.1. C₁-consistent mean pressure and its gradient at fluid-solid interfaces

The spatial reconstruction scheme for the mean pressure and its gradient at fluid-solid interfaces is described in the following. Free-slip conditions at any fluid-solid interface are featured by in-built motion of the fluid ' F ' and the solid ' S ' sides along the wall normal \underline{n}_{wall} :

$$\underline{a}_{wall,F} \cdot \underline{n}_{wall} = \underline{a}_{wall,S} \cdot \underline{n}_{wall} \quad (4.1)$$

where \underline{a} (m/s²) is the acceleration. The subscript ' $wall$ ' refers to any fluid-solid interface including both solid bodies and fixed walls in the continuum, contrarily to ' w ' which relates to a single discrete element of a fixed wall. All the kinematic quantities related to the solid subdomains are assumed as instantaneous and free from turbulent fluctuations during the resolution of the BEs of the fluid subdomain. The ensemble average of (4.1) is then obtained as follows:

$$\overline{\underline{a}_{wall,F} \cdot \underline{n}_{wall}} = \overline{\underline{a}_{wall,S} \cdot \underline{n}_{wall}} \Rightarrow \overline{\underline{a}_{wall,F} \cdot \underline{n}_{wall}} \approx \overline{\underline{a}_{wall,S} \cdot \underline{n}_{wall}} \quad (4.2)$$

After neglecting the diffusion term (unlike the ILES-SPH reconstruction scheme of Cercos-Pita et al., 2017, [54]) and assuming WC or incompressible conditions, the fluid mean acceleration reads:

$$\overline{\underline{a}_{wall,F}} = -\frac{1}{\overline{\rho}} \nabla \overline{p} \Big|_{\underline{x}_{wall}} + \underline{g} - \frac{2}{3} (\nabla \overline{q}) \Big|_{\underline{x}_{wall}} \quad (4.3)$$

The linearity assumption for the mean-pressure field implies the following relationships:

$$\overline{p}_{BC} = \overline{p}_{wall} + \nabla \overline{p} \Big|_{\underline{x}_{wall}} \cdot (\underline{x}_{BC} - \underline{x}_{wall}), \quad \overline{p}_0 = \overline{p}_{wall} + \nabla \overline{p} \Big|_{\underline{x}_{wall}} \cdot (\underline{x}_0 - \underline{x}_{wall}) \quad (4.4)$$

The system (4.1)–(4.4) permits to derive an expression for the boundary mean pressure as follows:

$$\begin{aligned} \overline{p}_{BC} &= \overline{p}_0 + \nabla \overline{p} \Big|_{\underline{x}_{wall}} \cdot (\underline{x}_{BC} - \underline{x}_0) = \overline{p}_0 + \overline{\rho}_{wall} \left[\left(\underline{g} - \underline{a}_{wall,S} - \frac{2}{3} (\nabla \overline{q})_{wall} \right) \cdot \underline{n}_{wall} \right] \underline{n}_{wall} \cdot (\underline{x}_{BC} - \underline{x}_0) \\ &\quad + \left\{ \nabla \overline{p} \Big|_{\underline{x}_{wall}} - \overline{\rho}_{wall} \left[\left(\underline{g} - \underline{a}_{wall,S} - \frac{2}{3} (\nabla \overline{q})_{wall} \right) \cdot \underline{n}_{wall} \right] \underline{n}_{wall} \right\} \cdot (\underline{x}_{BC} - \underline{x}_0) \end{aligned} \quad (4.5)$$

Under C₁ consistency for \overline{p} , the following assumptions are also flawless:

$$\overline{\rho}_{wall} = \overline{\rho}_0, \quad \underline{a}_{wall,S} = \underline{a}_{BC}, \quad \nabla \overline{p} \Big|_{\underline{x}_{wall}} = \nabla \overline{p} \Big|_{\underline{x}_0}, \quad \langle \nabla \overline{p} \rangle_0 = \langle \nabla \overline{p} \rangle_{REC,0} \quad (4.6)$$

where $\langle \nabla \overline{p} \rangle_{REC}$ (Pa/m) is the reconstructing 'REC' mean-pressure gradient. Under free-slip conditions, the tangential component of $\nabla \overline{p}$ does not depend on the interface acceleration and symmetry conditions are set for \overline{q} ; the reconstructed mean pressure reads:

$$\begin{aligned} \overline{p}_{BC,free-slip} &= \overline{p}_0 + \langle \nabla \overline{p} \rangle_{BC,free-slip} \cdot (\underline{x}_{BC} - \underline{x}_0), \\ \langle \nabla \overline{p} \rangle_{BC,free-slip} &= \langle \nabla \overline{p} \rangle_{REC,0} + \left\{ \overline{\rho}_0 \left(\underline{g} - \underline{a}_{BC} \right) - \langle \nabla \overline{p} \rangle_{REC,0} \right\} \cdot \underline{n}_{wall}, \quad \left. \frac{\partial \overline{q}}{\partial \underline{n}_{wall}} \right|_{wall} = 0 \end{aligned} \quad (4.7)$$

Under no-slip conditions, the in-built motion is imposed along any direction as follows:

$$\begin{aligned} \overline{\underline{a}}_{wall,F} &= \underline{a}_{wall,S} \Rightarrow \overline{p}_{BC,no-slip} = \overline{p}_0 + \langle \nabla \overline{p} \rangle_{BC,no-slip} \cdot (\underline{x}_{BC} - \underline{x}_0), \\ \langle \nabla \overline{p} \rangle_{BC,no-slip} &= \overline{\rho}_0 \left(\underline{g} - \underline{a}_{BC} - \frac{2}{3} (\nabla \overline{q}) \right), \quad \left. \frac{\partial \overline{q}}{\partial \underline{n}_{wall}} \right|_{SBL} = 0 \end{aligned} \quad (4.8)$$

where the last equality comes from WFs. Under general slip conditions, \overline{p}_{BC} is assumed as a linear combination of the no-slip and free-slip formulae, weighted on the slip coefficient ϕ and its complement to the unity. The reconstructed boundary mean pressure and its gradient read:

$$\bar{p}_{BC} = \bar{p}_0 + \langle \underline{\nabla p} \rangle_{BC} \cdot (\underline{x}_{BC} - \underline{x}_0), \quad \langle \underline{\nabla p} \rangle_{BC} = \phi_s \langle \underline{\nabla p} \rangle_{BC, no-slip} + (1 - \phi_s) \langle \underline{\nabla p} \rangle_{BC, free-slip} \quad (4.9)$$

Hereafter the reconstructing mean-pressure gradient in (4.7) is formulated. It only involves inner terms ‘*IN*’ to avoid recursion. Under this scope, SPH RANS-CE needs a C₁-consistent SPH filter:

$$\langle \underline{\nabla p} \rangle_{REC,0,CE} = \underline{\underline{B}}_{0,IN} \sum_b (\bar{p}_b - \bar{p}_0) \underline{\nabla W}_b \omega_b \quad (4.10)$$

where the beta-spline cubic kernel applies. Eq.(4.10) is used in (4.7) to complete the correction stage of RANS-CE and to initialise the surfaces of the solid bodies. It cannot work for SPH RANS-ME for two reasons: it would alter the slip conditions, affecting the inner contribution to the tangential component of the mean-pressure gradient under free-slip conditions; it would introduce some inconsistency as the reconstruction applies before the renormalisation. In SPH RANS-ME, (4.10) is thus replaced by an extrapolation via σ of the temporary C₀-consistent inner term of $\underline{\nabla p}$:

$$\langle \underline{\nabla p} \rangle_{REC,0,ME} = \frac{\langle \underline{\nabla p} \rangle_{C0,0,IN}}{\sigma_{0,IN}} = - \frac{\sum_b (\bar{p}_b - \bar{p}_0) \underline{\nabla W}_b \omega_b}{\sigma_{0,IN}} \quad (4.11)$$

where the cubic anti-cluster kernel substitutes the cubic beta-spline kernel.

4.2. C₁-consistent mean TKE and its gradient at fluid-solid interfaces

The spatial reconstruction scheme for the mean TKE and its gradient at fluid-solid interfaces is described hereafter. The symmetry condition on \bar{q} applies to the fluid-solid interface ‘*wall*’ and approximately also to its neighbourhood. The resulting boundary mean-TKE gradient reads:

$$(\underline{\nabla q})_{BC} \approx \langle \underline{\nabla q} \rangle_{REC,0} - \left[\langle \underline{\nabla q} \rangle_{REC,0} \cdot \underline{n}_{wall} \right] \underline{n}_{wall}, \quad \left. \frac{\partial \bar{q}}{\partial \underline{n}_{wall}} \right|_{wall} = 0 \quad (4.12)$$

The reconstructing mean-TKE gradient $\langle \underline{\nabla q} \rangle_{REC,0}$ (m/s²) is formulated as the analogous quantity for the mean pressure, by replacing \bar{p} with \bar{q} in (4.10) and (4.11). Under no-slip conditions, (4.12) is more accurate because the WF-driven mean-TKE gradient is null all over the NSBL.

The boundary mean TKE for any fluid-body inter-particle interaction reads:

$$\bar{q}_{0s} = \bar{q}_0 + (\underline{\nabla q})_{0s} \cdot (\underline{x}_s - \underline{x}_0), \quad (\underline{\nabla q})_{0s} = \langle \underline{\nabla q} \rangle_{REC,0} - \left[\langle \underline{\nabla q} \rangle_{REC,0} \cdot \underline{n}_{0s} \right] \underline{n}_{0s} \quad (4.13)$$

whereas the boundary mean-TKE for a fluid-wall interaction assumes the following expression:

$$\begin{aligned} \bar{q}_{BC,0w} &= \bar{q}_{0w} + \langle \underline{\nabla q} \rangle_{0w} \cdot (\underline{x}_{BC} - \underline{x}_0), \\ \bar{q}_{0w} &= \bar{q}_0, \quad (\underline{\nabla q})_{0w} = \langle \underline{\nabla q} \rangle_{REC,0} - \left[\langle \underline{\nabla q} \rangle_{REC,0} \cdot \underline{n}_{0w} \right] \underline{n}_{0w} \end{aligned} \quad (4.14)$$

4.3. Emission scheme: numerical mean concentration at the Pollutant Source

Unlike the mesh-based CFD codes for Air Quality (e.g. Efthimiou et al., 2016, [55]), the code of Sec.2 adopts a simpler emission scheme to represent the Pollutant Source, exploiting the Lagrangian approach of the SPH method for sake of efficiency. The emission model for the particle mean concentration at the PS represents a spatial reconstruction scheme which applies if the following conditions are met: the mean pollutant-mass flow rate at source \bar{Q}_{PS} (kg/s) is known; either the emission mean velocity is assumed uniform or the explicit modelling for jet intrusions in atmosphere is not mandatory. The resulting model is an emission scheme under uniform (specific mean) pollutant-mass flow rate. Unless otherwise stated, the PS is hereafter a point or a surface source, and lies within the physical inlet section or slightly downstream, as clarified later.

A physical PS is featured by its input flow rate \bar{Q}_{PS} and area A_{PS} (m^2), and assumes a uniform specific mean pollutant-mass flow rate at source $\bar{\Theta}_{PS}$ ($kg/s/m^2$). The resulting \bar{C} at PS varies with \bar{u} over the local coordinates η (m) and ζ (m) within the plane of the PS. This is assumed normal to the direction of the spatially-averaged mean velocity around the PS. In the discrete, the equivalent ' $_{eq}$ ' numerical source adopts analogous conditions and represents the correct physical flow rate \bar{Q}_{PS} by construction:

$$\begin{cases} \bar{Q}_{PS,eq} = \sum_{iPS=1}^{n_{pPS}} \bar{\Theta}_{PS,eq} \Delta \eta_{iPS} \Delta \zeta_{iPS} \approx \sum_{iPS=1}^{n_{pPS}} \bar{C}_{iPS} (-\underline{n}_{inlet} \cdot \bar{u}_{iPS}) \Delta \eta_{iPS} \Delta \zeta_{iPS} \\ \bar{\Theta}_{PS,eq} \text{ uniform} \Rightarrow \bar{\Theta}_{PS,eq} = \frac{\bar{Q}_{PS,eq}}{A_{PS,eq}}, \quad A_{PS,eq} \equiv \sum_{iPS=1}^{n_{pPS}} \Delta \eta_{iPS} \Delta \zeta_{iPS} \approx n_{pPS} (\Delta x)_{loc}^2 \end{cases} \Rightarrow \bar{C}_{iPS} = \frac{\bar{Q}_{PS}}{(-\underline{n}_{inlet} \cdot \bar{u}_{iPS}) n_{pPS} (\Delta x)_{loc}^2}, \quad \bar{Q}_{PS,eq} = \bar{Q}_{PS} \quad (4.15)$$

The subscript ' iPS ' denotes i^{th} position associated with the PS in the 2D time-independent emission pattern of the inlet particles and n_{pPS} is the number of such positions. If no point is detected as internal to the PS volume, the closest position in the pattern is selected. All the particles emitted by the points defined above are called PS inlet particles. It is the inlet particles which cross a PS at some time during their travel. The approximation symbols in (4.15) are due to considering null concentration fluctuations at source. The particle volume is locally assumed uniform and isotropic.

If the PS lies downstream the inlet section, then the following procedures integrate the model above. The numerical volume of the PS is extruded from the PS 2D surface to the inlet section and cannot overlap with other numerical volumes of PSs. The inlet section is defined to be almost parallel to the plane containing the 2D PS surface. SPH Cm-BE is frozen within the inlet region. Downstream, SPH Cm-BE is frozen if the particle flight time t_{FLY} (s) is smaller than the maximum frozen flight time $t_{FLY,FRO,max}$ (s). This is defined to make the PS particles hold null \bar{C} until reaching the physical PS:

$$t_{FLY,FRO,max,PS} = \frac{d_{PS,inlet}}{|\bar{u}|_{inlet,\eta_{PS},\zeta_{PS}}}, \quad d_{PS,inlet} = d_{PS,PHYinlet} + L_{inlet}, \quad L_{inlet} = \left[\int \left(4 \frac{h}{\Delta x} \right) + 1 \right] \Delta x + \frac{\Delta x}{2} \quad (4.16)$$

where $t_{FLY,FRO,max}$ depends on the PS. The velocity value in (4.16) is approximated by the corresponding time-dependent value of the first PS position detected by the code in the time-independent pattern of the inlet particles. The distance between the physical PS and the most upstream layer of inlet particles $d_{PS,inlet}$ (m) is the distance between the physical PS and the physical inlet section ' $PHYinlet$ ', increased by the length of the inlet region L_{inlet} (m). This is approximately equal to $4h$ plus half the particle size. The physical PS has to be close enough to the inlet section to satisfy the following conditions: no other physical PS affects the flow upstream the current PS; the flow locally satisfies Taylor's translation hypothesis for turbulence. The latter considers that the accumulated effect of the stream-wise relative dispersion is negligible and that the mean flow is locally almost 1D. Under these conditions, the local mean velocity at source can be approximately replaced by the inlet mean velocity at the same inlet local coordinates, for the assessments of \bar{C}_{iPS} in (4.15) and $t_{FLY,FRO,max}$ in (4.16). The mean velocity of a PS particle is deemed almost uniform along its trajectory between the numerical inlet section and the physical PS. Any pollutant-mass flux between a computational particle and a neighbouring particle having SPH Cm-BE frozen is inhibited to conserve the pollutant mass. The PS numerical geometry and $t_{FLY,FRO,max}$ are optimise to reduce the distance between the barycentres of the numerical equivalent PS and of the physical PS. A convergence criterion for each distance component is $2\Delta x$. Multiple PSs are treated. Volume PSs are permitted, provided that they belong to the physical inlet section and only extend in the inlet region up to the numerical inlet section. Volume PSs have null $t_{FLY,FRO,max}$. The simulated PSs are stationary. Initial Conditions and the inlet Boundary Conditions can impose additional time-dependent background concentrations.

5. CLOSURE OF THE BALANCE EQUATION FOR THE MEAN CONCENTRATION

The turbulent Schmidt number SCT in (2.5) can be alternatively represented in the code CFD-OUT-sweePDF by the ‘ SCT -const’ approach (Sec.1) or any of three SCT turbulent closures to the BE for the mean concentration (Sec.5.1-5.3). These closures show common features (Sec.5.4) and require the assessment of the peak value of the compensated velocity Lagrangian structure function \tilde{C}_0 (Sec.5.5) and of the weighted ensemble mean of the pollutant flight time \bar{t}_{FP} (Sec.5.6).

SCT -const approach here considers the constant $SCT=0.72$ (Efthimiou et al., 2017, [2]; Venetsanos et al., 2010, [3]; Violeau, 2009, [4]). The use of any constant value for SCT determines a systematic over/underestimation of K_T at small/large \bar{t}_{FP} , although it is the state-of-the-art approach used by deterministic RANS CFD codes. It is equivalent to tune SCT so that an intermediate and constant value is approximately used all over the domain, and hopefully for any test case. The SCT -const approach is responsible for systematic errors in the \bar{C} field, due to neglecting the effects of velocity autocorrelation (out of the turbulent-diffusion regime) and the dependence of SCT on the turbulence Reynolds number Re_T (under any regime of turbulent transport).

The formulations of the SCT -TLS (Sec.5.1), SCT -StHIT (Sec.5.2) and SCT -TGS (Sec.5.3) turbulence closures are reported, being the latter the default option in the current code. SCT -TGS closure analytically satisfies any regime of Taylor’s theory (HIT) and is numerically constrained to grid turbulence and a shear flow. SCT -TGS applies under non-stationary and inhomogeneous conditions, considering local values for \tilde{C}_0 , T_L , R_m , S_m and T_E . The effects of velocity autocorrelation, whose role is revised in Fang et al. (2022, [56]), and the systematic dependence of SCT on Re_T via \tilde{C}_0 are reproduced so that the bias of the state-of-the-art deterministic CFD codes in assessing the mean concentration of passive pollutants is inhibited.

The application of SCT closures is expected to be more effective for Lagrangian than Eulerian CFD codes due to the assessment of the weighted ensemble mean of the pollutant flight time \bar{t}_{FP} (Sec.5.6). It is defined as the ensemble mean of the pollutant flight time, weighted on the instantaneous pollutant mass per unit of volume, but it is approximated by a closed-form solution independent of \bar{C} . Alternative formulations for Eulerian deterministic RANS CFD codes are also proposed. The SCT closures of the code do not depend on the mean-scalar field, but on the properties of the transporting flow and \bar{t}_{FP} , which is here unaffected by the pollutant properties, except for the PS position.

5.1. SCT -TLS turbulence closure

The turbulence closure ‘ SCT -TLS’ stands for Taylor’s equivalent formulation of the turbulent Schmidt number SCT with the Lagrangian integral time scale of turbulence T_L resulting from Langevin’s equation and generalised by Sawford for finite values of the turbulence Reynolds number Re_T (Sawford & Pinton, 2013, [17]; Sawford et al., 2008, [16]). This closure is analytically constrained to Taylor’s theory (Taylor, 1922, [24]), which quantifies the dispersion tensor $\sigma_{x_i^+ x_k^+}^2$ (m^2), i.e. the ensemble covariance of the displacements of fluid particles emitted by the same point (e.g. a point Pollutant Source PS) in different turbulent realisations of the same fluid flow. The superscript ‘ $+$ ’ denotes a Lagrangian variable when it can be confused with an Eulerian quantity. Further integration of molecular diffusion, as in Pope (2011, [57]), provided the following overall expression:

$$\sigma_{x_i^+ x_j^+}^2 = \left\{ 2\sigma_{u_i u_j}^2 T_L \left[t_{FLY} - T_L \left(1 - e^{-\frac{t_{FLY}}{T_L}} \right) \right] + 2D_M t_{FLY} \right\} \delta_{ij} \quad (5.1)$$

where δ_{ij} is Kronecker delta. Eq.(5.1) was derived in the absence of chemical reactions and under HIT, large Re and Taylor’s translation hypothesis for turbulence, i.e. $(\sigma_u \ll \bar{u})$ with uniform mean velocity. Under these conditions, the following statements apply: the flight time t_{FLY} (s) is equal to the weighted

ensemble mean of the pollutant flight time (Sec.5.6); the diagonal components of $\sigma_{x_i^+ x_k^+}^2$ are equal to the squares of the mean-plume spreads along the reference axes. Under HIT, the square of the plume spread is isotropic and the velocity components are uncorrelated: $\sigma_{x_i^+ x_k^+}^2$ equals the product of the identity matrix times the average $\sigma_{\underline{x}^+}^2$ (m^2) of the squares of the plume spreads along the reference axes, which can be rearranged as follows:

$$\sigma_{\underline{x}^+}^2 \equiv \frac{\sigma_{x_k^+}^2}{3} = \frac{4}{3} \bar{q} T_L \left[t_{FLY} - T_L \left(1 - e^{-\frac{t_{FLY}}{T_L}} \right) \right] + 2 D_M t_{FLY}, \quad \bar{q} = \frac{3}{2} \sigma_{u_i}^2 \quad (5.2)$$

where Einstein's summation convention applies to the subscript ' k ', the mean TKE is introduced under HIT. The limit behaviours of (5.2) (Taylor, 1922, [24]; Pope, 2011, [57]) here consider Sawford & Pinton (2013, [17]) expression for T_L and 'k-eps' formula for ν_T :

$$\begin{aligned} \lim_{t_{FLY} \ll \frac{3D_M}{\bar{q}}} \sigma_{\underline{x}^+}^2 &= \sqrt{2 D_M t_{FLY}} \equiv \sigma_{\underline{x}^+, D_M}^2, \quad \lim_{t_{FLY} \gg \frac{3D_M}{\bar{q}}} \sigma_{\underline{x}^+}^2 = \sqrt{\frac{4}{3} \bar{q} T_L \left[t_{FLY} - T_L \left(1 - e^{-\frac{t_{FLY}}{T_L}} \right) \right]} \equiv \sigma_{\underline{x}^+, T}^2, \\ \lim_{o\left(\frac{3D_M}{\bar{q}}\right) \approx t_{FLY} \ll T_L} \sigma_{\underline{x}^+}^2 &= \sqrt{\frac{2}{3} \bar{q} t_{FLY}^2 + 2 D_M t_{FLY}}, \quad \lim_{\frac{3D_M}{\bar{q}} \ll t_{FLY} \ll T_L} \sigma_{\underline{x}^+}^2 = \left(\sqrt{\frac{2}{3}} \bar{q} \right) t_{FLY}, \\ \lim_{t_{FLY} \gg T_L} \sigma_{\underline{x}^+}^2 &= \sqrt{2 \left(\frac{2}{3} \bar{q} T_L + D_M \right) t_{FLY}}, \quad \lim_{\frac{t_{FLY}}{8C_\mu \tilde{C}_0 D_M} \gg T_L} \sigma_{\underline{x}^+}^2 = 2 \sqrt{\frac{\bar{q} T_L}{3}} t_{FLY}, \end{aligned} \quad (5.3)$$

These limits corresponds to the following regimes, respectively: molecular-diffusion regime; turbulent-dispersion regime ' T '; ballistic & molecular-diffusion regime; ballistic regime; molecular-turbulent-diffusion regime; turbulent-diffusion regime. The ODE associated with (5.2) is valid under HIT (Taylor, 1922, [24]):

$$\frac{d\sigma_{\underline{x}^+}^2}{dt_{FLY}} = \frac{4}{3} \bar{q} T_L \left(1 - e^{-\frac{t_{FLY}}{T_L}} \right) + 2 D_M \quad (5.4)$$

Contrarily to (5.2), (5.4) can be approximately used under general conditions with limited errors, since the formulation in ODE form depends on local quantities. RANS Cm-BE analytically determines the following expression for $\sigma_{\underline{x}^+}^2$ under cross-stream-Homogeneous Isotropic Turbulence and Taylor's translation hypothesis for turbulence (Pope, 2011, [57]):

$$\frac{d\sigma_{\underline{x}^+}^2}{dt_{FLY}} = 2 \left(K_T \Big|_{\underline{x}^+} + D_M \Big|_{\underline{x}^+} \right), \quad \sigma_{\underline{x}^+}^2 = 2 \int_0^{t_{FLY}} \left(K_T \Big|_{\underline{x}^+} + D_M \Big|_{\underline{x}^+} \right) dt'_{FLY} \quad (5.5)$$

Hereafter D_M is considered homogeneous without loss of generality for SCT . The near-source linearity of K_T in the stream-wise spatial coordinate guarantees consistency with the ballistic regime under HIT. Imposing the modelled rate of change of the plume spread (5.5) to be equal to the exact value (5.4) under HIT determines the following expression (Taylor, 1922, [24], considering Sawford & Pinton, 2013, [17]):

$$K_T = \frac{8}{9} \frac{\nu_T}{C_\mu \tilde{C}_0} \left(1 - e^{-\frac{t_{FLY}}{T_L}} \right), \quad K_T = \frac{1}{2} \frac{d\sigma_{\underline{x}^+, T}^2}{dt_{FLY}} \quad (5.6)$$

Its limit behaviours are expressed as follows:

$$\lim_{t_{FLY} \ll T_L} K_T = \frac{2}{3} \bar{q} t_{FLY}, \quad \lim_{t_{FLY} \gg T_L} K_T = \frac{2}{3} \bar{q} T_L = \frac{8}{9} \frac{\nu_T}{C_\mu \tilde{C}_0} \quad (5.7)$$

K_T is inhomogeneous under HIT as it depends on \check{t}_{FP} . The SCT -TLS closure to RANS Cm-BE on the turbulent Schmidt number reads (Taylor, 1922, [24], considering Sawford & Pinton, 2013, [17]):

$$Sc_{T,k+1} = \frac{\frac{9}{8}C_\mu\tilde{C}_{0,k+1}}{\left(1 - e^{-\frac{t_{FLY}}{T_L}}\right)_{k+1}}, \quad Sc_T \equiv \frac{\nu_T}{K_T} \quad (5.8)$$

Its limit behaviours are expressed as follows:

$$\begin{aligned} \lim_{t_{FLY} \rightarrow 0} Sc_T &= \infty, \quad \lim_{t_{FLY} \ll T_L} Sc_T = \frac{3}{2} \frac{\nu_T}{q t_{FLY}} = \frac{3}{2} C_\mu \frac{T_E}{t_{FLY}} = \frac{9}{8} C_\mu \tilde{C}_0 \frac{T_L}{t_{FLY}}, \\ \lim_{t_{FLY} \gg T_L} Sc_T &= \frac{9}{8} C_\mu \tilde{C}_0 \equiv Sc_{T,\min} \in \left[0; \frac{9}{8} C_\mu C_0 = 0.658\right] \end{aligned} \quad (5.9)$$

and (5.24) is used for \tilde{C}_0 . In the coded version of Sc_T -TLS, the flight time t_{FLY} is replaced with the weighted ensemble mean of the pollutant flight time \bar{t}_{FP} (s), as defined in Sec.5.6. Under grid turbulence, the modelled rate of change of the plume spread is still represented by (5.5), whereas the exact value (5.4) for HIT should be replaced by the analogous expression (12.6). Instead, to generalise the scope of the Sc_T closures of the code, Sc_T -TLS (5.8) is here numerically tested under grid turbulence and proves to be an accurate closure without appreciable errors (Sec.7).

5.2. Sc_T -StHIT turbulence closure

The Sc_T -TLS closure (Sec.5.1) is limitedly but systematically over-diffusive in the ballistic regime ($t_{FLY} \ll T_L$) under shear flows (Sec.8). Thus, an alternative closure is presented as Sc_T -StHIT: it is constrained to Taylor's theory under Stationary HIT, as Sc_T -TLS, but it is half diffusive in the ballistic regime and progressively recovers the exact value of K_T under the HIT turbulent-diffusion regime. The Sc_T -StHIT closure is arbitrarily designed as if the modelled plume spread were equal to:

$$\sigma_{x^+}^2 = 2 \left(K_T \Big|_{x^+} + D_M \right) \bar{t}_{FP}, \quad \frac{d\sigma_{x^+}^2}{dt_{FLY}} = 2 \left[\left(K_T \Big|_{x^+} + D_M \right) + t_{FLY} \frac{dK_T \Big|_{x^+}}{dt_{FLY}} \right] \quad (5.10)$$

which represents the actual expression of the modelled plume spread only in the turbulent-diffusion regime. The replacement of the flight time t_{FLY} with the weighted ensemble mean of the pollutant flight time \bar{t}_{FP} (s) is defined and motivated in Sec.5.6. Imposing the fictitious plume spread (5.10) to be equal to the exact value (5.4) under HIT determines the following expression:

$$K_T = \frac{\sigma_{x^+,T}^2}{2\bar{t}_{FP}} = \frac{8}{9} \frac{\nu_T}{C_\mu \tilde{C}_0} \left[1 - \frac{T_L}{\bar{t}_{FP}} \left(1 - e^{-\frac{\bar{t}_{FP}}{T_L}} \right) \right] \quad (5.11)$$

Its limit behaviours are expressed as follows:

$$\lim_{\bar{t}_{FP} \ll T_L} K_T = \frac{\bar{q}\bar{t}_{FP}}{3}, \quad \lim_{\bar{t}_{FP} \gg T_L} K_T = \frac{2}{3} \bar{q} T_L = \frac{8}{9} \frac{\nu_T}{C_\mu \tilde{C}_0} \quad (5.12)$$

The resulting Sc_T -StHIT closure to RANS Cm-BE on the turbulent Schmidt number reads:

$$Sc_{T,k+1} = \frac{\frac{9}{8}C_\mu\tilde{C}_{0,k+1}}{\left[1 - \frac{T_L}{\bar{t}_{FP}} \left(1 - e^{-\frac{\bar{t}_{FP}}{T_L}} \right)\right]_{k+1}} \quad (5.13)$$

whereas its limit behaviours assume the following forms:

$$\begin{aligned} \lim_{\bar{t}_{FP} \rightarrow 0} Sc_T &= \infty, \quad \lim_{\bar{t}_{FP} \ll T_L} Sc_T = \frac{3\nu_T}{\bar{q}\bar{t}_{FP}} = 3C_\mu \frac{T_E}{\bar{t}_{FP}} = \frac{9}{4} C_\mu \tilde{C}_0 \frac{T_L}{\bar{t}_{FP}}, \\ \lim_{\bar{t}_{FP} \gg T_L} Sc_T &= \frac{9}{8} C_\mu \tilde{C}_0 \equiv Sc_{T,\min} \in \left[0; \frac{9}{8} C_\mu C_0 = 0.658\right] \end{aligned} \quad (5.14)$$

5.3. SCT -TGS turbulence closure

The SCT -TLS closure is analytically constrained to Taylors' theory (1922, [24]) under HIT (Sec.5.1) and is numerically found to be accurate under grid turbulence (Sec.7); at the same time, SCT -StHIT closure (Sec.5.2) provides a superior performance under shear flows (Sec.8). Thus, a generalised closure, which gradually shifts from SCT -TLS, where the roto-deformation frequency of the mean flow is small enough with respect to the turbulence frequency, to the SCT -StHIT closure, under opposite conditions, is derived. This generalised closure is referred to as SCT -TGS for sake of simplicity, being constrained to 'Taylor's theory', 'Grid turbulence' and the experimental 'Shear flow' of Fackrell & Robins (1982, [9]), which is representative of a general turbulent shear flow.

In the NSBL and NOBL subdomains of an analytical shear flow (e.g. Amicarelli, 2024, [25]), the product of the mean-velocity gradient times the Eulerian integral time scale of turbulence is approximately uniform:

$$\left(\frac{d\bar{u}}{dz} T_E \right)_{NOBL} \approx \left(\frac{d\bar{u}}{dz} T_E \right)_{NSBL} = \frac{1}{\sqrt{C_\mu}} = \frac{10}{3} \quad (5.15)$$

In an analytical shear flow, the quadratic invariants of the mean strain rate tensor S_m and the mean rotation tensor R_m read:

$$R_m = -S_m = \left(\frac{1}{2} \frac{d\bar{u}}{dz} \right)^2 \Rightarrow \left| \frac{d\bar{u}}{dz} \right| = 2\sqrt[4]{R_m(-S_m)} \quad (5.16)$$

The combination of (5.15)-(5.16) permits to define a non-dimensional frequency number N_f :

$$N_f \equiv 2T_E \sqrt[4]{R_m(-S_m)} \quad (5.17)$$

which is the ratio between the mean roto-deformation frequency and the turbulence frequency of the fluid flow. Where the first/latter is much larger than the latter/first, N_f tends to infinite/null values. An analytical shear flow is represented by the first limit, whereas HIT and grid turbulence lie in the second limit. A more useful range is given by the introduction of the exponential function e^{-N_f} because it varies between zero and the unity and equals 0.036 everywhere in an analytical shear flow, according to (5.15). In terms of K_T , SCT -TGS closure gradually shifts between SCT -TLS and SCT -StHIT closures depending on the frequency number N_f , as follows:

$$K_{T,TGS} = K_{T,TLS} e^{-N_f} + K_{T,StHIT} \left(1 - e^{-N_f} \right) = K_{T,StHIT} + (K_{T,TLS} - K_{T,StHIT}) e^{-N_f} \quad (5.18)$$

After some algebraic rearrangements, one obtains the following expression for K_T :

$$K_T = \frac{8}{9} \frac{\nu_T}{C_\mu \tilde{C}_0} \left[1 - \frac{T_L}{\tilde{t}_{FP}} \left(1 - e^{-\frac{\tilde{t}_{FP}}{T_L}} \right) \left(1 - e^{-2T_E \sqrt[4]{R_m(-S_m)}} \right) - e^{-\frac{\tilde{t}_{FP}}{T_L}} e^{-2T_E \sqrt[4]{R_m(-S_m)}} \right] \quad (5.19)$$

Its limit behaviours are expressed as follows:

$$\lim_{t_{FLY} \ll T_L} K_T = \frac{\tilde{q} t_{FLY}}{3} \left[1 + e^{-2T_E \sqrt[4]{R_m(-S_m)}} \right], \quad \lim_{t_{FLY} \gg T_L} K_T = \frac{2}{3} \tilde{q} T_L = \frac{8}{9} \frac{\nu_T}{C_\mu \tilde{C}_0} \quad (5.20)$$

The resulting SCT -TGS closure to RANS Cm-BE on the turbulent Schmidt number reads:

$$Sc_{T,k+1} = \frac{\frac{9}{8} C_\mu \tilde{C}_{0,k+1}}{\left[1 - \frac{T_L}{\tilde{t}_{FP}} \left(1 - e^{-\frac{\tilde{t}_{FP}}{T_L}} \right) \left(1 - e^{-2T_E \sqrt[4]{R_m(-S_m)}} \right) - e^{-\frac{\tilde{t}_{FP}}{T_L}} e^{-2T_E \sqrt[4]{R_m(-S_m)}} \right]_{k+1}} \quad (5.21)$$

which uses local values of the turbulence quantities. Its limit behaviours assume the following forms:

$$\lim_{t_{FLY} \rightarrow 0} Sc_T = \infty, \quad \lim_{t_{FLY} \ll T_L} Sc_T = \frac{9}{4 \left[1 + e^{-2T_E \sqrt[4]{R_m(-S_m)}} \right]} C_\mu \tilde{C}_0 \frac{T_L}{t_{FLY}}, \quad (5.22)$$

$$\lim_{\bar{t}_{FP} \gg T_L} Sc_T = \frac{9}{8} C_\mu \tilde{C}_0 \equiv Sc_{T,\min} \in \left[0; \frac{9}{8} C_\mu C_0 = 0.658 \right]$$

5.4. Sc_T turbulence closures: further motivations and numerical features

Anand & Pope (1985, [6]) stated that ‘turbulent diffusion models can be made to work, by making K_T an explicit function of σ_z or time (e.g. Deardorff, 1978, [14]; Libby & Scragg, 1973, [13])’ but that ‘such ad hoc modifications are inconsistent with the principles of invariant modelling and have little general utility’. They also stated that ‘second-order closures experience the same problem (e.g. Deardorff, 1978, [14]; Sykes et al., 1984, [15])’ because they need to make a transport coefficient depend on the scalar field. The above-mentioned inconsistency is explicitly reported in Pope (2011, [57]) as follows: ‘since the velocity field is (by definition) unaffected by passive scalars, in a consistent model, K_T is independent of any passive scalar field that may be present’.

On the inconsistency of any closure to RANS Cm-BE of a turbulent-diffusion model, four attempts of observation are reported in the following, considering Sc_T -TGS closure. First, the turbulent transport term of RANS Cm-BE depends on the concentration field and so it does the corresponding BE associated with any RANS PDF model. The inconsistency issue originates from the nature of the turbulent-diffusion models (i.e., deterministic RANS) where the turbulent coefficient is defined to properly work only in the turbulent-diffusion regime and thus to be independent on the mean-scalar field. It might be sufficient to define the turbulent dispersion coefficient to be dependent on the scalar field or on the flight time (as for the ‘time-dependent diffusivity’ of Pope, 2011, [57]) and not to use the expression turbulent-diffusion models to avoid such inconsistency. Secondly, if any Sc_T closure is inconsistent, than the state-of-the-art Sc_T -const approach risks to appear more inconsistent, after the clarified dependence of T_L on Re_T via the peak value of the compensated velocity Lagrangian structure function \tilde{C}_0 (Sec.5.5). This equals Kolmogorov constant C_0 only for ($Re_T \rightarrow \infty$): out of this extreme condition, any Sc_T -const approach does not satisfy any configuration, not even the simplest turbulent-diffusion regime under HIT. In this regime, the three Sc_T closures of the current study are equivalent and correctly depend on Re_T , which is a quantity exclusively associated with the transporting fluid, whereas any constant Sc_T value is independent on the local properties of the same fluid. Sc_T closures have to adapt their formulation out of the turbulent-diffusion regime because using $Sc_{T,\min}$ all over the domain would provide a consistent turbulent-diffusion model, but it would also lead to a sound failure everywhere in the domain, due to time-cumulated overestimation errors of the plume spread at small \bar{t}_{FP} . Under HIT, one would obtain:

$$\sigma_{\underline{x}^+, T}^2 \Big|_{Sc_T = Sc_{T,\min}} = \frac{2}{3} q T_L \bar{t}_{FP} \gg \sigma_{\underline{x}^+, T}^2 = \frac{2}{3} q (\bar{t}_{FP})^2, \quad \bar{t}_{FP} \ll T_L \quad (5.23)$$

Under general conditions, the use of any constant value for $Sc_T > Sc_{T,\min}$ determines a systematic over/underestimation of K_T at small/large \bar{t}_{FP} , although it is the state-of-the-art approach used by deterministic RANS CFD codes (Sec.1). It is equivalent to tune Sc_T so that an intermediate and constant value is approximately used all over the domain, and hopefully for any test case. Sc_T closures also avoid the inconsistent use of a large range of Sc_T constant values depending on the numerical method (or the code) and the application field (or the test case), unless specific tasks require explicit data assimilation or calibration. Nonetheless, there is no doubt about the superior accuracy of RANS PDF with respect to deterministic RANS, either with or without Sc_T closures. Thirdly, unlike the turbulent-diffusion models mentioned by Anand & Pope (1985, [6]), the Sc_T closures of the current code do not depend on the mean-scalar field, but on the quantities of the transporting flow and \bar{t}_{FP} , which is here unaffected by the scalar properties, except for the PS position. A possible fourth observation is that if an inconsistent correction to a consistent model makes this work more properly on a set of application fields, such correction might be considered useful in a specific scope.

On the little general utility of any closure to RANS Cm-BE of a turbulent-diffusion model, other four observations might be useful. First, the Sc_T -TGS closure is constrained to Taylor’s theory (HIT), grid

turbulence and an experimental shear flow. These three general test cases are considered sufficient to constrain the constants of most of the turbulence closures to RANS-ME (e.g., k-eps model) to make them apply under general conditions. Secondly, if SCT -TGS will fail under some application fields, these might be excluded from its scope, as for any turbulence scheme. Thirdly, SCT -TGS closure provides a positive test in assessing the mean concentration around a bluff body (Sec.9). A fourth possible observation is that, in the worst-case scenario where SCT -TGS will fail in any other application except for the ones mentioned above, then at least any RANS deterministic model could exploit SCT -TGS to properly treat these four general configurations without those systematic errors which currently affect the state-of-the-art SCT -const approach.

Under very large flight times, all the SCT closures of the code tend to SCT_{min} that only depends on Re_T . Chemical reactions and molecular diffusion are non-influential, being SCT only related to turbulent transport. Further, the SCT closures does not depend on the size of the Pollutant Source PS.

5.5. Peak value of the compensated velocity Lagrangian structure function

The velocity Lagrangian structure function is the tensor of the ensemble variance of the velocity time-difference along the fluid-particle trajectories (e.g. Sawford & Pinton, 2013, [17]). The peak value of its compensated (i.e. non-dimensional) norm (Sawford, 1991, [58]; Pope, 1994, [59]) was given a closed-form solution by Sawford et al. (2008, [16]):

$$\tilde{C}_0 = \frac{C_0}{1 + \frac{70}{\sqrt{15} Re_T}}, \quad Re_T = \frac{(\sigma_u)^4}{\varepsilon \nu} = \frac{4 \bar{q}^2}{9 \varepsilon \nu} = \frac{4}{9 C_\mu} \frac{\nu_T}{\nu} \approx 5 \frac{\nu_T}{\nu}, \quad \bar{q} = \frac{3}{2} \sigma_u^2 \quad (5.24)$$

This depends on Kolmogorov constant $C_0=6.5$ and the turbulence Reynolds number Re_T , which assumes a simplified HIT form. Eq.(5.24) is coded to assess T_L .

5.6. Weighted ensemble mean of the pollutant flight time for deterministic RANS models

The weighted ensemble mean of the pollutant flight time \bar{t}_{FP} (s) for the SCT closures is formulated hereafter. In the present section, any quantity is implicitly considered net of molecular diffusion. Under general conditions, the instantaneous flight time t_{FLY} from Taylor's theory (Taylor, 1922, [24]; Sec.5.1) requires a generalisation as it is not representative any longer of the age of the pollutant and the association between σ_x^2 and the plume spread (Sec.5.1) would be inaccurate.

The instantaneous pollutant time t_{FP} (s) is first introduced as the average flight time weighted over each fraction of pollutant mass within the fluid particle, at fixed time and space, in a specific virtual realisation of the turbulent flow. This quantity can correctly replace t_{FLY} in Taylor's theory (Taylor, 1922, [24]). Instead, a proper ensemble statistic is requested under deterministic RANS modelling.

The ensemble mean \bar{t}_{FP} does not fully represent the pollutant mass associated with \bar{C} because the contributions from each realisation are not weighted over C . This motivates the introduction of the

weighted ensemble mean of the pollutant flight time $\bar{t}_{FP} \equiv \bar{t}_{FP} \equiv \bar{t}_{FP} \equiv \bar{t}_{FP}$ (s), whose curved over-bar denotes an ensemble mean weighted on the instantaneous pollutant mass per unit of volume (i.e. C):

$$\bar{t}_{FP} \equiv \frac{\sum_{i=1}^{N_r} t_{FP,i} C_i}{\sum_{i=1}^{N_r} C_i} = \frac{\sum_{i=1}^{N_r} t_{FP,i} C_i}{N_r} \frac{N_r}{\sum_{i=1}^{N_r} C_i} = \frac{\overline{t_{FP} C}}{\bar{C}} \quad (5.25)$$

where N_r is the number of virtual realisations of the same turbulent flow. The quantity \bar{t}_{FP} seems an accurate generalisation for t_{FLY} , but (5.25) is associated with two additional BEs for $\overline{t_{FP} C}$ and \bar{C} . The latter might be reasonably approximated by Cm-BE, which includes molecular diffusion. Even though the resulting error grows when Re decreases, the role of SCT simultaneously diminishes. On

the other hand, a new stable scheme for the BE of $\overline{t_{FP}C}$ requires appreciable computational time. Such complication is out of the scope of the current study and would need proper motivation. Instead, a simplified model is adopted, keeping the definition of \check{t}_{FP} , but avoiding the numerical solution of a new PDE. It is assumed that any pollutant turbulent flux of any node with its surrounding environment does not alter the particle \check{t}_{FP} . Under this simplifying hypothesis, \check{t}_{FP} always has the same rate of change of t . The simple associated PDE has the following closed-form solution:

$$\frac{d\check{t}_{FP}}{dt}\Bigg|_{\underline{u}_0} = 1 \Rightarrow \check{t}_{FP,0,k+1} = t_{k+1} - t_{ENT,0} + \check{t}_{FP,ENT,0} = t_{FLY,0,k+1} + \check{t}_{FP,ENT,0} \quad (5.26)$$

where the Initial Condition $\check{t}_{FP,ENT}$ (s) at the particle entry time t_{ENT} (s) is assigned in the following. Under single PS and null background inlet concentration \overline{C}_{inlet} , the following expression applies:

$$\check{t}_{FP,ENT,0} = \begin{cases} \left[\check{t}_{FP,PS} - (t_{FLY,FRO,max,PS} + \Delta t_{SPPS,PS}) \right] \frac{\left(-n_{inlet} \cdot \overline{u} \Big|_{x_{PS}} \right)}{\left(-n_{inlet} \cdot \underline{u}_0 \right)}, & \text{inlet} \\ 0, & \text{other BCs / ICs} \end{cases} \quad (5.27)$$

where the first line sets all the SPH inlet particles and the latter is related to the background concentrations for the other subdomains under different BC/IC conditions. $\check{t}_{FP,PS}$ (s) is the physical input value for \check{t}_{FP} at the downstream edge of any polluted IC/BC/PS volume: the IC variable $\check{t}_{FP,ENT}$ is inhomogeneous to reproduce ($\check{t}_{FP} \approx \check{t}_{FP,PS}$) when any inlet particle passes the cross-stream section containing the above-mentioned edge. The time lag Δt_{SPPS} is defined in Sec.6.

In the absence of PSs, all the inlet particles are treated with the other BC/IC zones by the second line of (5.27). Its default null value is motivated as follows. The dispersion along the cross-stream directions at the edges of any IC/BC zone is the main concern in terms of plume-spread evolution. Here any plume edge propagates as a point PS as long as \overline{C} is uniform within the IC/BC zone.

Under multiple PSs or ($\overline{C}_{inlet} > 0$), several procedures apply. PS inlet particles are associated with a sole PS and (5.27) is approximately adopted. For inlet particles not passing for any PS, a weighted average is performed involving the null $\check{t}_{FP,ENT}$ value representative of \overline{C}_{inlet} (with weight equal to 1 or 0 for positive or null \overline{C}_{inlet}) and an overall value associated with the set of PSs (with weight equal to the number of PSs). This set value is computed following the first line of (5.27), but introducing a PS-average for each of the following quantities: ($t_{FLY,FRO,max,PS} + \Delta t_{SPPS,PS}$); $\check{t}_{FP,PS}$; $\overline{u}_{PS,inlet}$.

The default null value in (5.27) for the background concentrations in the initial fluid bodies and at the inlet section can be changed in input to possibly improve multiple-PS emission scenarios.

The errors of the current model grows with the distance between the inlet section and the PS section. Such errors also depend on the cross-stream inhomogeneity of the mean velocity. In the presence of an elevated PS, they might contribute to systematically enhance dispersion towards the bottom-wall regions, where mean velocity decreases, with overestimation of \check{t}_{FP} and underestimation of SCT .

Regarding possible uses in Eulerian CFD codes, the PDE associated with (5.26) would read:

$$\frac{\partial \check{t}_{FP}}{\partial t} = -\overline{u}_j \frac{\partial \check{t}_{FP}}{\partial x_j} + 1 \quad (5.28)$$

where the advection term, implicitly represented by the current Lagrangian code, has to be discretised by a mesh-based method. An alternative formulation for \check{t}_{FP} , conceived for experimental procedures, is reported in Hanna & Britter (2002, [60]) and Bezpalcova (2007, [61]) in terms of ‘travelling time’, as function of the ‘effective transport speed’ (or ‘cloud advection speed’).

6. SUB-PARTICLE POLLUTANT-SOURCE (SPPS) SCHEME

The size of the numerical Pollutant Source PS can be conveniently set larger than the physical PS, but this difference causes a spurious numerical diffusion at PS. To minimise such diffusion, the following Sub-Particle Pollutant-Source (SPPS) spatial reconstruction scheme is introduced. It manages the very early stage of the plume development within the particles which discretise the PS. Based on experimental evidence, the intrusion model reported in Cushman-Roisin (2019, [62]) for a turbulent jet in a still environment expresses the radius of the ‘jet-environment’ intrusion region R_x (m) as function of the stream-wise distance from the emission section of the jet (i.e. the PS section):

$$R_x = \frac{(x - x_{PS})}{5} + R_{PS}; \quad R_x \equiv 2\sigma_z = 2\sigma_y; \quad R_{PS} = \begin{cases} \sqrt{\frac{A_{PS}}{\pi}}, & 3D \\ \frac{A_{PS}}{2W_{PS}}, & W_{PS} \equiv 1, \quad 2D \end{cases} \quad (6.1)$$

where molecular diffusion is neglected. The x -axis is here aligned with the average mean velocity at the PS. R_x is measured as the mean-plume radius, being the jet polluted by a passive scalar. R_{PS} (m) is the radius of the isotropic equivalent physical PS; it is the radius of the circle in 3D (or the half-length of the segment in 2D) which has the same area A_{PS} (m^2) as the physical PS. Eq.(6.1) is also valid for any velocity deviation of the jet with respect to a uniform, non-null environment mean velocity U_{env} (m/s), being U_{emi} (m/s) the average mean velocity at the exit of the emission duct ($x=x_{PS}$). The numerical ‘ $_{num}$ ’ PS discretises the physical PS using n_{pPS} numerical points (Sec.4.3). The area and radius of the numerical PS are expressed as follows:

$$A_{PS,num} = \begin{cases} \pi R_{PS,num}^2 = (\Delta x)^2 n_{pPS}, & 3D \\ 2R_{PS,num} W_{PS} = n_{pPS} (\Delta x) W_{PS}, & 2D \end{cases} \Rightarrow R_{PS,num} = c_{SPPS} (\Delta x); \quad c_{SPPS} \equiv \begin{cases} \sqrt{\frac{n_{pPS}}{\pi}}, & 3D \\ \frac{n_{pPS}}{2}, & 2D \end{cases} \quad (6.2)$$

In terms of equivalent radius, the numerical PS of (6.2) matches the downstream evolution of the isotropic equivalent physical PS of (6.1) at a specific position noticed as x_{SPPS} (m):

$$R_{x_{SPPS}} = R_{PS,num} \Rightarrow (x_{SPPS} - x_{PS}) = \max \{5(c_{SPPS} \Delta x - R_{PS}); 0\} \quad (6.3)$$

where a null limiter is integrated to avoid upstream unphysical dispersion. The SPPS scheme applies to the SPPS region, which is the space contained by the extrusion of the numerical PS downstream the position of the physical PS to x_{SPPS} . In this region, all the pollutant fluxes of a PS particle are zeroed, including the opposite fluxes of the neighbouring particles. For each PS, a uniform SPPS frozen time lag Δt_{SPPS} (s) is assessed as follows:

$$\Delta t_{SPPS} \equiv t_{FLY,SPPS} - t_{FLY,PS} \approx \frac{(x_{SPPS} - x_{PS})}{|\bar{u}|_{x_{PS}}} \quad (6.4)$$

The SPPS scheme freezes the mean plume downstream the PS up to a maximum length of few SPH particle sizes. The SPPS scheme is thus interpreted as a spatial reconstruction scheme. It is consistent, being non-influential for $\Delta x \rightarrow 0$. The SPPS scheme effectively inhibits numerical diffusion at PS also because no spatial filter applies. The residual part of the \bar{C} numerical diffusion decreases with the flight time from the PS to the SPPS downstream edge. Here the residual errors are mainly related to representing a uniform \bar{C} field within a PS particle. Compared to the ballistic regime of Taylor’s theory (Taylor, 1922, [24]) in (5.3), the jet-intrusion model has the advantage of being valid for any velocity deviation of the jet, but it is more approximated under null U_{emi} , which features the ballistic regime. The two approaches are equivalent if the following conditions are all satisfied: U_{env} and U_{emi}

are uniform; $R_{PS} \ll \Delta x$; $\sigma_w = \frac{|u|}{10}$, being σ_w (m/s) the standard deviation of the vertical velocity.

7. GRID TURBULENCE WITH SURFACE POLLUTANT SOURCE

The new features of the code of Sec.2 are validated under grid turbulence. The air-flow pasts a mechanical grid virtually located at the inlet section, whose lowest half is featured by a surface Pollutant Source PS of NO. Top unpolluted air and bottom contaminated air mix within the channel featured by decaying turbulence to provide the mean concentration field of Figure 1 (top panel). This is more diffused than the corresponding field in Amicarelli (2024, [25]), where the previous code version was tested and full description of the test case is available. This benchmark is associated with a full-scale application to Duct Air Quality (Figure 1, bottom panel). The reference simulation adopts the Sc_T -TGS closure. The SPPS scheme is non-influential. Validation is executed by comparison with the closed-form solution of Anand & Pope (1985, [6]), as generalised in Sec.12.3 to be coherent with Bos (2020, [63]): it is referred to as Anand & Pope (1985, [6], gen.), for sake of brevity.

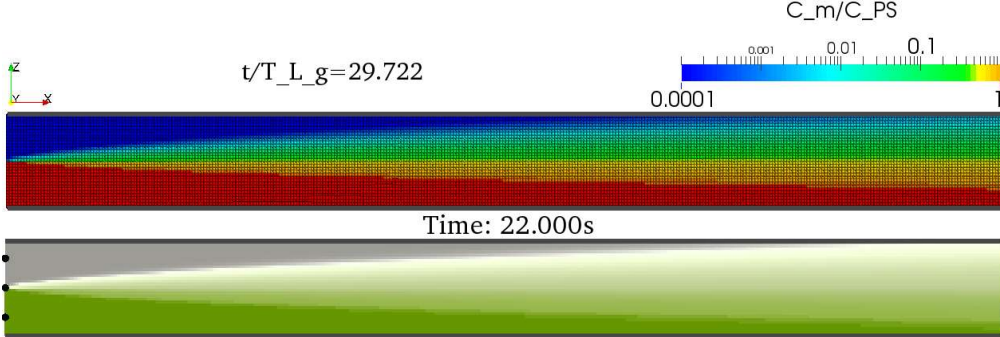


Figure 1. Grid turbulence with surface Pollutant Source: \bar{C} field. Top panel: non-dimensional field. Bottom panel: duct (grey and black) air-flow past a mechanical grid (black); \bar{C} goes from transparent white to saturated dark green (PS). CFD-OUT-sweePDF v.2.0.0 (Sc_T -TGS closure).

The main synthetic validation concerns the stream-wise profile of the non-dimensional \bar{C} at a specific intermediate height ($z=0.4375H_{dom}$) where both stream-wise and cross-stream gradients are relevant. The replacement of Sc_T -const approach with Sc_T -TGS closure practically zeros the errors (Figure 2, left panel). They were associated with a slight over-diffusion near the PS and a relevant under-diffusion more downstream. A residual error of ca.1% regards the reproduction of the BC at the inlet section, due to the truncation errors of the SPH-TSE filter (the nearest-particle method of Sec.3.8 is not used to extract these stream-wise profiles for sake of simplicity).

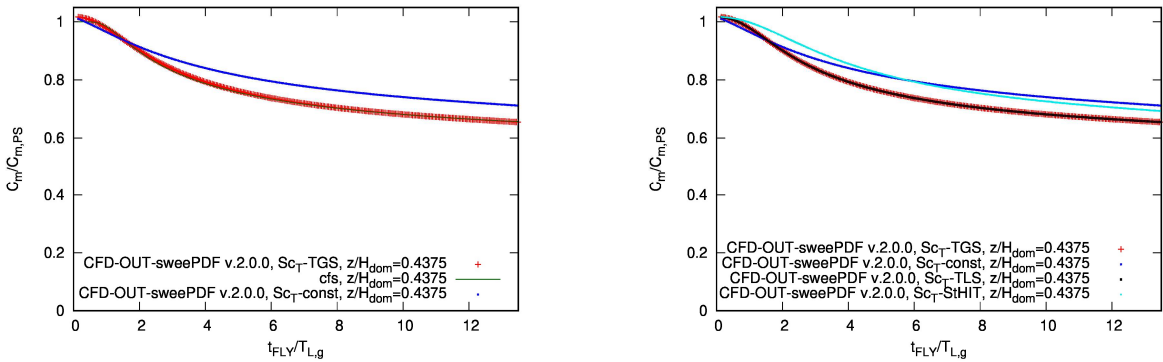


Figure 2. Grid turbulence at $t=t_f$ being t_f (s) the time at stationary conditions. Stream-wise profiles of the non-dimensional \bar{C} at $z/H_{dom}=0.4375$. Validation (left panel). Inter-comparisons on Sc_T assessments (right panel). Legend: CFD-OUT-sweePDF v.2.0.0 (reference simulation with Sc_T -TGS: +); closed-form solution (Anand & Pope, 1985, [6], gen.: —); CFD-OUT-sweePDF v.2.0.0 variants (Sc_T -const: *; Sc_T -TLS: ■; Sc_T -StHIT: □).

The ratio $t_{FLY}/T_{L,g}=1.70$ corresponds to $t_{FLY}/T_L=1.00$; the maximum ratio t_{FLY}/T_L being equal to 1.93. The sparring Sc_T -TLS closure practically provides the same results as Sc_T -TGS (Figure 2, right panel), whereas the other alternative Sc_T -StHIT is systematic under-diffusive, especially at the intermediate

distances within the domain. Thus, its overall performance is slightly worse than $Sc_T\text{-const}$, unless the numerical domain extended beyond the current outlet section.

Further validations refer to the five cross-stream profiles of Figure 3. All of them confirm that the residual errors resulting from the application of $Sc_T\text{-TGS}$ closure are negligible, fixing the slight over-diffusion near the inlet section and the relevant under-diffusion far enough from the PS. The output values along the most upstream profile (Figure 3, top-left panel) describe an almost discontinuous field of \bar{C} requiring the nearest-particle unfiltered ensemble values along these monitors (Sec.3.8).

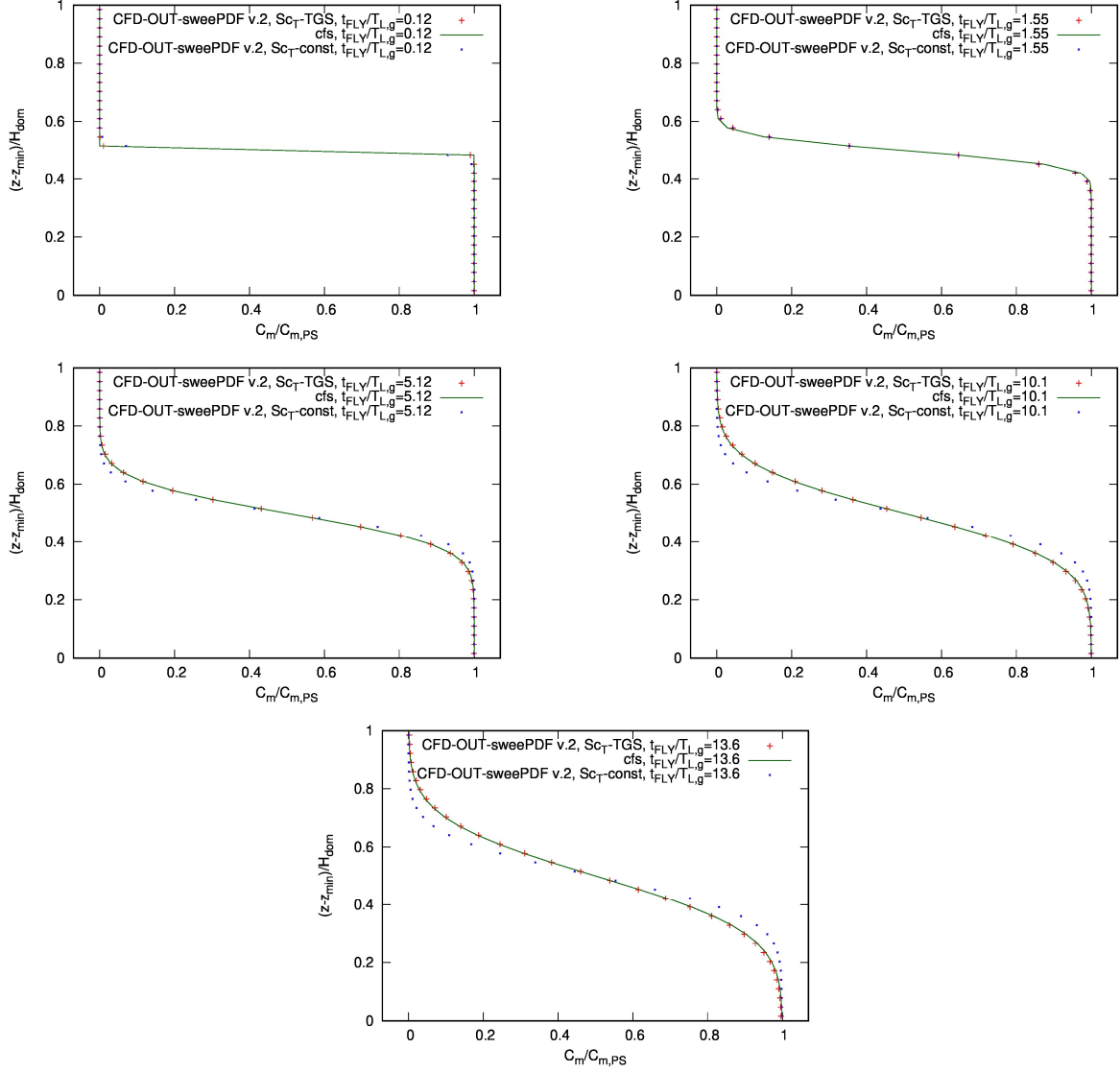


Figure 3. Grid turbulence: validations ($t=t_f$). Vertical profiles of relative \bar{C} (from top left to bottom right): $t_{FLY}/T_{L,g}=0.12, 1.55, 5.12, 10.1, 13.6$. Legend: CFD-OUT-sweePDF v.2.0.0 (reference simulation with $Sc_T\text{-TGS}$: +); closed-form solution (Anand & Pope, 1985, [6], gen.: —); CFD-OUT-sweePDF v.2.0.0 ($Sc_T\text{-const}$ approach: *).

The numerical results also concern other three sparring simulations, featured by the following differences with respect to the reference one (with $Sc_T\text{-TGS}$ closure): halved $F_{\mathcal{A}}$ (the time integration optimisation factor); doubled Δx ; doubled Δx with solid bodies as lateral boundaries in 3D. The results show spatial and time convergences, the correct behaviour of the solid bodies as boundaries and the consistency between the 2D and the 3D numerical models of the current code (Figure 4).

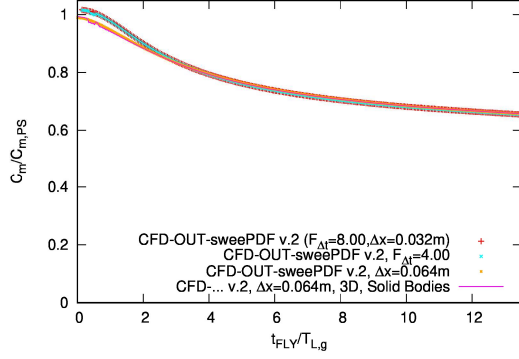


Figure 4. Grid turbulence: further inter-comparisons on \bar{C} . Time/space convergence; 3D validation with solid bodies.

Legend: CFD-OUT-sweePDF v.2.0.0 (ref. sim. with default $F_A=8.00$ and $\Delta x=0.032\text{m}$: $+$; variant with $F_A=4.00$: \times ; variant with $\Delta x=0.064\text{m}$: \diamond ; 3D variant with solid bodies, $\Delta x=0.064\text{m}$: —).

The computational cost of the reference simulation is quantified by the Total Virtual Memory $TVM=0.05\text{GB}$ and the elapsed time $t_{ela}=76\text{s}$ on 3.5 physical cores (with hyper-threading) of an i9-13900HX CPU processor. The very small number of cores is only due to a very-low-cost operative strategy.

8. EXPERIMENTAL TURBULENT SHEAR FLOW WITH ELEVATED POLLUTANT SOURCE

The novelties of Sec.2 are validated on the experimental turbulent shear flow of Fackrell & Robins (1982, [9]) with an Elevated Pollutant Source (EPS). Full description of the test case is available in Amicarelli (2024, [25]), where the previous code version was tested. This benchmark is associated with an application to Outdoor Air Quality with a stack ordinary emission of propane (C_3H_8) at the scale ratio of 1:1000. The SPH particle size is $\Delta x=0.03\text{ m}$. The reference simulation adopts the SCT -TGS closure and the SPPS scheme. The latter is deactivated in the simulations which exclusively focus on the differences between the SCT -related approaches, also comparing with the measurements of Fackrell & Robins (1982, [9]), and with the LSM-FDM numerical results of Amicarelli et al. (2011, [27]). For sake of simplicity, jet intrusion at PS is not explicitly modelled. The \bar{C} field around the most upstream monitoring point of the horizontal profile is almost discontinuous requiring the nearest-particle method (Sec.3.8).

Figure 5 indicates that the fields of the mean TKE and its dissipation rate are accurately reproduced so that the errors in the \bar{C} field should relate to SCT and possible truncation errors.

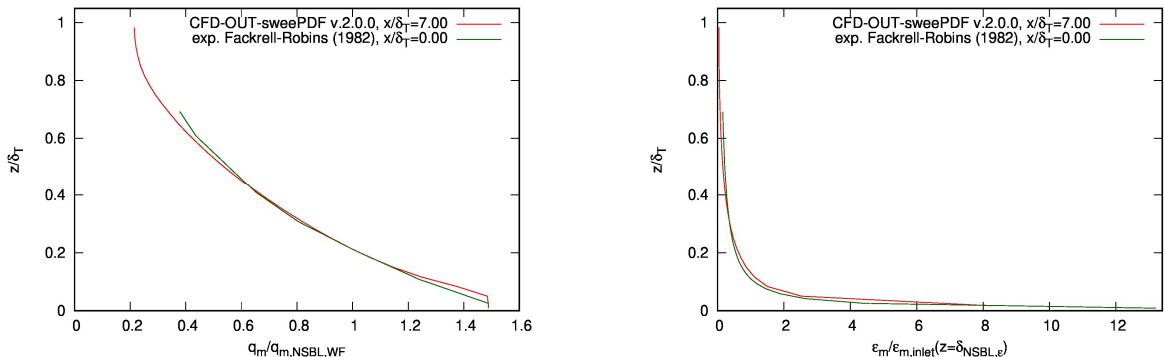


Figure 5. Shear flow with EPS: stream-wise profiles of the mean TKE and its dissipation rate near the outlet section ($\Delta x=0.03\text{m}$). Legend: CFD-OUT-sweePDF v.2.0.0 (—); experimental values (Fackrell & Robins, 1982, [9]): —).

Figure 6 (left panel) shows the \bar{C} horizontal profile of the maxima along the vertical and synthesises the overall validation of the SCT -TGS closure on the present benchmark. In this scope, the SCT -const

approach was found to systematically and progressively underestimate \bar{C} while approaching the PS (Amicarelli, 2024, [25]). The turbulence closure S_{CT} -TGS permits to fix this bias (Figure 6) because it indirectly represents velocity autocorrelation (Sec.5). The benefits provided by the S_{CT} -TGS closure are highlighted by comparison with the measurements of Fackrell & Robins (1982, [9]) showing larger improvements closer to the PS, up to one order of magnitude. The S_{CT} -TGS closure seems to fill the gap between the S_{CT} -const approach, belonging to deterministic RANS CFD, and the simulation of Amicarelli et al. (2011, [27]), related to stochastic RANS CFD, in simulating the dispersion of a passive pollutant in a turbulent shear flow. The largest errors of S_{CT} -const approach occur far from the bottom wall, thus excluding their association with Boundary Conditions. The sparring closure S_{CT} -StHIT is practically equivalent to the reference S_{CT} -TGS on the present test case, whereas S_{CT} -TLS is limitedly over-diffusive; the three closures provide better performances than S_{CT} -const (Figure 6, right panel).

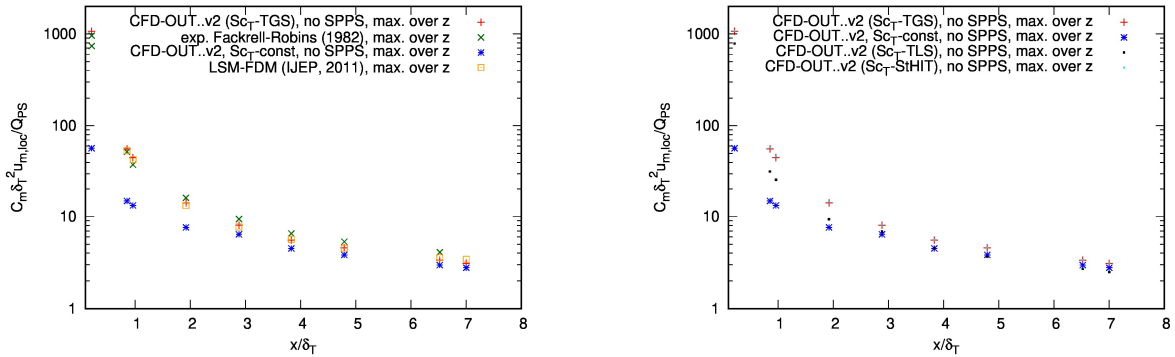


Figure 6. Shear flow with EPS: \bar{C} horizontal profile ($t=t_f$, $y=y_{PS}=0$). Validation (left panel) and S_{CT} -related inter-comparisons (right panel) on the maxima along the vertical: CFD-OUT-sweePDF v.2.0.0, S_{CT} -TGS, SPPS off (red +); experimental values (Fackrell & Robins, 1982, [9]: green x); CFD-OUT-sweePDF v.2.0.0 variants with SPPS off (S_{CT} -const: blue *; S_{CT} -TLS: black ■; S_{CT} -StHIT: blue ■); LSM-FDM numerical results of Amicarelli et al. (2011, [27]; orange □).

The benefits given by S_{CT} -TGS closure are confirmed by the cross-stream profiles of relative \bar{C} normalised over the local maximum along each profile (Figure 7). Despite some residual overestimations at ground, close enough to the PS, the overall improvements are systematic for the three most upstream profiles where the S_{CT} -TGS results are much closer to the available measurements (Fackrell & Robins, 1982, [9]) than using the S_{CT} -const approach.

The SPPS scheme is finally activated to configure the reference simulation of the code of Sec.2 for the current test case, keeping the S_{CT} -TGS closure active (Figure 8). The resulting stream-wise profiles of \bar{C} are point-to-point compared with the available measurements (Fackrell & Robins, 1982, [9]) also at the ground level (Figure 8, left panel). The numerical results correctly match the measured values with limited errors. They refer to an anticipated arrival of the mean plume at ground with a coherent anticipation of \bar{C} peak at the same height. The simulated \bar{C} is limitedly overestimated at $x < \delta_T$ and slightly underestimated at $x > \delta_T$. The incremental contribution of the SPPS scheme is secondary and slightly deteriorates the quantitative performance of the code (Figure 8, right panel). Beyond this minor drawback, possibly due to some counterbalancing effect with the SPH truncation errors, SPPS provides a more reliable physical description of the plume around the PS and is kept active in the following validations which motivate its use.

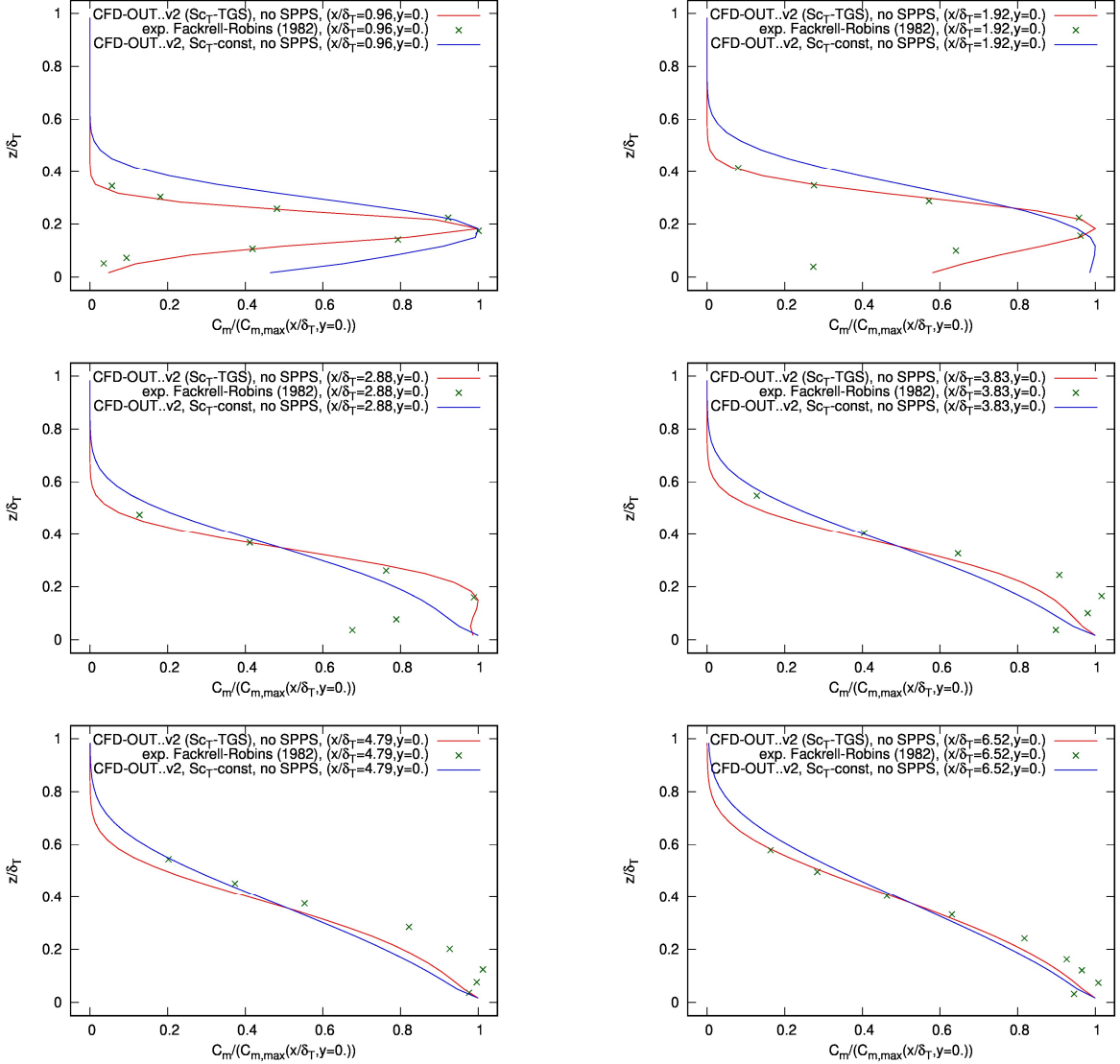


Figure 7. Shear flow with EPS: vertical profiles of relative dispersion ($t=t_f$, $y=y_{PS}$). From top-left to bottom-right panels: $x/\delta_T=0.96, 1.92, 2.88, 3.83, 4.79, 6.52$. CFD-OUT-sweePDF v.2.0.0, Sc_T -TGS, SPPS off (—); experimental values (Fackrell & Robins, 1982, [9]: \times); sparring simulation with Sc_T -const approach and SPPS off (—).

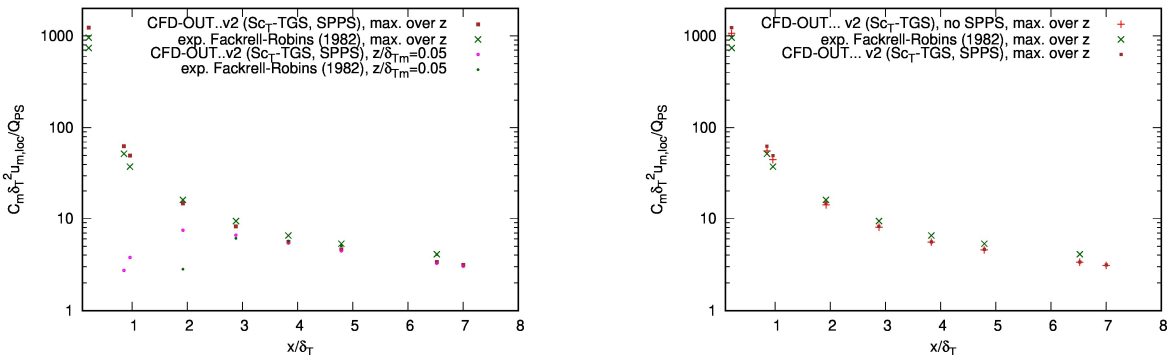


Figure 8. Shear flow with EPS: \bar{C} horizontal profiles ($t=t_f$, $y=y_{PS}$). Left panel: validation on the maxima along the vertical and on the ground-level values. Right panel: inter-comparisons on the maxima with/without SPPS. CFD-OUT-sweePDF v.2.0.0 (reference simulation, i.e. Sc_T -TGS and SPPS on: ■, ●); experimental values (Fackrell & Robins, 1982, [9]: \times , ●); CFD-OUT-sweePDF v.2.0.0 with Sc_T -TGS and SPPS off (+).

The benefits of the SCT -TGS closure vs. the SCT -const approach are also analysed in terms of \bar{C} field and plume shape. The comparison of the vertical section of \bar{C} field passing for the PS (Figure 9) shows that the upper and lower edges of the SCT -TGS plume depict a linear shape close enough to the PS, coherently with the ballistic regime of turbulent transport and contrarily to the parabolic shape that the SCT -const plume reproduces all over the domain. This is due to the absence of velocity autocorrelation. SCT -TGS relevantly reduces the turbulent dispersion assessed by SCT -const: the plume depth is smaller; its \bar{C} maxima along the vertical are larger. The SPPS scheme qualitatively adds a secondary improvement to the plume shape very close to the PS by freezing \bar{C} for a distance of $2.11\Delta x$ to permit the small physical plume to correctly reach the particle size. SPPS effect in the non-frozen region is a translation of \bar{C} field downstream.

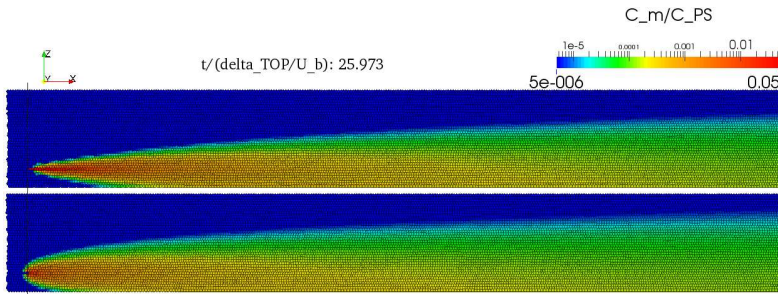


Figure 9. Shear flow with EPS. Vertical slice ($y=y_{PS}$) of the non-dimensional field for \bar{C} ($t=ca.t_f$). Top panel: SCT -TGS closure (and SPPS on). Bottom panel: SCT -const approach (and SPPS off). The vertical line represents the vertical section containing the PS.

Analogous improvements are found in the representation of the horizontal turbulent fluxes of the pollutant. The plume width is also correctly reproduced by SCT -TGS with a reduced dispersion close enough to the PS where the plume width shows a linear growth (Figure 10). Due to the optimised positions of the lateral boundaries, the over-diffusive reproduction of the plume width by SCT -const also triggers some side effects which might reach the monitors along the domain central section.

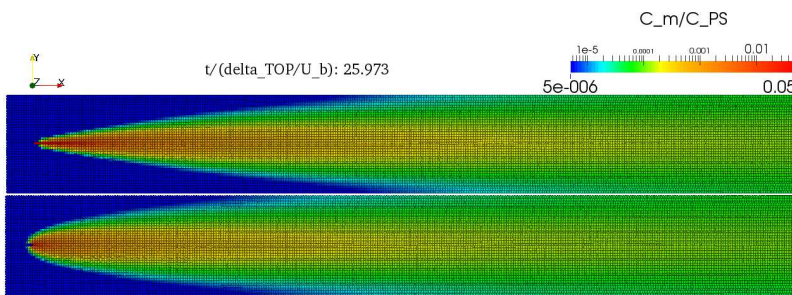


Figure 10. Shear flow with EPS: non-dimensional field for \bar{C} ($t=ca.t_f$). Horizontal slice ($z=z_{PS}$). Top panel: SCT -TGS closure (and SPPS on). Bottom panel: SCT -const approach (and SPPS off).

The iso-surfaces of the non-dimensional \bar{C} are obtained from the grid points (Figure 11) and represents a 3D layout of the \bar{C} field. The SCT -TGS iso-surfaces of the largest values involve bigger volumes and reaches longer stream-wise distances than SCT -const, due to the proper amount of turbulent dispersion. The iso-surface of the lowest value shows the correction to the plume shape.

SCT -TGS introduces the estimations of \bar{t}_{FP} and SCT . The central vertical slice of the field of the ratio \bar{t}_{FP}/T_L (Figure 12, top panel) represents the growth of the weighted ensemble mean of the pollutant flight time with the distance from the PS and its decrease with height due to larger values of the mean velocity, associated with smaller flight times. This dependence on z is amplified by T_L increase with height.

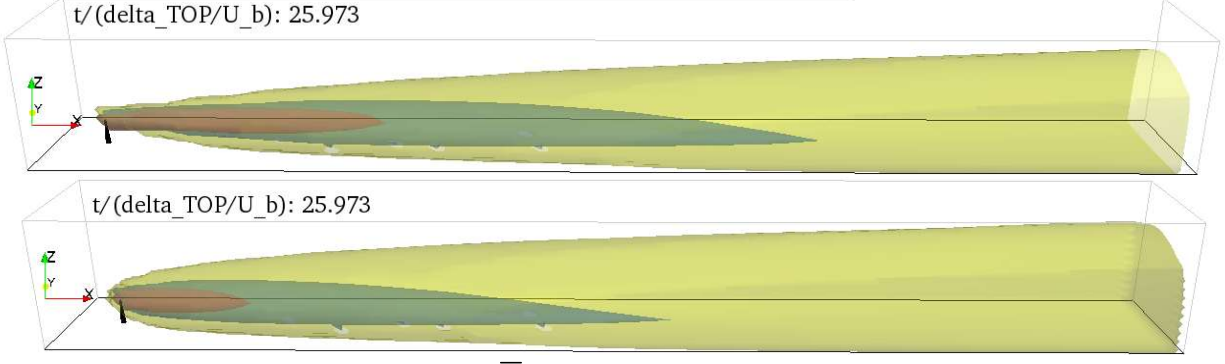


Figure 11. Shear flow with EPS: iso-surfaces of \bar{C} normalised by its maximum value at PS (red: 5×10^{-4} , cyan: 2×10^{-4} , yellow: 1×10^{-5}) at $t=ca.t_f$. Top panel: Sc_T -TGS closure (and SPPS on). Bottom panel: Sc_T -const approach (SPPS off).

Almost the whole domain is interested by a hybrid regime of pollutant transport, whereas the pure ballistic regime ($\tilde{t}_{FP}/T_L \leq 0.05$) can be detected close to the PS. The spatial pattern of \tilde{t}_{FP}/T_L rules the Sc_T field (Figure 12, bottom panel), whose vertical inhomogeneity is amplified by Re_T via \tilde{C}_0 (Sec.5.5). The value of $Sc_T=0.72$ (Sec.5), associated with Sc_T -const approach, represents an intermediate Sc_T value in the downstream half of the domain, where \bar{C} differences with respect to Sc_T -TGS are more limited. Sc_T ranges from ca.0.3 to over 100. Its assessment is suspended in the Cm-BE frozen region (Sec.4.3), which includes the SPPS region (Sec.8).

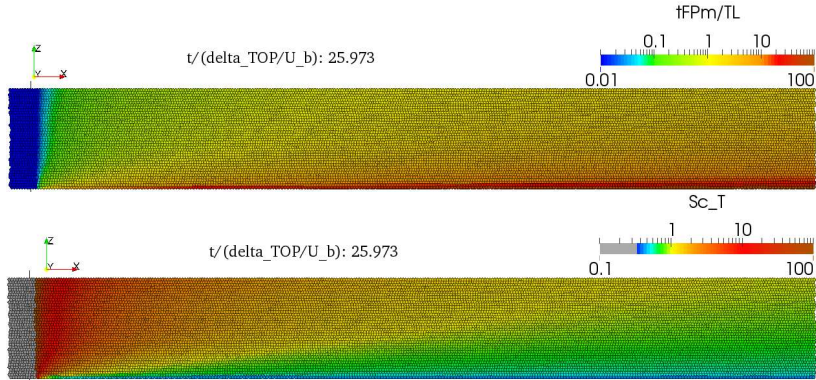


Figure 12. Shear flow with EPS: vertical slices ($y=y_{PS}$) of the fields of \tilde{t}_{FP}/T_L (top panel) and Sc_T (bottom panel) at $t=ca.t_f$. CFD-OUT-sweePDF v.2.0.0: reference simulation (Sc_T -TGS closure and SPPS on).

Thanks to the Sc_T -TGS closure, the residual errors of the reference simulation are limited; their possible sources are discussed in the following. The approximated model for \tilde{t}_{FP} (Sec.5.6) might enhance turbulent dispersion towards the wall where the mean velocity decreases and Sc_T is probably underestimated. In the wall SPH neighbourhood, along the mean plume centreline, the same bias might play a secondary beneficial role counterbalancing the under-diffusive effect induced by the C_0 -consistent BC terms in SPH Cm-BE. The SPH truncation error in reproducing a quasi-Laplacian might also play an appreciable role far from the wall if \bar{C} is strongly non-linear. The computational cost of the reference simulation is quantified by the Total Virtual Memory $TVM=5.77\text{GB}$ and the elapsed time $t_{ela}=\text{ca.}9\text{h}33\text{min}$ on 3.5 physical cores (with hyper-threading; i9-13900HX CPU). The present test case is associated with an application to Outdoor Air Quality with a stack ordinary emission of hydrocarbons (C_3H_8) over flat topography. At full scale, the improvements given by Sc_T -TGS (vs. Sc_T -const) and by the SPPS scheme (vs. an implicit numerical diffusion at source) are appreciated in the 3D representation with progressive colouring of Figure 13, where the most polluted region of the air-flow is highlighted. The concentration freezing is clearly visible just downstream the PS as well as the ballistic regime with linear growth of the plume spread in the early stages of the

pollutant transport. Under the reference simulation, the stream-wise length of the most polluted region is longer than the sparring simulation with Sc_T -const and the plume spread is smaller near the PS.

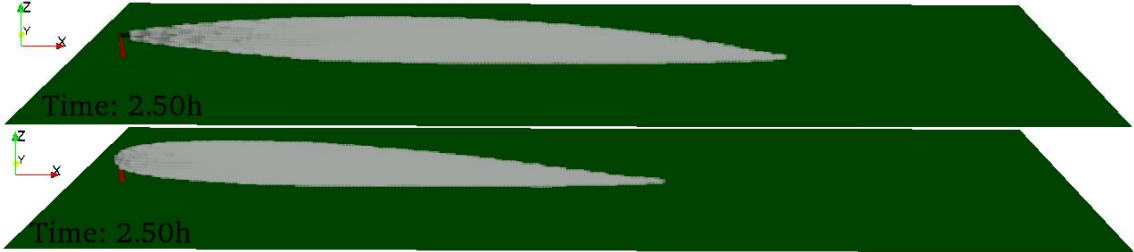


Figure 13. Shear flow with EPS: \bar{C} field ($t=t_f$). Stack ordinary emission of C_3H_8 (full-scale application) with \bar{C} going from transparent white (null values) to black saturated at PS (stack in red, grassy flat topography in green). Top panel: Sc_T -TGS closure (and SPPS on). Bottom panel: Sc_T -const approach (and SPPS off).

9. CONFINED FLOW PAST A WALL-MOUNTED CUBIC OBSTACLE WITH CANYON POLLUTANT SOURCE

The code of Sec.2 is validated on a confined flow past a wall-mounted cubic obstacle of size H_b (m) with a canyon Pollutant Source. It is the reproduction of the experimental air-flow of Martinuzzi & Tropea (1993, [64]) combined with the dispersion scenario whose BCs are set as close as possible to the experiment of Mavroidis et al. (2003, [65]). The full description of the test case is available in Amicarelli (2024, [25]), where the previous code version was tested. The non-dimensional concentration $\pi_{\bar{C}}$ is defined according to Mavroidis et al. (2003, [65]). The test case is associated with an application to Indoor Air Quality with an accidental release of hydrocarbons (C_3H_8) from a pipeline in a ventilated indoor parking lot with guard post (scale ratio 1:100). The reference simulation is compared with the results of the previous version of the code (Amicarelli, 2024, [25]), featured by the Sc_T -const approach and the absence of the SPPS scheme.

In the horizontal slice of the \bar{C} field passing for the obstacle barycentre (Figure 14), the Sc_T -TGS closure improves the plume representation upstream the obstacle. Here the plume is much narrower than using the Sc_T -const approach, evolves with a linear growth coherently with the near-source ballistic regime of turbulent transport and is more influenced by the displacement zone of the air-flow, induced by the presence of the obstacle. Downstream, in the monitoring region, the \bar{C} field does not show relevant differences among the two approaches. In the non-frozen zone of the reference simulation, the SPPS scheme simply translates the mean plume downstream of $2.40\Delta x$, which is the length of the SPPS region.

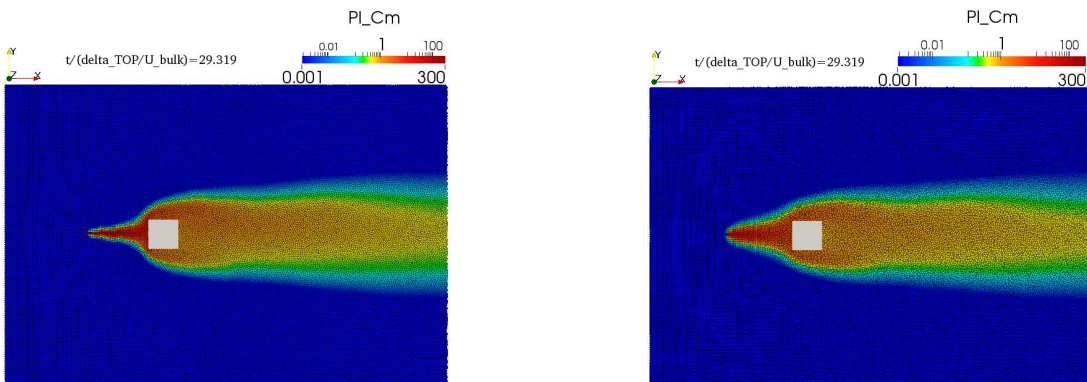


Figure 14. Confined flow past a cube with CPS at $t=ca.t_f$. Non-dimensional field of $\pi_{\bar{C}}$ (horizontal slices, $z=H_b/2$). Left panel: reference simulation (Sc_T -TGS; SPPS on). Right panel: simulation with Sc_T -const (Amicarelli, 2024, [25]).

Analogous Sc_T -TGS improvements are recorded over the vertical slice of Figure 15, where the further confinement exerted by the bottom wall is more influential with the Sc_T -const approach; this also shows some extra dispersion around the PS, where its underestimation of Sc_T is maximum.

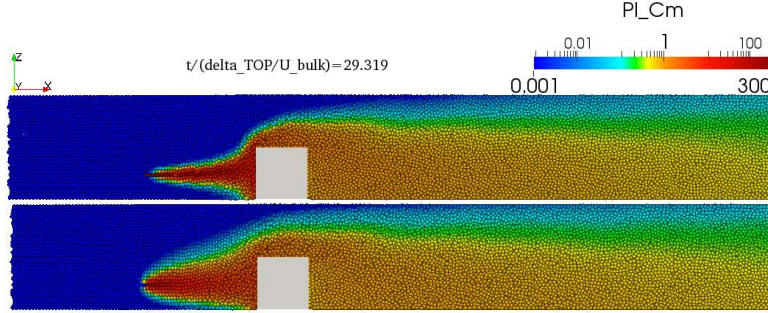


Figure 15. Confined flow past a wall-mounted cube with CPS. Vertical slices ($y/H_b=y_{PS}/H_b=0$) of the field of π_C^- . Top panel: reference simulation (Sc_T -TGS). Bottom panel: simulation with Sc_T -const (Amicarelli, 2024, [25]).

The Sc_T field depends on \bar{t}_{FP}/T_L and Re_T (or ν_T for sake of simplicity). The Lagrangian integral time scale T_L grows with the distance from any wall and decreases with larger Re_T , which occurs in the side recirculation regions, the cavity and the wake (Figure 16, top panel).

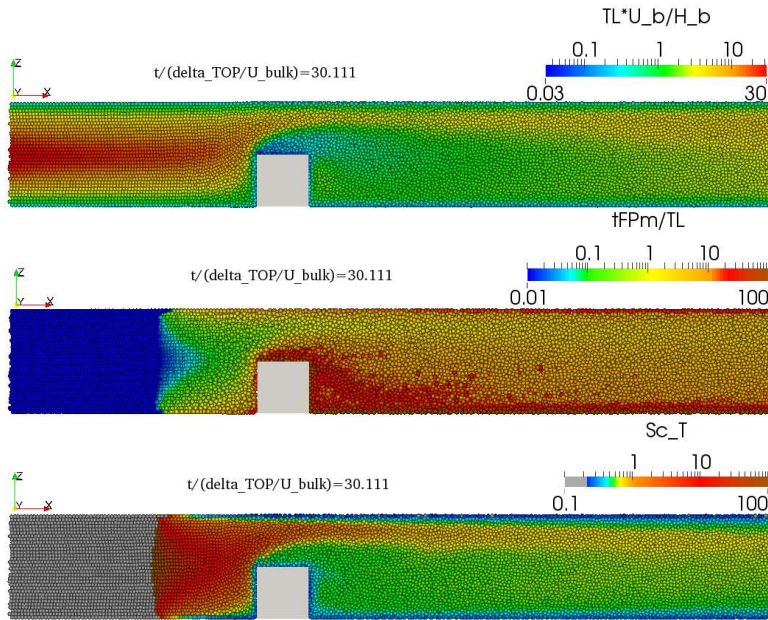


Figure 16. Confined flow past a cube with CPS: vertical slices ($y/H_b=0$) of the fields of $T_L U_b / H_b$ (top panel), \bar{t}_{FP} / T_L (centre panel) and Sc_T (bottom panel, reference simulation with Sc_T -TGS closure) at $t=t_f$.

In this reference section, T_L varies between zero (on the walls) to its maximum value at the core of the incoming flow where it is equal to ca.30 times the period necessary to make the fluid cover a cube face at the bulk velocity U_b (m/s), i.e. the average inlet mean velocity. The ratio \bar{t}_{FP}/T_L grows with the stream-wise distance and towards any wall due to larger t_{FLY} and smaller T_L values (Figure 16, centre panel). A relevant area of local maxima is shown in the recirculation regions where both the fluid particles and the SPH control volumes are entrapped for some flight time. This makes the lower half of the domain be featured by longer \bar{t}_{FP} values, also due to the speedup induced by the abrupt shrinkage in the upper half. These behaviours are amplified by the spatial pattern of T_L , except for the cavity core. The pure ballistic regime of pollutant transport (Sec.5.1) covers a small region close to the PS, whereas the turbulent-diffusion regime ($\bar{t}_{FP}/T_L \geq 20$) rules the recirculation regions and the

SPH particles close to the downstream walls. The SCT field (Figure 16, bottom panel) strongly depends on \bar{t}_{fp}/T_L , except for the cavity core due to the counterbalancing effect of a maximum area of Ret . The value of $SCT=0.72$ (SCT -const approach, Sec.1) is representative of a very limited volume, mainly in the upper half of the domain, downstream the shrinkage. This makes SCT -TGS induce relevant SCT reductions upstream the obstacle and appreciable SCT increases in the cavity and wake regions. It explains why the validation of the mean concentration, which only occurs in the cavity and the wake, is not practically affected by the improvements to SCT , contrarily to the assessment of the plume evolution upstream the obstacle. SCT globally ranges from ca.0.2 at the top wall to over 100 in the core of the cross-stream section containing the PS.

The integrated application of the spatial reconstruction schemes for the mean pressure and the mean TKE (Sec.4), the C_1 -consistent SPH quadrature formulae (Sec.3), several stabilisation strategies (Amicarelli, 2024, [25]) and the SPH-TSE filter (Amicarelli, 2025, [26]) at the grid points permits to reproduce a regular field of the non-dimensional mean pressure (Figure 17). The horizontal slice of the mean reduced-pressure coefficient π_{p_r} passing for the obstacle barycentre shows the upstream stagnation area, the depression volumes in the side recirculation regions and a downstream area of local maxima along the domain centreline where the downward flow interacts with the bottom wall.

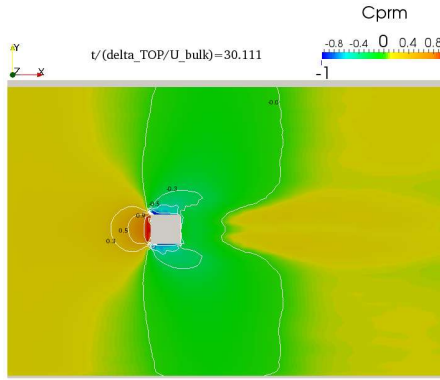


Figure 17. Confined flow past a cube with CPS. Horizontal slice ($z=H_b/2$) of the mean reduced-pressure coefficient π_{p_r} at $t=t_f$; iso-lines (-0.5, -0.3, 0, 0.3, 0.5, 0.9) reconstructed from the points of the positioning grid.

The combined application of the spatial reconstruction scheme for the mean TKE (Sec.4.2), the C_1 -consistent SPH quadrature formulae (Sec.3), several stabilisation strategies (Amicarelli, 2024, [25]) and the RANS Wall Functions (Amicarelli, 2024, [25]) allows the code to reproduce a proper field of \bar{q} , as demonstrated by the quantitative validations in Amicarelli (2024, [25]). Here a further qualitative demonstration is given by the cross-stream vertical slice containing the trailing edge (Figure 18) where the regular field of the mean TKE shows an arch of maxima in the side recirculation regions. This pattern of \bar{q} peaks matches the upper bound of the experimental arch vortex described in Martinuzzi & Tropea (1993, [64]) just downstream the trailing edge.

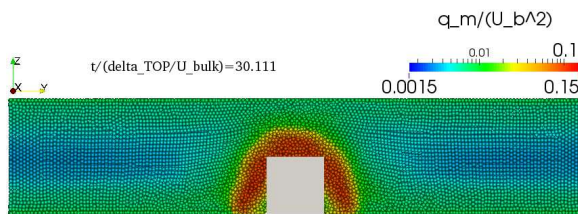


Figure 18. Confined flow past a cube with CPS. Cross-stream vertical slice containing the trailing edge ($x=H_b$) of the non-dimensional \bar{q} at $t=t_f$.

The computational cost of the reference simulation is quantified by $TVM=15.1\text{GB}$ and $t_{ela}=\text{ca.}17\text{h}04\text{min}$ on 3.5 physical cores (with hyper-threading) of an i9-13900HX CPU processor.

Compared to the simulation with Sct -const approach (Amicarelli, 2024, [25]), the elapsed time t_{ela} of the reference simulation with the Sct -TGS closure shows an increase of ca.3% as all the new quantities are computed on the fly to minimise TVM . The very small number of cores is only due to a very-low-cost operative strategy; about massively-parallelised SPH runs, one might refer to Cui et al. (2020, [66]) results of 1024-core SPH simulations on the impingement and solidification of Super-cooled Large Droplets on aircraft surfaces.

10. CONCLUSIONS

The turbulent Schmidt number Sct is systematically assumed constant (' Sct -const approach') by deterministic RANS CFD codes in assessing the mean concentration. This is equivalent to setting Sct to an intermediate value all over the domain, neglecting the effects of velocity autocorrelation and the dependence of Sct on the turbulence Reynolds number Ret . Out of the extreme condition ($Re_t \rightarrow \infty$), using any constant Sct value does not satisfy any configuration, not even the simplest turbulent-diffusion regime under HIT. Despite being a useful state-of-the-art practise, the adoption of any constant Sct value determines a systematic overestimation/underestimation of the turbulent dispersion coefficient K_T at small/large flight times since the Pollutant Source PS.

To overcome these limits, the simple Sct -TGS turbulence closure is presented and validated. Sct -TGS analytically satisfies any regime of Taylor's theory (HIT) and is numerically constrained to grid turbulence and a shear flow. These three general test cases are considered sufficient to constrain the constants of most of the turbulence closures to RANS-ME (e.g., k-eps model) to make them apply under general conditions. Sct -TGS applies under non-stationary and inhomogeneous conditions, considering local values for \tilde{C}_0 , T_L , R_m , S_m and T_E . The effects of velocity autocorrelation (e.g. Fang et al., 2022, [56]) and the systematic dependence of Sct on Ret are reproduced via the peak value of the compensated velocity Lagrangian structure function \tilde{C}_0 so that bias of the state-of-the-art deterministic CFD codes in assessing the mean concentration of passive pollutants is inhibited. Sct -TGS adopts the concept of 'time-dependent diffusivity' (Sykes et al., 1984, [15]; Pope, 2011, [57]) making RANS Cm-BE represent any regime of scalar transport in turbulent flows instead of working as a turbulent-diffusion model. Sct closures require this adaptation because using the physically-based limit Sct_{min} all over the domain would provide a consistent turbulent-diffusion model, but it would also lead to a sound failure everywhere in the domain, due to time-cumulated overestimation errors of the plume spread at small values of the weighted ensemble mean of the pollutant flight time \bar{t}_{FP} . Sct -TGS closure do not depend on the mean-scalar field, but on the properties of the transporting flow and \bar{t}_{FP} , which is here unaffected by the pollutant properties, except for the PS position.

Sct -TGS is the default Sct approach of CFD-OUT-sweePDF v.2.0.0 (Amicarelli et al.). It is a Lagrangian deterministic RANS CFD-SPH code for turbulent flows with pollutant dispersion under stationary and non-stationary regimes. Thanks to Sct -TGS, Sct has a hyperbolic behaviour close to the Pollutant Source PS; under large flight times Sct tends to the minimum Sct_{min} that only depends on Ret . Sct -TGS formulation is approximately defined for any number/shape/size of PSs and any BC/IC for \bar{C} . Sct -TGS is proposed for both Lagrangian and Eulerian deterministic RANS CFD codes. However its application might be more effective for Lagrangian codes due to assessing \bar{t}_{FP} .

Sct -TGS numerical validations concern three test cases by comparisons with the available closed-form solutions (Anand & Pope, 1985, [6], with a minor generalisation in Sec.12.3) and measurements (Fackrell & Robins, 1982, [9]), the numerical results of a stochastic RANS-LSM model (Amicarelli et al., 2011, [27]) and the previous version of the aforementioned code using the Sct -const approach (Amicarelli, 2024, [25]). These incremental validations involve grid turbulence, an experimental turbulent shear flow with elevated PS and a confined turbulent flow past a wall-mounted cubic obstacle with Canyon PS. These benchmarks are associated with full scale applications to Duct/Outdoor/Indoor Air Quality.

Under grid turbulence, the RANS CFD-SPH code using the SCT -TGS closure reduces the SCT -const errors of slight over-diffusion (near enough the PS) and relevant under-diffusion (far enough from the PS) down to negligible values.

In the shear flow, the mean concentration assessed with the SCT -TGS closure is close to the experimental values. SCT -TGS relevantly reduces the turbulent dispersion overestimated by SCT -const approach near the PS, with \bar{C} improvements up to one order of magnitude. SCT -TGS fills most of the gap between deterministic RANS CFD, featured by the SCT -const approach, and stochastic RANS CFD in simulating the dispersion of a passive pollutant in a turbulent shear flow, provided the same accuracy level for the velocity statistics. SCT -TGS makes the plume depict a linear shape in the ballistic regime of turbulent transport near the PS, analogously to Taylor's theory (Taylor, 1922, [24]) and contrarily to the parabolic shape that the SCT -const plume reproduces all over the domain.

The SCT field depends on the ratio \tilde{t}_{FP}/T_L and Re_T . All these quantities are estimated by the code. T_L grows with the distance from any wall (showing a near-wall linear behaviour) and decreases with larger Re_T , which occurs in the side recirculation regions, the cavity and the wake zones of the confined flow around the wall-mounted cubic obstacle. The ratio \tilde{t}_{FP}/T_L grows with the stream-wise distance and also towards any wall due to larger t_{FLY} and smaller T_L values; local maxima are shown in the recirculation regions where both the fluid particles and the SPH control volumes are entrapped for some flight time. The ballistic regime of turbulent transport ($\tilde{t}_{FP} \leq ca.0.05T_L$) is detected close to the PS, whereas the turbulent-diffusion regime ($\tilde{t}_{FP} \geq ca.20T_L$) rules the recirculation regions and the most downstream zones, especially close to walls. The SCT field strongly depends on \tilde{t}_{FP}/T_L , except for the cavity core due to the counterbalancing effect of Re_T . The discrete values of SCT globally ranges from ca.0.2 to over 100 at the core of the cross-stream section containing the PS.

A simple analytical turbulence closure on SCT for the mean concentration, constrained to Taylor's theory (Taylor, 1922, [24]), grid turbulence and a shear flow, might be a novelty in CFD. The assessment of T_L seems an original contribution of the current code in the scope of deterministic CFD. A SCT closure independent of the mean-scalar field and the computation of \tilde{t}_{FP} might represent original items together with the dependence of SCT on Re_T via \tilde{C}_0 , under any transport regime.

SCT -TGS represents a closed-form solution, thus it is formally a 0-equation first-order closure, analogously to the mixing-length model for RANS ME. These closures try to improve the results given by the simpler use of a constant Schmidt turbulent number or a constant artificial viscosity. Using a second-order closure to RANS Cm-BE on the turbulent transport term represents a more expensive task whose effectiveness has to be proven, when compared with first-order SCT closures for deterministic RANS or with RANS-PDF, whose accuracy is superior to any SCT closure.

In the worst-case scenario, where SCT -TGS will fail in any other configuration different from HIT, grid turbulence, shear flow and a fluid flow past a bluff body, then SCT -TGS could be exploited by any RANS deterministic model at least to properly treat these four general configurations without those systematic errors which currently affect the state-of-the-art SCT -const approach.

The adoption of a constant SCT value was sometimes useful for data-assimilation or calibration purposes as a diagnostic strategy and/or to compensate some numerical bias (e.g., in the estimation of the mean TKE). Analogously, the SCT -TGS closure might be multiplied by an explicit calibration/assimilation factor within the same scope.

The turbulence closure SCT -TGS might also interest RANS-SPDF (Scalar PDF) models (Haworth, 2010, [67]), a category of stochastic RANS CFD codes that do not reproduce velocity autocorrelation. SCT -TGS might also apply to the turbulent Prandtl number for the diffusion of the mean temperature. SCT -TGS could constrain the Sub-Grid-Scale (SGS) turbulent Schmidt number SCT,Δ used in some LES models as in Meringolo et al. (2024, [68]). This represents one of the rare LES SPH studies on pollutant transport with explicit turbulent transport term, giving a physically-based value to the SGS coefficient of turbulent dispersion. That study assumed $SCT,\Delta=0.70$, focused on water quality,

considered an active pollutant (i.e. buoyancy effects were simulated) and provided a quantitative validation on the LES-filtered concentration in 2D.

Considering the four configurations (HIT and the three test cases), the two alternative closures S_{CT} -TLS and S_{CT} -StHIT are less accurate than S_{CT} -TGS, but more accurate than S_{CT} -const approach, except for S_{CT} -StHIT that is slightly less correct under grid turbulence. This exception is removed if the domain is lengthened. S_{CT} -TLS is equivalent to S_{CT} -TGS under HIT and grid turbulence; S_{CT} -StHIT is equivalent to S_{CT} -TGS in the shear flow.

A separate validation involves the Sub-Particle Pollutant Source (SPPS) scheme. It is a ‘sub-grid’ spatial reconstruction scheme for \bar{C} working in a very limited region just downstream the PS. SPPS allows to set the size of the numerical PS conveniently larger than the physical PS, minimising any spurious numerical diffusion at PS. It is constrained to the model of Cushman-Roisin (2019, [62]) for the intrusion of a turbulent jet in a still environment. SPPS freezes \bar{C} for a distance of very few particle sizes from the PS to permit the small physical plume to correctly reach the particle size. The use of a sub-grid scheme to reconstruct \bar{C} around the PS seems an original contribution to CFD.

Some code features validated in Amicarelli (2024, [25]) are provided with detailed descriptions in the current paper, as they are active and further tested with the current simulations. It is the SPH quadrature formulae and the spatial reconstruction schemes for the mean pressure, the mean TKE and the mean concentration at the PS. The SPH spatial filters of a generic function, gradient and ‘quasi-Laplacian’ consider contributions from fluid particles, solid particles and fixed-wall elements. The SPH quadrature formulae rely on the assessment of relative positions, kernel functions and gradients, and are also computed over the barycentres of the positioning grid and the monitoring points. It is demonstrated that each SPH filter represents a spatial filter in the continuum plus a 3D open weighted quadrature formula for given irregular nodes. The formulations for all the SPH-TSE ensemble statistics and the SPH spatial statistics of the code are presented. The approximations of gradients and functions are systematically assessed by C_1 -consistent SPH quadrature formulae in the BE terms and the spatial reconstruction schemes, including boundary contributions in the renormalisation matrix, whereas SPH models usually adopt C_0 -consistent approximations with few and partial exceptions (e.g., Marongiu et al. 2010, [69]; Lind et al., 2012, [70]; Amicarelli et al. 2017, [71]; Khayyer et al., 2018, [72]; Chen et al., 2022, [41]). Unlike the mesh-based CFD codes for Air Quality (e.g. Efthimiou et al., 2016, [55]), the code of Sec.2 adopts a more approximated emission scheme to represent the Pollutant Source, exploiting the SPH Lagrangian approach.

The pre-processing procedures for the inlet mean-TKE dissipation rate and the depth of the turbulent Boundary Layer are also reported. The code simulations show limited elapsed times even if the executions only used 3.5 physical cores due to a very-low-cost operative strategy. Concentration turbulent fluctuations are neglected; they are relevant in case of non-linear relationships between concentration and damage as for odour dispersion (e.g. Viccione et al., 2014, [73]).

Acknowledgements

This study received no public funding. Formal details on the code CFD-OUT-sweePDF v.2.0.0 (Amicarelli et al.) are reported at <https://www.researchgate.net/profile/Andrea-Amicarelli> and github.com/AndreaAmicarelli-personal. Videos on the results of CFD-OUT-sweePDF are published at <https://www.youtube.com/@andrea.amicarelli>. Regarding those source-code parts which were imported in CFD-OUT-sweePDF v.1.0.0 (Amicarelli et al.) from SPHERA v.10.0.0 (RSE SpA) — as mentioned in the last lines of Sec.2, Sec.3.4 and Sec.3.6, with detailed references to the associated papers — the following notice applies: ‘SPHERA v.10.0.0 was realised by RSE SpA thanks to the funding “Fondo di Ricerca per il Sistema Elettrico” within the frame of a Program Agreement between RSE SpA and the Italian Ministry of Economic Development (Ministero dello Sviluppo Economico)’.

Disclosure statement

The author reports there are no competing interests to declare.

11. APPENDIX A: PRE-PROCESSING PROCEDURES

Two general pre-processing procedures for the code of Sec.2 are executed in the current study as well as in Amicarelli (2024, [25]) and Amicarelli (2025, [26]). They concern the inlet mean-TKE dissipation rate (Sec.11.1) and the depth of the turbulent boundary layer (Sec.11.2).

11.1. Inlet mean-TKE dissipation rate

The inlet values for the mean-TKE dissipation rate $\bar{\varepsilon}$ can be set following five alternative formulae:

$$\begin{aligned} \bar{\varepsilon} &= \begin{cases} \frac{u_*^3}{k_v r}, & \frac{11\bar{\nu}}{u_*} < r \leq \delta_{NSBL,\bar{\varepsilon}} \\ 0, & 0 < r \leq \frac{11\bar{\nu}}{u_*} \end{cases}; \quad \bar{\varepsilon} = \max \left\{ 0.6\bar{q} \left[(-S_m) R_m \right]^{\frac{1}{4}}; \bar{\varepsilon}_{\lim} \right\}, \quad \bar{\varepsilon}_{\lim} = \frac{1}{2} \sqrt{\frac{3}{2}} \frac{(C_\mu)^{\frac{3}{4}} \sigma_w \bar{q}}{k_v r}; \\ \bar{\varepsilon} &= \max \left\{ 0.6\bar{q} \sqrt{-S_m}; \bar{\varepsilon}_{\lim} \right\}; \quad \bar{\varepsilon} = \max \left\{ -\bar{u}' \bar{w}' \frac{\partial \bar{u}}{\partial z}; \bar{\varepsilon}_{\lim} \right\}; \quad \bar{\varepsilon} = \frac{u_*^3}{k_v r} \left(1 - \frac{r}{\delta_T} \right)^{\frac{3}{2}}, \quad \delta_{NSBL,\bar{\varepsilon}} < r \leq \delta_T \end{aligned} \quad (11.1)$$

where k_v is von Karman constant and σ_w (m/s) is the standard deviation of the vertical velocity; δ_{NSBL} (m) and δ_T (m) are the depths of the Neutral Surface Boundary Layer (NSBL) and the Turbulent BL. The first formulation in (11.1) is used as WF in the code of Sec.2 (Amicarelli, 2024, [25]). The two following formulations are the closed-form solutions of TKE-BE under homogeneous and stationary turbulence, according to either Kat&Lau-k-eps turbulence closure (Sec.2) or k-eps model (commonly used in CFD for atmospheric flows, e.g. Efthimiou et al., 2021, [74]). A limiter ' $_{\lim}$ ' applies to avoid unphysical underestimations of $\bar{\varepsilon}$, incoherent with the distance from the fixed wall r (m); it involves an approximate value of the Eulerian integral time scale of turbulence in the NSBL. The limiter is imposed only where necessary to minimise the corrections to the raw experimental input data. The fourth expression assumes a simplified 1D TKE-BE and the 3D definition of the friction velocity u_* (m/s), without assumptions on the mean-velocity gradient. The last formula in (11.1) can be derived for the Neutral Outer Boundary Layer (NOBL) as in Amicarelli (2024, [25]). The formulations in (11.1) are reported in order of decreasing priority, considering their accuracy and coherence with the rest of the code. Such order can be revised according to the actual availability and reliability of the experimental data. In case of 2D simulations with 1D mean flow, the fourth expression is preferred to the previous two ones. If \bar{q} BCs and ICs are set in terms of WF or NOBL profile, it seems more coherent to apply the analogous profiles of $\bar{\varepsilon}$, unless measurements indicate otherwise.

11.2. An operative definition for the depth of the turbulent Boundary Layer

The depth of the turbulent Boundary Layer δ_T , requested to assess δ_{NSBL} for the WFs of the code (Sec. 2) and for other pre-processing procedures, is provided as an input value. The following operative definition is function of the distance from the wall r (m):

$$\begin{aligned} \delta_T &= \min_i \{r_i\}, \quad r_1 = \min_j \left\{ r_j : \frac{\bar{u}_\tau \Big|_{r_j}}{\bar{u}_\tau \Big|_{0.3r_j}} = 1.1 \right\}, \quad r_2 = \min_j \left\{ r_j : u_*^2 \Big|_{r_j} \leq 0.05 u_*^2 \Big|_{r_{\min}} \right\}, \\ r_3 &= \min_j \left\{ r_j : \bar{q} \Big|_{r_j} \leq 0.05 \bar{q} \Big|_{r_{\min}} \right\}, \quad r_4 = \min_j \left\{ r_j : \sigma_u \Big|_{r_j} \leq 0.05 \sigma_u \Big|_{r_{\min}} \right\}, \\ r_5 &= \min_j \left\{ r_j : \sigma_v \Big|_{r_j} \leq 0.05 \sigma_v \Big|_{r_{\min}} \right\}, \quad r_6 = \min_j \left\{ r_j : \frac{\partial \bar{u}_\tau}{\partial r} \Big|_{r_j} > 0 \right\}, \quad r_7 = \min_j \left\{ r_j : \text{Re}_T \Big|_{r_j} \leq 0.05 \right\} \end{aligned} \quad (11.2)$$

whose minima can be assessed over the inlet section, for sake of simplicity; \bar{u}_τ (m/s) is the tangential-to-wall component of the mean velocity, σ_i (m/s) is a standard deviation of velocity. The distance r_1

is coherent with the WFs reported in Amicarelli (2024, [25]). The distance r_6 is useful if the fluid-wall relative velocity changes direction not far from the wall, under complex flows. The following definition of the friction velocity in the BL ($u_{*,r}^2 \equiv -\overline{u'w'}|_r$) might be useful to assess the quantities in (11.2), which does not need any WF to be computed. Besides any simple operative definition of δ_T for a CFD code, thorough analyses on the evolution of the Boundary Layer depth are available in specific studies (e.g., Moroni & Cenedese, 2006, [75]; Catalano et al., 2012, [76]).

12. APPENDIX B: CLOSED-FORM SOLUTIONS IN GRID TURBULENCE

This appendix collects the closed-form solutions used to validate the numerical results of Sec.7.

12.1. Grid turbulence: closed-form solutions for the transporting fluid flow

The grid-turbulence approximation is usually treated under the ‘active-grid limit’, as defined by Bos (2020, [63]): turbulence is only produced at the grid location, instantaneously, and decreases along the physical-particle trajectories downstream the grid section. Grid-turbulence conditions under the active-grid limit are also cited as ‘grid-decaying turbulence’ and can be represented by a numerical simulation solving the flow downstream the grid section, without an explicit mechanical grid. The following hypotheses apply. The transporting fluid flow is homogeneous in the cross-stream direction and the mean velocity is uniform; gravity and the mean pressure are non-influential; the flow is stationary and satisfies Taylor’s translation hypothesis for turbulence. The closed-form solutions for the mean TKE and its dissipation rate are reported in Bos (2020, [63]), among the others:

$$\bar{q} = \frac{\bar{q}_g}{\left(1 + \frac{t_{FLY} - t_g}{t_*}\right)^n}, \quad t_g \equiv t_{FLY}|_{x_g}, \quad \bar{\varepsilon} = \frac{\bar{\varepsilon}_g}{\left(1 + \frac{t_{FLY} - t_g}{t_*}\right)^{n+1}}, \quad t_* = n \frac{\bar{q}_g}{\bar{\varepsilon}_g}, \quad n = \frac{1}{C_{\varepsilon_2} - 1} \approx 1.09 \quad (12.1)$$

where the value of the constant $C_{\varepsilon_2} = 1.92$ relates to k-eps modelling and the time scale t_* (s) is found to be slightly larger than the Eulerian time scale at the grid location ‘ g ’.

12.2. Grid turbulence: state-of-the-art analytical solution for the mean concentration

The analytical solution for the mean concentration of a passive scalar assumes a stationary uniform step PS covering the lower half of the domain depth (Anand & Pope, 1985, [6]):

$$\bar{C} = \frac{1}{2} \bar{C}_{\max} \left[1 - \operatorname{erf} \left(\frac{z}{\sqrt{2} \sigma_{z^+}} \right) \right], \quad \operatorname{erf}(\infty) = 1, \quad \lim_{z \rightarrow -\infty} \bar{C} = \bar{C}_{\max} \quad (12.2)$$

The formula for the plume spread σ_{z^+} net of the PS size reads (Anand & Pope, 1985, [6]):

$$\sigma_{z^+} = 2D_M (t_{FLY} - t_{PS}) + \frac{4}{3} \bar{q}_{PS} t_{PS-g}^2 \left[\frac{\left(1 + \frac{t_{FLY} - t_{PS}}{t_{PS-g}}\right)^{r-s}}{r(r-s)} + \frac{\left(1 + \frac{t_{FLY} - t_{PS}}{t_{PS-g}}\right)^{-s}}{rs} - \frac{1}{s(r-s)} \right] \quad (12.3)$$

It relied on a simplified closed-form solution for the mean TKE (Anand & Pope, 1985, [6], considering Sawford, 2004, [77]):

$$\bar{q} = \frac{\bar{q}_{PS}}{\left(1 + \frac{t_{FLY} - t_{PS}}{t_{PS-g}}\right)^m}, \quad t_{PS-g} \equiv t_{PS} - t_g \approx \frac{x_{PS} - x_g}{u}, \quad x_{PS} - x_g > 10M, \quad t_{PS} \equiv t_{FLY}|_{x_{PS}} \quad (12.4)$$

which is alternative to (12.1) and is equivalent to analogous expressions (e.g.: Brown & Bilger, 1996, [78]; Sawford, 2004, [77]; Sawford, 2006, [79]; Pope, 2011, [57]). These simplified solutions depend

on the travel time t_{PS-g} (s) between the mechanical grid and the Pollutant Source, the grid spacing M (m) and the experimental parameter m , which is tuned on a limited subdomain of interest. The constants r and s in (12.3) are defined as follows (Anand & Pope, 1985, [6]):

$$r \equiv \frac{t_{PS-g}}{T_{L,PS}} - \frac{m}{2} + 1, \quad s \equiv \frac{t_{PS-g}}{T_{L,PS}} + \frac{m}{2} - 1, \quad r-s = 2-m \quad (12.5)$$

The present formulation (12.2), (12.3) and (12.5) is the main reference under grid turbulence. However, it is featured by the following shortcomings: the underlying approximation of the mean TKE (12.4) introduces an appreciable error; the parameter m is test-case dependent and needs an experimental tuning procedure; the Pollutant Source has to be located downstream the mechanical grid at a distance sufficiently large as noticed in (12.4).

12.3. Grid turbulence: generalised analytical solution for the mean concentration

Two items are introduced to remove the shortcomings described at the end of Sec.12.2: the first is the replacement of the mean-TKE expression; the second is a general closure. While (12.2) keeps unaltered, the accurate expression for the mean TKE (12.1) replaces its approximated version (12.4). The two formulae are formally equal, provided that $(t_{FLY} - t_{PS})$ replaces $(t_{FLY} - t_g)$, n substitutes m and t^* replaces t_{PS-g} . The same formal equivalence applies to $\bar{\varepsilon}$, which is directly derived from \bar{q} , and to T_E , being the ratio between \bar{q} and $\bar{\varepsilon}$. Following step by step the demonstration of Anand & Pope (1985, [6]), one observes that the replacement of $(t_{FLY} - t_g)$ is straightforward since (12.1) removes any constraint on the position of PS, which here conveniently overlaps the mechanical grid under the active-grid limit. The quantities t_{PS-g} and m affect the solution for \bar{C} only in terms of T_E : this determines that the last two replacements directly apply to (12.3) as follows:

$$\sigma_{z^+} = 2D_M(t_{FLY} - t_g) + \frac{4}{3}\bar{q}_g t_*^2 \left[\frac{\left(1 + \frac{t_{FLY} - t_g}{t_*}\right)^{r-s}}{r(r-s)} + \frac{\left(1 + \frac{t_{FLY} - t_g}{t_*}\right)^{-s}}{rs} - \frac{1}{s(r-s)} \right] \quad (12.6)$$

where the definitions of the constants r and s are coherently generalised:

$$r \equiv \frac{t_*}{T_{L,g}} - \frac{n}{2} + 1, \quad s \equiv \frac{t_*}{T_{L,g}} + \frac{n}{2} - 1, \quad r-s = 2-n \quad (12.7)$$

The time scale ratio in (12.7) is rearranged, recalling the expression for \tilde{C}_0 (5.24), to obtain a general closure to the system (12.2) and (12.6), which does not depend on benchmark-related constants:

$$r = \frac{n}{2} \left(\frac{3}{2} \tilde{C}_{0,g} - 1 \right) + 1, \quad s = \frac{n}{2} \left(\frac{3}{2} \tilde{C}_{0,g} + 1 \right) - 1, \quad \tilde{C}_{0,g} = \frac{C_0}{1 + \frac{70}{\sqrt{15 \text{Re}_{T,g}}}}, \quad \text{Re}_{T,g} = \frac{4}{9C_\mu} \frac{\nu_{T,g}}{\nu} \quad (12.8)$$

REFERENCES

- [1] Y. Tominaga and T. Stathopoulos, “Turbulent Schmidt numbers for CFD analysis with various types of flowfield,” *Atmospheric Environment*, vol. 41, no. 37, pp. 8091-8099, <https://doi.org/10.1016/j.atmosenv.2007.06.054>, 2007.
- [2] G. Efthimiou, S. Andronopoulos, R. Tavares and J. Bartzis, “CFD-RANS prediction of the dispersion of a hazardous airborne material released during a real accident in an industrial environment,” *Journal of Loss Prevention in the Process Industries*, vol. 46, pp. 23-36, <http://dx.doi.org/10.1016/j.jlp.2017.01.015>, 2017.

- [3] A. Venetsanos, E. Papanikolaou and J. Bartzis, “The ADREA-HF CFD code for consequence assessment of hydrogen applications,” *Int. J. Hydrot. Energy*, vol. 35, pp. 3908–3918, <https://doi.org/10.1016/j.ijhydene.2010.01.002>, 2010.
- [4] D. Violeau, “Explicit algebraic Reynolds stresses and scalar fluxes for density-stratified shear flows,” *Phys. Fluids*, vol. 21, p. 035103, 2009.
- [5] K.-J. Hsieh, F.-S. Lien and E. Yee, “Numerical modeling of passive scalar dispersion in an urban canopy layer,” *Journal of Wind Engineering and Industrial Aerodynamics*, vol. 95, pp. 1611–1636, doi:10.1016/j.jweia.2007.02.028, 2007.
- [6] M. S. Anand and S. B. Pope, “Diffusion behind a line source in grid turbulence,” in *Turbulent shear flows*, vol. 4, Berlin, Springer-Verlag, edited by Bradbury L.J.S., Durst F., Launder B.E., Schmidt F.W., Whitelaw J.H., 1985, p. 46–61.
- [7] L. Dong, H. Zuo, L. Hu, B. Yang, L. Li and L. Wu, “Simulation of heavy gas dispersion in a large indoor space using CFD model,” *Journal of Loss Prevention in the Process Industries*, vol. 46, pp. 1–12, <https://doi.org/10.1016/j.jlp.2017.01.012>, 2017.
- [8] A. Issakhov, A. Alimbek and A. Issakhov, “A numerical study for the assessment of air pollutant dispersion with chemical reactions from a thermal power plant,” *Engineering Applications of Computational Fluid Mechanics*, vol. 14, no. 1, pp. 1035–1061, <https://doi.org/10.1080/19942060.2020.1800515>, 2020.
- [9] J. Fackrell and A. Robins, “Concentration fluctuations and fluxes in plumes from point sources in a turbulent boundary layer,” *Journal of Fluid Mechanics*, vol. 117, p. 1–26, 1982.
- [10] J.-J. Baik, Y.-S. Kang and J.-J. Kim, “Modeling reactive pollutant dispersion in an urban street canyon,” *Atmospheric Environment*, vol. 41, pp. 934–949, doi:10.1016/j.atmosenv.2006.09.018, 2007.
- [11] Y. Tominaga, S. Iizuka, M. Imano, H. Kataoka, A. Mochida, T. Nozu, Y. Ono, T. Shirasawa, N. Tsuchiya and R. Yoshie, “Cross Comparisons of CFD Results of Wind and Dispersion Fields for MUST Experiment: Evaluation Exercises by AJI,” *Journal of Asian Architecture and Building Engineering*, vol. 12, no. 1, pp. 117–124, <https://doi.org/10.3130/jaabe.12.117>, 2013.
- [12] E. Yee and C. Biltoft, “Concentration fluctuation measurement in a plume dispersing through a regular array of obstacles,” *Boundary-Layer Meteorology*, vol. 111, pp. 363–415, <https://doi.org/10.1023/B:BOUN.0000016496.83909.ee>, 2004.
- [13] P. A. Libby and C. A. Scragg, “Diffusion of heat from a line source downstream of a turbulence grid,” *AIAA Journal*, vol. 11, no. 4, pp. 562–563, <https://doi.org/10.2514/3.6795>, 1973.
- [14] J. W. Deardorff, “Closure of second- and third-moment rate equations for diffusion in homogeneous turbulence,” *Phys. Fluids*, vol. 21, no. 4, pp. 525–530, 1978.
- [15] R. I. Sykes, W. S. Lewellen and S. F. Parker, “A turbulent-transport model for concentration fluctuations and fluxes,” *Journal of Fluid Mechanics*, vol. 139, pp. 193–218, <https://doi.org/10.1017/S002211208400032X>, 1984.
- [16] B. Sawford, P. Yeung and J. Hackl, “Reynolds Number Dependence of Relative Dispersion Statistics in Isotropic Turbulence,” *Physics of Fluids*, vol. 20, no. 065111, p. <https://doi.org/10.1063/1.2946442>, 2008.
- [17] B. Sawford and J.-F. Pinton, “A Lagrangian view of turbulent dispersion and mixing,” in *Ten chapters in turbulence*, Cambridge University Press, edited by P.A. Davidson, Y. Kaneda and K.R. Sreenivasan, 2013, pp. Chapter 4, page 131–175, <https://doi.org/10.1017/CBO9781139032810.005>.
- [18] S. B. Pope, “PDF methods for turbulent reacting flows,” *Progress in Energy and Combustion Science*, vol. 11, p. 119–192, 1985.
- [19] P. M. Morkisz and P. Przybylowicz, “Optimal pointwise approximation of SDE’s from inexact information,” *Journal of Computational and Applied Mathematics*, vol. 324, pp. 85–100, <http://dx.doi.org/10.1016/j.cam.2017.04.023>, 2017.
- [20] M. Bahlali, E. Dupont and B. Carissimo, “A hybrid CFD RANS/Lagrangian approach to model atmospheric dispersion of pollutants in complex urban geometries,” *Int. J. Environ. Pollut.*, vol. 64, no. 1–3, pp. 74–89, DOI <https://doi.org/10.1504/IJEP.2018.099150>, 2018.

- [21] M. Bahlali, E. Dupont and B. Carissimo, "Atmospheric dispersion using a Lagrangian stochastic approach: application to an idealized urban area under neutral and stable meteorological conditions," *J Wind Eng Ind Aerodyn*, vol. 193, no. 103976, p. DOI <https://doi.org/10.1016/j.jweia.2019.103976>, 2019.
- [22] D. J. Thomson, "Criteria for the selection of the stochastic models of particle trajectories in turbulent flows," *Journal of Fluid Mechanics*, vol. 180, pp. 529-556, 1987.
- [23] C. Gariazzo, A. Pelliccioni, M. Bogliolo and et al., "Evaluation of a Lagrangian Particle Model (SPRAY) to Assess Environmental Impact of an Industrial Facility in Complex Terrain," *Water, Air, & Soil Pollution*, vol. 155, pp. 137–158, <https://doi.org/10.1023/B:WATE.0000026525.82039.ef>, 2004.
- [24] G. Taylor, "Diffusion by continuous movements," *Proceedings of the London Mathematical Society*, Vols. s2-20, no. 1, pp. 196-212, <https://doi.org/10.1112/plms/s2-20.1.196>, 1922.
- [25] A. Amicarelli, "A Lagrangian RANS CFD-SPH code for turbulent flows with pollutant transport and applications to Outdoor/Indoor/Duct Air Quality," *International Journal of Computational Fluid Dynamics*, vol. 38, no. 5, p. 339–376; <https://doi.org/10.1080/10618562.2025.2469497>, 2024.
- [26] A. Amicarelli, "RANS SPH CFD for micro-scale meteorology and Air Quality in and around Urban Canopies," *paper preprint*, pp. 1-30, protocol, RS2502, 2025.
- [27] A. Amicarelli, G. Leuzzi, P. Monti and D. J. Thomson, "A comparison between IECM and IEM Lagrangian models," *International Journal of Environment and Pollution*, vol. 44, no. 1/2/3/4, pp. 324-331, DOI 10.1504/IJEP.2011.038433, 2011.
- [28] D. Isik and Z. He, "SPH Viscous Flow Around a Circular Cylinder: Impact of Viscous Formulation and Background Pressure," *International Journal of Computational Fluid Dynamics*, vol. 35, no. 6, pp. 451-467, DOI: 10.1080/10618562.2021.1979523, 2021.
- [29] J. Galindo, R. Navarro, L. M. García-Cuevas, D. Tarí, H. Tartoussi and S. Guilain, "A zonal approach for estimating pressure ratio at compressor extreme off-design conditions," *International Journal of Engine Research*, vol. 20, no. 4, pp. 393-404, <https://doi.org/10.1177/1468087418754899>, 2018.
- [30] R. Vignjevic and J. Campbell, "Review of Development of the Smooth Particle Hydrodynamics (SPH) Method," in *Predictive Modeling of Dynamic Processes*, Boston, Springer, S. Hiermaier (ed.), 2009, pp. 367-396, https://doi.org/10.1007/978-1-4419-0727-1_20.
- [31] A. Crespo, M. Gómez-Gesteira and R. Dalrymple, "Modeling Dam Break Behavior over a Wet Bed by a SPH Technique," *Journal of Waterway, Port, Coastal and Ocean Engineering*, vol. 134, no. 6, pp. 313-320, [https://doi.org/10.1061/\(ASCE\)0733-950X\(2008\)134:6\(313\)](https://doi.org/10.1061/(ASCE)0733-950X(2008)134:6(313)), 2008.
- [32] F. Aristodemo, S. Marrone and I. Federico, "SPH modeling of plane jets into water bodies through an inflow/outflow algorithm," *Ocean Engineering*, vol. 105, pp. 160-175, <https://doi.org/10.1016/j.oceaneng.2015.06.018>, 2015.
- [33] X. Cui, W. G. Habashi and V. Casseau, "Multiphase SPH Modelling of Supercooled Large Droplets Freezing on Aircraft Surfaces," *International Journal of Computational Fluid Dynamics*, vol. 35, no. (1-2), pp. 79-92, <https://doi.org/10.1080/10618562.2020.1817401>, 2020.
- [34] L. Fang, S. Wang and J. Hong, "Analytical expressions of the deformation limit of fluid particles," *Physics Letters A*, vol. 381, pp. 3996–4004, <https://doi.org/10.1016/j.physleta.2017.10.032>, 2017.
- [35] X. Cui, A. Bakkar and W. G. Habashi, "A multiphase SPH framework for supercooled large droplets dynamics," *International Journal of Numerical Methods for Heat & Fluid Flow*, vol. 29, no. 7, pp. 2434-2449, <https://doi.org/10.1108/HFF-10-2018-0547>, 2019.
- [36] B. Tagliafierro, M. Karimirad, I. Martínez-Estévez, J. M. Domínguez, G. Viccione and A. J. C. Crespo, "Numerical Assessment of a Tension-Leg Platform Wind Turbine in Intermediate Water Using the Smoothed Particle Hydrodynamics Method," *Energies*, vol. 15, no. 3993, pp. 1-23, <https://doi.org/10.3390/en15113993>, 2022.
- [37] A. Issakhov and A. Baitureyeva, "Modeling of a passive scalar transport from thermal power plants to atmospheric boundary layer," *International Journal of Environmental Science and Technology*, vol. 16, no. 8, pp. 4375-4392, <https://doi.org/10.1007/s13762-019-02273-y>, 2019.

- [38] A. Leroy, D. Violeau, M. Ferrand and C. Kassiotis, “Unified semi-analytical wall boundary conditions applied to 2-D incompressible SPH,” *Journal of Computational Physics*, vol. 261, pp. 106–129, <http://dx.doi.org/10.1016/j.jcp.2013.12.035>, 2014.
- [39] B. Launder and D. Spalding, “The numerical computation of turbulent flows,” *Comput. Meth. Applied Mech. Eng.*, vol. 3, no. 2, pp. 269-289, 1974.
- [40] L. Fang, H.-K. Zhao, L.-P. Lu, Y.-W. Liu and H. Yan, “Quantitative description of non-equilibrium turbulent phenomena in compressors,” *Aerospace Science and Technology*, vol. 71, pp. 78-89, <https://doi.org/10.1016/j.ast.2017.09.020>, 2017.
- [41] Y.-k. Chen, D. D. Meringolo and Y. Liu, “SPH study of wave force on simplified superstructure of open-type sea access road,” *Ocean Engineering*, vol. 249, no. 110869, pp. 1-30, <https://doi.org/10.1016/j.oceaneng.2022.110869>, 2022.
- [42] A. Di Monaco, S. Manenti, M. Gallati, S. Sibilla, G. Agate and R. Guandalini, “SPH modeling of solid boundaries through a semi-analytic approach,” *Engineering Applications of Computational Fluid Mechanics*, vol. 5, no. 1, pp. 1-15, DOI: 10.1080/19942060.2011.11015348, 2011.
- [43] SPHERA (RSE SpA), “<https://github.com/GiordanoAgateRSE/SPHERA>,” 2022. [Online].
- [44] A. Amicarelli, R. Albano, D. Mirauda, G. Agate, A. Sole and R. Guandalini, “A Smoothed Particle Hydrodynamics model for 3D solid body transport in free surface flows,” *Computers & Fluids*, vol. 116, p. 205–228; <https://doi.org/10.1016/j.compfluid.2015.04.018>, 2015.
- [45] A. Amicarelli, S. Manenti, R. Albano, G. Agate, M. Paggi, L. Longoni, D. Mirauda, L. Ziane, G. Viccione, S. Todeschini, A. Sole, L. Baldini, D. Brambilla, M. Papini, M. Khellaf, B. Tagliafierro, L. Sarno and G. Pirovano, “SPHERA v.9.0.0: a Computational Fluid Dynamics research code, based on the Smoothed Particle Hydrodynamics mesh-less method,” *Computer Physics Communications*, vol. 250, pp. 107157, <https://doi.org/10.1016/j.cpc.2020.107157>, 2020.
- [46] A. Amicarelli, S. Manenti and M. Paggi, “SPH modelling of dam-break floods, with damage assessment to electrical substations,” *International Journal of Computational Fluid Dynamics*, vol. 35, no. 1-2, pp. 3-21; <https://doi.org/10.1080/10618562.2020.1811240>, 2021.
- [47] A. Amicarelli, E. Abbate and A. Frigerio, “SPH modelling of a dike failure with detection of the landslide sliding surface and damage scenarios for an electricity pylon,” *International Journal of Computational Fluid Dynamics*, vol. 36, no. 4, pp. 265-293, <https://doi.org/10.1080/10618562.2022.2108020>, 2022.
- [48] B. Tagliafierro, S. Mancini, P. Ropero-Giralda, J. M. Domínguez, A. J. C. Crespo and G. Viccione, “Performance Assessment of a Planing Hull Using the Smoothed Particle Hydrodynamics Method,” *J. Mar. Sci. Eng.*, vol. 9, no. 244, pp. 1-18, <https://doi.org/10.3390/jmse9030244>, 2021.
- [49] R. W. Randles and L. D. Liberts, “Smoothed Particle Hydrodynamics. Some recent improvements and applications,” *Comput. Methods Appl. Mech. Engrg.*, vol. 139, pp. 375-408, 1996.
- [50] M. Basa, N. Quinlan and M. Lastiwka, “Robustness and accuracy of SPH formulations for viscous flow,” *International Journal for Numerical Methods in Fluids*, vol. 60, no. 10, pp. 1127-1148, DOI: 10.1002/fld.1927, 2009.
- [51] J. Monaghan and J. Lattanzio, “A refined method for astrophysical problems,” *Astronomy and Astrophysics*, vol. 149, pp. 135-143, 1985.
- [52] M. Gallati and G. Braschi, “Simulazione lagrangiana di flussi con superficie libera in problemi di idraulica,” in *L'ACQUA 5*, 2000.
- [53] S. Gu, X. Zheng, L. Ren, H. Xie, Y. Huang, J. Wei and S. Shao, “SWE-SPHysics simulation of dam break flows at South-Gate Gorges Reservoir,” *Water*, vol. 9, no. 6, pp. art. no. 387, <https://doi.org/10.3390/w9060387>, 2017.
- [54] J. Cercos-Pita, M. Antuono, A. Colagrossi and A. Souto-Iglesias, “SPH energy conservation for fluid-solid interactions,” *Comput. Methods Appl. Mech. Engrg.*, vol. 317, pp. 771–791, <http://dx.doi.org/10.1016/j.cma.2016.12.037>, 2017.
- [55] G. Efthimiou, S. Andronopoulos, I. Tolias and A. Venetsanos, “Prediction of the upper tail of concentration distributions of a continuous point source release in urban environments,” *Environmental Fluid Mechanics*, vol. 16, no. 5, pp. 899-921, DOI <https://doi.org/10.1007/s10652-016-9455-2>, 2016.

- [56] L. Fang, L. Li, J. Guo, Y. Liu and X. Huang, “Time scale of directional change of active Brownian particles,” *Physics Letters A*, vol. 427, no. 127934, p. <https://doi.org/10.1016/j.physleta.2022.127934>, 2022.
- [57] S. Pope, “Simple models of turbulent flows,” *PHYSICS OF FLUIDS*, vol. 23, pp. 011301, 1-19, DOI: 10.1063/1.3531744, 2011.
- [58] B. L. Sawford, “Reynolds number effects in Lagrangian stochastic models of turbulent dispersion,” *Phys. Fluids A*, vol. 3, pp. 1577-1586, 1991.
- [59] S. B. Pope, “Lagrangian PDF methods for turbulent flows,” *Annu. Rev. Fluid Mech.*, vol. 26, pp. 23-63, 1994.
- [60] S. Hanna and R. Britter, Wind Flow and Vapor Cloud Dispersion at Industrial and Urban Sites, New York: American Institute of Chemical Engineers, pp.1-208, ISBN 978-0-816-90863-9, 2002.
- [61] K. Bezpalcova, Physical modelling of flow and diffusion in urban canopy; PhD thesis, Prague: Charles University, 2007.
- [62] B. Cushman-Roisin, “Environmental Fluid Mechanics,” 2019. [Online]. Available: <http://www.dartmouth.edu/~cushman/books/EFM.html>. [Accessed 21 May 2019].
- [63] W. J. Bos, “Production and dissipation of kinetic energy in grid turbulence,” *Physical Review Fluids*, vol. 104607, pp. 1-26, DOI: 10.1103/PhysRevFluids.5.104607, 2020.
- [64] R. Martinuzzi and C. Tropea, “The flow around surface-mounted, prismatic obstacles placed in a fully developed channel flow,” *J. Fluids Eng.*, vol. 115, pp. 85-92, <https://doi.org/10.1115/1.2910118>, 1993.
- [65] I. Mavroidis, R. Griffiths and D. Hall, “Field and wind tunnel investigations of plume dispersion around single surface obstacles,” *Atmospheric Environment*, vol. 37, pp. 2903-2918, DOI: 10.1016/S1352-2310(03)00300-5, 2003.
- [66] X. Cui, W. G. Habashi and V. Casseau, “MPI Parallelisation of 3D Multiphase Smoothed Particle Hydrodynamics,” *International Journal of Computational Fluid Dynamics*, vol. 34, no. 7-8, pp. 610-621, DOI: 10.1080/10618562.2020.1785436, 2020.
- [67] D. Haworth, “Progress in probability density function methods for turbulent reacting flows,” *Progress in Energy and Combustion Science*, vol. 36, pp. 168–259, DOI: 10.1016/j.pecs.2009.09.003, 2010.
- [68] D. D. Meringolo, F. Aristodemo, S. Servidio and P. G. F. Filianoti, “Large eddy simulations of turbulence diffusion within the smoothed particle hydrodynamics,” *Physics of Fluids*, vol. 36, no. 4, 045105, pp. 1-21, <https://doi.org/10.1063/5.0202974>, 2024.
- [69] J.-C. Marongiu, F. Leboeuf, J. Caro and E. Parkinson, “Free surface flows simulations in Pelton turbines using an hybrid SPH-ALE method,” *J. Hydraul. Res.*, vol. 48(sup1), pp. 40–49, <https://doi.org/10.1080/00221686.2010.9641244>, 2010.
- [70] S. Lind, R. Xu, P. Stansby and B. Rogers, “Incompressible smoothed particle hydrodynamics for free-surface flows: A generalised diffusion-based algorithm for stability and validations for impulsive flows and propagating waves,” *Journal of Computational Physics*, vol. 231, no. 4, pp. 1499-1523, DOI: 10.1016/j.jcp.2011.10.027, 2012.
- [71] A. Amicarelli, B. Kocak, S. Sibilla and J. Grabe, “A 3D Smoothed Particle Hydrodynamics model for erosional dam-break floods,” *International Journal of Computational Fluid Dynamics*, vol. 31, no. 10, pp. 413-434, DOI: 10.1080/10618562.2017.1422731, 2017.
- [72] A. Khayyer, H. Gotoh, Y. Shimizu, K. Gotoh, H. Falahaty and S. Shao, “Development of a projection-based SPH method for numerical wave flume with porous media of variable porosity,” *Coastal Engineering*, vol. 140, pp. 1-22; DOI: 10.1016/j.coastaleng.2018.05.003, 2018.
- [73] G. Viccione, D. Spiniello, T. Zarra and V. Naddeo, “Fluid dynamic simulation of odour measurement chamber,” *Chemical Engineering Transactions*, vol. 40, pp. 109-114, <https://doi.org/10.3303/CET1440019>, 2014.
- [74] G. Efthimiou, F. Barmpas, G. Tsegas and N. Moussiopoulos, “Development of an Algorithm for Prediction of the Wind Speed in Renewable Energy Environments,” *Fluids*, vol. 6, no. 461, pp. 1-9, <https://doi.org/10.3390/fluids6120461>, 2021.

- [75] M. Moroni and A. Cenedese, “Penetrative convection in stratified fluids: velocity and temperature measurements,” *Nonlin. Processes Geophys.*, vol. 13, pp. 353–363, <https://doi.org/10.5194/npg-13-353-2006>, 2006.
- [76] F. Catalano, M. Moroni, A. Cenedese and V. Dore, “An alternative scaling for unsteady penetrative free convection,” *J. Geophys. Res.*, vol. 117, pp. D18102, <https://doi.org/10.1029/2012JD018229>, 2012.
- [77] B. Sawford, “Micro-Mixing modelling of scalar fluctuations for plumes in homogeneous turbulence,” *Flow, Turbulence and Combustion*, vol. 72, pp. 133-160, <https://doi.org/10.1023/B:APPL.0000044409.74300.db>, 2004.
- [78] R. Brown and R. Bilger, “The Diffusion of conserved and reactive scalars behind line sources in homogeneous turbulence,” *Journal of Fluid Mechanics*, vol. 318, pp. 339-372, 1996.
- [79] B. L. Sawford, “Lagrangian stochastic modelling of chemical reactions in a scalar mixing layer,” *Boundary-Layer Meteorology*, vol. 118, pp. 1-23, 2006.